SÃO PAULO STATE UNIVERSITY - UNESP
SCHOOL OF ENGINEERING - BAURU

ISABELA AUGUSTO SILVEIRA

NUMERICAL STUDY OF THE HYDROMECHANICAL BEHAVIOR OF ITAIPU'S LEFT BANK EARTH DAM

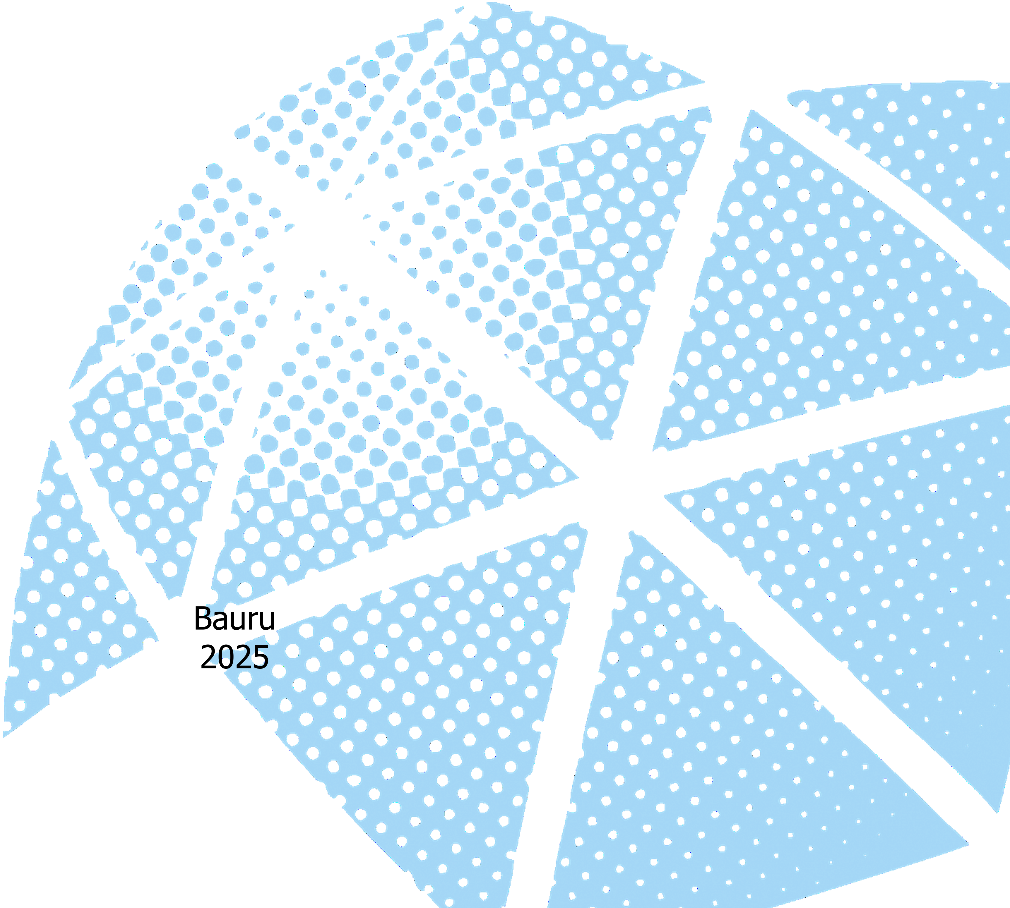

Bauru
2025

ISABELA AUGUSTO SILVEIRA

NUMERICAL STUDY OF THE HYDROMECHANICAL BEHAVIOR OF ITAIPU'S LEFT BANK EARTH DAM

Thesis presented to the São Paulo State University (UNESP), School of Engineering at Bauru, as a requirement for obtaining a PhD in Civil and Environmental Engineering.

Area of Concentration: Geotechnical Engineering

Advisor: Prof. Dr. Roger Augusto Rodrigues
Co-advisor: Prof. Dr. Heraldo Luiz Giacheti
Co-advisor: Prof. Dr. Jean Vaunat

Bauru
2025

Silveira, Isabela Augusto.
Numerical Study of the Hydromechanical Behavior of Itaipu’s Left Bank Earth Dam / Isabela Augusto Silveira. - Bauru, 2025
132 f. : il, tabs.

Tese (Doutorado) -Universidade Estadual Paulista (Unesp), Faculdade de Engenharia, Bauru
Orientador: Roger Augusto Rodrigues

1. Unsaturated soil. 2. Saturated soil. 3. Earth dam. 4. Numerical simulation. 5. SI curve. I. Universidade Estadual Paulista. Faculdade de Engenharia. II. Título.

ATA DA DEFESA PÚBLICA DA TESE DE DOUTORADO DE ISABELA AUGUSTO SILVEIRA, DISCENTE DO PROGRAMA DE PÓS-GRADUAÇÃO EM ENGENHARIA CIVIL E AMBIENTAL, DA FACULDADE DE ENGENHARIA - CÂMPUS DE BAURU.

Aos 20 de outubro de 2025, às 8h30min, por meio de Videoconferência, realizou-se a defesa de TESE DE DOUTORADO de ISABELA AUGUSTO SILVEIRA, intitulada **NUMERICAL STUDY OF THE HYDROMECHANICAL BEHAVIOR OF ITAIPU'S LEFT BANK EARTH DAM**. A Comissão Examinadora foi constituída pelos seguintes membros: Prof. Dr. ROGER AUGUSTO RODRIGUES (Orientador(a) - Participação Presencial) do(a) Departamento de Engenharia Civil e Ambiental / Universidade Estadual Paulista (UNESP) - Faculdade de Engenharia - Câmpus de Bauru , Prof. Dr. LEONARDO JOSÉ DO NASCIMENTO GUIMARÃES (Participação Virtual) do(a) Departamento de Engenharia Civil / Universidade Federal de Pernambuco, Profa. Dra. JOSIELE PATIAS (Participação Virtual) do(a) Departamento de Engenharia Civil e Arquitetura / Itaipu Binacional, Prof. Dr. MICHAEL ANDRADE MAEDO (Participação Virtual) do(a) Departamento de Engenharia Civil / Universidade Federal de Uberlândia, Prof. Dr. CAIO GORLA NOGUEIRA (Participação Presencial) do(a) Departamento de Engenharia Civil e Ambiental / Faculdade de Engenharia Câmpus Bauru, Após a exposição pela doutoranda e arguição pelos membros da Comissão Examinadora que participaram do ato, de forma presencial e/ou virtual, a discente recebeu o conceito final:___Aprovada_______. Nada mais havendo, foi lavrada a presente ata, que após lida e aprovada, foi assinada pelo(a) Presidente(a) da Comissão Examinadora.

gov.br
Documento assinado digitalmente
ROGER AUGUSTO RODRIGUES
Data: 21/10/2025 00:34:49-0300
Verifique em https://validar.iti.gov.br

Prof. Dr. ROGER AUGUSTO RODRIGUES

Acknowledgements

Aos meus pais, Rosângela e Luiz, pelo apoio incondicional e pelo incentivo constante na realização dos meus sonhos;

À minha irmã Marina, exemplo de vida e inspiração; aos meus sobrinhos, Eli e Olivia, que me ensinam diariamente o que é o amor; and to Steve, who has always been willing to help;

À minha família, em especial às minhas avós Anita e Odete, pela presença constante ao longo da minha trajetória;

Ao Prof. Dr. Roger Augusto Rodrigues pela orientação e anos de confiança;

Ao Prof. Dr. Heraldo Luiz Giacheti pela coorientação e ensinamentos;

Al Prof. Dr. Jean Vaunat, por la supervisión durante la estancia doctoral en la UPC, por la acogida, por la co-dirección de este trabajo y por sus valiosas enseñanzas;

Ao Prof. Michael Maedo, que me recebeu na UFU e sempre esteve disposto a ajudar. Agradeço especialmente pelos ensinamentos de Fortran, CODE_BRIGHT e pela contribuição na implementação da curva SI;

Aos professores do Programa de Pós-Graduação de Engenharia Civil e Ambiental;

À Josiele Patias e ao Rodrigo de Lima Rodrigues, pela disponibilidade, auxílio com as informações da barragem de Itaipu e pela confiança na elaboração desta pesquisa;

Aos técnicos do Laboratório de Mecânica dos Solos da UNESP, Gustavo e Sérgio pelas orientações, dedicação e paciência, exercendo um trabalho exemplar no laboratório;

Aos amigos da pós: Caio, Marcela, Murilo, Nayra, Mariana, Lucas, Jhaber, Johana, Luís, Higor, Thalita, Breno, Amanda, Diego e Tamara, por todos os momentos de descontração, cafés e risadas;

Aos amigos que tive a felicidade de conhecer durante minha estadia na Universitat Politècnica de Catalunya (UPC) e Universidade Federal de Uberlândia (UFU), que tornaram essa experiência ainda mais enriquecedora;

Aos amigos de longa caminhada. Vocês sempre estiveram ao meu lado e me ajudaram a tornar a vida mais leve;

Aos meus padrinhos: Fernanda e Valmir, Tatá e Guto, pelo cuidado e torcida;

À Elenice e José Roberto, minha família de coração;

À Coordenação de Aperfeiçoamento de Pessoal de Nível Superior (CAPES) pela bolsa concedida a qual tornou possível o desenvolvimento desta pesquisa;

E a todos que, de forma direta ou indireta, contribuíram para a realização deste trabalho.

Abstract

The analysis of the hydro-mechanical conditions of both saturated and unsaturated soils is essential for understanding the geotechnical behavior of earth dams. Constitutive models and numerical simulations that consider hydro-mechanical coupling provide consistent framework for understanding and predicting the behavior of these soils. This research aims to numerically analyze the geotechnical behavior of the Itaipu dam throughout its construction, reservoir filling, and years of operation, with particular emphasis on understanding the settlement case observed during operation, taking into account the saturated and unsaturated conditions of the massif. The stress–strain and flow responses of the dam were simulated using the finite element method and a coupled hydro-mechanical approach. The finite element program CODE_BRIGHT, together with the Barcelona Basic Model (BBM) as the constitutive law, was employed to reproduce the dam's construction, reservoir filling, and operational phases. Furthermore, in order to incorporate drying-induced hardening effects in the analyses, the BBM was extended within CODE_BRIGHT by implementing the suction-increase (SI) curve. The results of the numerical simulations were compared with field instrumentation data, showing good agreement during construction and reservoir filling. However, during the operational phase, simulations using the original BBM formulation failed to reproduce the observed settlements, likely due to a series of water level drawdowns that maintained the reservoir below the full operational level. The implementation of the SI curve successfully captured the volumetric shrinkage tests under drying conditions, accounting for plastic hardening caused by suction increase. Nonetheless, even with the SI curve, the numerical analyses of the dam could not reproduce the settlements, as the reservoir drawdowns during operation were insufficient to reduce suction and activate drying-induced plasticity as defined by the SI boundary introduced in this work.

Keywords: unsaturated soil; saturated soil; earth dam; numerical simulation; SI curve.

Resumo

A análise das condições hidromecânicas de solos saturados e não saturados é essencial para a compreensão do comportamento geotécnico de barragens de terra. Modelos constitutivos e simulações numéricas que consideram o acoplamento hidromecânico fornecem a base necessária para interpretar e prever a resposta desses solos. A barragem de terra da margem esquerda de Itaipu dispõe de um extenso conjunto de dados de instrumentação de campo, além de relatórios bem documentados. Assim, esta pesquisa tem como objetivo analisar numericamente o comportamento geotécnico da barragem de Itaipu ao longo da sua construção, enchimento do reservatório e anos de operação, com ênfase especial na compreensão do caso de recalque observado durante a operação da barragem, considerando tanto as condições saturadas quanto não saturadas do maciço. As respostas tensão–deformação e de fluxo da barragem foram simuladas por meio do método dos elementos finitos e de uma abordagem hidromecânica acoplada. O programa de elementos finitos CODE_BRIGHT, em conjunto com o Modelo Básico de Barcelona (BBM) como lei constitutiva, foi utilizado para reproduzir as fases de construção, enchimento e operação da barragem. Além disso, com o intuito de incorporar os efeitos de plastificação por secagem nas análises, o BBM foi estendido no CODE_BRIGHT pela implementação da curva SI (conhecida como *suction increase curve*)**.** Os resultados das simulações numéricas foram comparados com os dados de instrumentação de campo, apresentando boa concordância durante as etapas de construção e enchimento do reservatório. No entanto, durante a fase operacional, a simulação utilizando a formulação original do BBM não reproduziu os recalques observados, sendo estes devido a uma provável série de rebaixamentos do nível d'água que mantiveram o reservatório abaixo do nível operacional máximo. A implementação da curva SI permitiu reproduzir os ensaios laboratoriais de retração volumétrica por secagem, considerando as deformações plásticas decorrente do aumento de sucção. Ainda assim, mesmo com a consideração da curva SI, a análise numérica da barragem não foi capaz de representar os recalques, uma vez que os rebaixamentos do nível de água durante a operação não foram suficientes para reduzir a sucção e ativar a plastificação por secagem definida pela fronteira da curva SI implementada neste trabalho.

Palavras-Chave: solo não saturado; solo saturado; barragem de terra; simulação numérica; curva SI.

List of Figures

List of Tables

List of Symbols

s	Soil suction
u_a	Pore-air pressure
u_w	Liquid pressure
$\boldsymbol{\sigma}$	Stress tensor
$\boldsymbol{\delta}$	Kronecker delta
$\mathbf{D}$	Inverse of the fourth-order tensor expressed in terms of net stress
$d\boldsymbol{\varepsilon}$	Strain increment tensor
p	Net mean stress (excess of mean stress over air pressure)
q , J	Deviatoric stress
κ	Elastic stiffness for changes in net mean stress
κ_s	Elastic stiffness for changes in suction
$\lambda(0)$	Stiffness parameter for changes in net mean stress for virgin states of the saturated soil
β	Parameter controlling the rate of increase of soil stiffness with suction
r	Parameter defining the maximum soil stiffness
k	Parameter describing the increase in cohesion with suction
M	Slope of the projection of the critical state line
p_0^*	Preconsolidation stress for saturated conditions
p_c	Reference stress
$\mathbf{k}$	Intrinsic permeability tensor (m²)
k_{rl}, k_{rg}	Relative permeability of the liquid and gas phase (m/s)
μ_α	Dynamic viscosity of the phase liquid or gas
$\mathbf{g}$	Gravity vector
S_{rl}, S_{ls}	Residual and maximum degree of saturation
P_0	Reference pressure in certain temperature
λ	Parameter that controls the shape of the Van Genuchten curve
P_M	Air entry value of the macrostructural bimodal SWRC
M_{RC}	Shape coefficient of the macrostructural bimodal SWRC
P_m	Air entry value of the microstructural bimodal SWRC
m_{RC}	Shape coefficient of the microstructural bimodal SWRC
w	Weight of the bimodal SWRC
θ_l^w, θ_g^w	Volumetric mass of the specie water in the liquid and gas phase
S_l, S_g	Degree of saturation of the liquid and gas phase
ϕ, n	Porosity
$\mathbf{j}_l^w, \mathbf{j}_g^w$	Net flow of the specie water in the liquid and gas phase
θ_l^a, θ_g^a	Volumetric mass of the specie air in the liquid and gas phase
$\mathbf{q}_l, \mathbf{q}_g$	Darcy's flow of the liquid and gas phase
$\mathbf{i}_g^w, \mathbf{i}_l^w$	Diffusive flux of the specie water, given by Fick's Law
$\mathbf{i}_g^a, \mathbf{i}_l^a$	Diffusive flux of the specie air, given by Fick's Law

$\mathbf{j}_l^a, \mathbf{j}_g^a$	Net flow of the specie air in the liquid and gas phase
f^w, f^a	External supply of the species water and air
$\mathbf{b}$	Body forces
ρ_s	Mass of solid per unit volume of solid
$\dot{\mathbf{u}}$	Velocity
ρ_d	Dry density
e	Void ratio
E	Young Modulus
ν	Poisson's ratio
K	Bulk Modulus
$\mathbf{C}$	Fourth-order tensor expressed in terms of net stress (subscript *e* indicates elastic, and subscript *ep* indicates elastoplastic)
$\boldsymbol{\varepsilon}_{tr}$	Elastic trial strain
$\boldsymbol{\sigma}_{tr}$	Elastic trial stress
$\boldsymbol{\sigma}^{old}$	Stress from the previous step converged
s_{tr}	Elastic trial suction
α_s	Suction coupling coefficient
p_{atm}	Atmospheric pressure
θ	Lode's angle
g_y	Function of the Lode's angle
$\boldsymbol{\varepsilon}_r$	Residual strain
$\boldsymbol{\sigma}^{prev}$	Previous integration stress
$\boldsymbol{\sigma}^{pred}$	Predicted integration stress
$\boldsymbol{\sigma}_{\boldsymbol{\mu}}$	Weighted stress (second-order stress)
$\boldsymbol{\sigma}^{int}$	Integration stress
$\boldsymbol{\sigma}^{new}$	Stress converged for the next step
H, H_{cr}	Plastic parameters
$\boldsymbol{\Gamma}_s$	Plastic flow matrix associated with the soil suction variation
$\boldsymbol{\sigma}^{corr}$	Stress correction used in the Yield correction algorithm
α	Scalar to define the elastic portion of the stress increment and determines the stress state that reaches the yield surface without plastic deformation
s_0	Hardening parameter of the suction increase curve (SI curve)
λ_s	Stiffness parameter for changes in suction for virgin states of the soil
B	Non-dimensional constant that controls the smoothness of the LC-SI curve

Table of Contents

1 INTRODUCTION

Earth dams projects aim to ensure structural stability under a set of conditions expected during their service life. It is necessary to evaluate the mechanical and hydraulic conditions in a combined manner due to the development of pore pressure during construction, after impoundment, and during the lowering of the reservoir level (ALONSO; CARDOSO, 2010).

Earth dams are constructed with compacted soil. Therefore, the design construction, and performance of these geotechnical structures needs to be evaluated from the perspective of unsaturated soil mechanics (FREDLUND; MORGENSTERN, 1977; FREDLUND; RAHARDJO, 1993; LU; NIKOS, 2004). The dam operation lead to transient reservoir conditions and the estimation of distributed pore pressure requires material characterization based on concepts from unsaturated soil mechanics such as relative permeability and soil water retention curve (ALONSO; PINYOL, 2008).

Predicting the behavior of earth dams represents a major challenge, as traditional geotechnical methods may have limitations. The analyses of the hydro-mechanical conditions of the unsaturated soils can accurately estimates the earth dam properties and parameters in terms of deformations and flows.

In this context, the Barcelona Basic Model (BBM) stands out as a constitutive model for predicting the mechanical behavior of earth dams, as it is capable of reproducing the main characteristics of the behavior of compacted non-expansive soils (ALONSO; GENS; JOSA, 1990). The BBM has already been used in other dam-related studies found in the literature, revealing the potential of this mechanical model in comprehending the behavior of earth dams. The applications of the BBM include numerical simulation of historical cases covering construction, impoundment, and operation (ALONSO et al., 2011; ALONSO; OLIVELLA; HUGAS, 2005; ALONSO; OLIVELLA; PINYOL, 2005; COSTA; ALONSO, 2009; PINYOL; ALONSO, 2019) and numerical analysis of rapid drawdown (ALONSO; PINYOL, 2016; PINYOL; ALONSO; OLIVELLA, 2008; TURKSON; VANDENBERGE, 2023).

The left bank earth dam of Itaipu is an important numerical simulation case study due to its national and international relevance. Moreover, there is the availability of a set of well-documented reports, laboratory and in-situ tests, as well as a comprehensive set of field monitoring data covering the construction and impoundment, and several years of dam operation.

Since the initial filling of the Itaipu reservoir, the earth dam has operated for long periods with the reservoir water level at the normal operating level defined in the design phase. However, between 1999 and 2000, the reservoir water level reached the lowest historical operating level, remaining below the project level for four months. A series of drawdowns kept the reservoirs at low operating water levels for three years, between 2012 and 2015.

During this period of reservoir water level drawdowns, the instruments installed on the dam indicated the occurrence of small settlements, possibly related to drying events in a structure that has been in operation for over 30 years. Despite the presence of well-supported examples for the design, construction, and operation of earth dams, none of them address the case of settlement caused by the drying phenomenon, as explored in this study.

Therefore, this research studies the left bank earth dam of Itaipu through numerical simulations that consider the unsaturated soil condition. In this context, the stress–deformation and flow behavior of the dam were numerically simulated using the finite element method and coupled hydro-mechanical analyses. The analyses encompassed the entire construction and reservoir impoundment history, as well as more than thirty years of operation, in order to understand the occurrence of the settlements recorded during the periods of operation with low reservoir water levels. Furthermore, to incorporate the effects of suction-induced hardening, the Barcelona Basic Model was extended in CODE_BRIGHT through the implementation of the suction-increase (SI) curve, allowing for a more consistent evaluation of possible drying hardening on the dam's mechanical response.

2 OBJECTIVES OF THIS STUDY

The main objective is to study the geotechnical behavior of the left bank earth dam of Itaipu during construction, reservoir impoundment, and operation, from 1984 to 2017. The section under analysis is 135+50, where the survey marker installed nearby recorded an atypical settlement. The numerical simulation of the earth dam was set up in the CODE_BRIGHT program using the BBM (Barcelona Basic Model) mechanical model for partially saturated soils for both the foundation clay and compacted embankment.

The specific objectives of this study are:

- To define the mechanical and hydraulic parameters used in the constitutive models of the materials comprising the earth dam, based on laboratory results considering both the saturated and unsaturated condition of these materials and the available historical data;
- To numerically simulate the geotechnical behavior of the left bank earth dam of Itaipu during construction and impoundment using the finite element method, through coupled hydro-mechanical analyses;
- To numerically simulate the geotechnical behavior of the left bank earth dam of Itaipu during the operational period by the finite element method, through coupled hydro-mechanical analyses. The simulation of the dam operation aims to understand the settlement that occurred between 2012 and 2015, recorded by the survey marker installed near the section under analysis (station 135+50). These settlements occurred after prolonged periods of operation with reservoir water levels below normal operating levels;
- To compare the numerical simulations with field instrumentation data collected during construction and subsequent operation;

- To implement in CODE_BRIGHT the modification of the Barcelona Basic Model (BBM) proposed by Pedroso and Farias (2011), by incorporating the suction-increase (SI) yield curve into the Thermo-Elastoplastic Model for soils (TEP);
- To validate the implementation of the SI curve through a benchmark from the literature and experimental volumetric shrinkage tests due to drying, performed on both the foundation clay and the compacted embankment soils of the Itaipu earth dam;
- To apply the extended BBM with the SI curve to the numerical simulation of the Itaipu earth dam, in order to investigate whether the drying-induced hardening mechanism can contribute to explaining the settlements observed during the operational period.

3 BIBLIOGRAPHIC REVIEW

3.1 Unsaturated Soils: A briefly review

Natural occurrences of unsaturated soil include aeolian, alluvial and colluvial sedimentary soils, as well as lateritic and saprolitic residual soils. The excavation, remolding, and compaction process result in unsaturated material whose behavior is challenging to predict within traditional soil mechanics framework. Unsaturated soils are a three-phase system comprising solids, liquids and gases. Understanding the interactions between these phases is fundamental for comprehending the behavior of a partially saturated soil.

A milestone in the evolution of unsaturated soil mechanics was the recognition of soil water suction as the driving potential for flow and water content transfer. Classic studies dating back to the 1950s highlights this concept (ALONSO, 2006). Suction characterizes unsaturated soils by describing the mechanisms that retain water within the soil skeleton. Suction can be elucidated through energy concepts from thermodynamics and soil physics, as presented in classic studies by Croney (1952) and Aitchison (1965). The total water potential encompasses matric, osmotic, and pneumatic potentials, along with other minor components.

The concept of matric suction arises from the interaction between the liquid and gas phases, due to the difference in air and water pressures in the pores. Matric suction depends on surface tension and on the curvature radius of the meniscus at the interface between the liquid and gas phases. Conceptually, it is defined as the difference between air pressure and the interstitial water pressure within the soil ($s = u_a - u_w$). Osmotic suction arises from solute concentration in the soil. In the study of the mechanical and hydraulic behavior of unsaturated soils, matric suction is the primary source of suction affecting the mechanical behavior.

Understanding the mechanical behavior of unsaturated soil preceded the initial studies and advances in flow analysis. In general, the evolution of unsaturated soil mechanics can be delineated into three periods.

The first phase, spanning the 1950s and 1960s, focused on establishing the hydraulic behavior of soil while seeking a mechanical model capable of providing an effective stress to govern the stress-strain behavior of unsaturated soil. In this context, Bishop's (1959) effective stress proposal stands out. While Bishop’s equation solved flow and deformation problems in a single equation, similar to the Terzaghi’s equation for saturated soils, it failed to reproduce accurately the behavior of unsaturated soils sensitive to water content variation, such as expansive and collapsible soils.

The second phase, beginning in the mid-1960s, recognized the inadequacy of a single effective stress in fully capturing the behavior of unsaturated soils, particularly concerning volume reduction with decreasing suction or inundation. Fredlund and Morgenstern (1977) proposed to describe the stress state of unsaturated soil though two independent stress state variables: net mean stress (or excess of total stress over the air pressure) and isotropic suction. Although this combination of stress state variable is already established in unsaturated soils analysis, other combinations of two state variables to model the behavior of these soils are conceptually correct and have already been proposed by different authors (e.g. GALLIPOLI et al., 2003; ZHANG; IKARIYA, 2011). The main point lies in the necessity of at least two state variables to describe satisfactorily all the key features of the unsaturated soil behavior.

The third phase began in the late 1980s, when the development of computational tools enabled the development of consistent stress-strain laws for flow-deformation analysis in unsaturated soils. Great efforts were invested in investigating unsaturated soils behavior in terms of critical state theory and plasticity, particularly under loading and unloading cycles. Pioneering works such as the Cam Clay model (ROSCOE; SCHOFIELD, 1963) and the modified Cam Clay model (ROSCOE; BURLAND, 1968) for modeling the behavior of saturated soils remain as important references and served as the basis for the development of models for unsaturated soils.

The first constitutive model to provide a complete elasto-plastic framework for modeling the behavior of unsaturated soil was introduced by Alonso, Gens and Josa (1990), the Barcelona Basic Model (BBM). This model deals with the stress-strain relationship and uses the net mean stress and suction as stress variables. The BBM is a widely referenced mechanical model (ALONSO et al., 2024; RODRIGUES; SOARES; SANCHEZ, 2021;

SHOWKAT; BABU, 2023; SHOWKAT; MOHAMMADI; BABU, 2022). Other models have been developed subsequently.

Given the importance of numerical modeling in unsaturated soils, literature reviews have been conducted (GENS; SÁNCHEZ; SHENG, 2006; LI et al., 2011; SHENG et al., 2008), discussing crucial aspects of constitutive modeling. These include constitutive variables, wetting-induced collapse, compressibility, yielding, shear strength, failure criteria, water retention behavior and hydro-mechanical coupling.

The state and properties of unsaturated soils are susceptible to significant variations induced by external loads, weather fluctuations, and groundwater level. In essence, the primary concerns in unsaturated soil mechanics are (1) the volumetric behavior associated with changes in saturation or suction; (2) the strength behavior associated with alterations in saturation and suction, and (3) the hydraulic behavior upon changes in saturation or suction (SHENG et al., 2008).

3.2 Numerical Simulation of Unsaturated Soils: Hydro-Mechanical Analysis

The behavior of unsaturated soils depends on the interaction between the solid skeleton and pore water. For this reason, the equilibrium and conditions need to be satisfied simultaneously through hydro-mechanical coupled analysis. The basic variables of the equations are displacement and pore pressure, and the equations are formulated as a discrete system by using an approximation technique such as the principle of virtual work and/or Galerkin method (DE FARIAS; CORDÃO NETO, 2010). The formulation of the finite element method (MEF) for unsaturated soils will not be explained here but can be found elsewhere (LI; ZIENKIEWICZ, 1992; SHENG et al., 2003; SHENG; FREDLUND, 2008).

The numerical analysis of hydro-mechanical problems depends on the choice of appropriate constitutive model to represent mathematically the hydraulic and mechanical behavior of all phases of an unsaturated soil. The laws for this analysis require the relations: stress-strain-suction, storage-strain-suction, and permeability-strain-suction (DE FARIAS; CORDÃO NETO, 2010).

To address the stress-strain-suction relation, the constitutive relations for unsaturated soils are formulated in terms of two state variables: net mean stress and matric suction. The equation has the general form (DE FARIAS; CORDÃO NETO, 2010):

$$d(\boldsymbol{\sigma}_{ij} - u_a \boldsymbol{\delta}_{ij}) = \mathbf{D}_{ijkl} d\boldsymbol{\varepsilon}_{kl} - \mathbf{h}_{ij} d(u_a - u_w) \quad (1)$$

where $\boldsymbol{\sigma}_{ij}$ is the stress tensor; u_a is the pore-air pressure; $\boldsymbol{\delta}_{ij}$ is the Kronecker delta; $d(\boldsymbol{\sigma}_{ij} - u_a \boldsymbol{\delta}_{ij})$ is the increment in the tensor of net stresses; $\mathbf{D}_{ijkl}$ is a fourth-order tensor representing stiffness moduli in terms of net stresses; $d\boldsymbol{\varepsilon}_{kl}$ is the incremental in strain tensor; $\mathbf{h}_{ij}$ is a nondimentional second-order tensor of coefficients that represents the interaction between the solid skeleton and contractile skin; and, $d(u_a - u_w)$ is the increment in matric suction.

Equation (1) expresses the increase in net mean stress due to strain or arrangement of the soil particles (the first term on the right side) and changes in the matric suction (the second term of the right side). The tensors $\mathbf{D}_{ijkl}$ and $\mathbf{h}_{ij}$ are calculated based on the concepts of elasto-plasticity, requiring definitions of a yield function, a plastic potential function, and a hardening law. These functions are dependent on material parameters, stress state, stress history, and variables specific for each constitutive model. The BBM is the mechanical constitutive model employed in this research and will be further detailed in subtopic (3.2.1).

The storage-strain-suction relation elucidates how the volumetric water content varies with changes in the representative elementary volume of the unsaturated soil and with changes in matric suction. This relation reflects the coupling between the continuity and equilibrium conditions. The hydraulic constitutive equations and the equilibrium restriction used in this research and will be further detailed in subtopic (3.2.2).

*3.2.1 **Mechanical Constitutive Model: Barcelona Basic Model (BBM)***

Barcelona Basic Model (BBM) is an elastoplastic constitutive model introduced by Alonso, Gens and Josa (1990). The model incorporates the suction ($s = u_a - u_w$, where u_a is the air pressure and u_w is the liquid pressure) and the net mean stress, p ($\frac{1}{3}\mathrm{tr}(\boldsymbol{\sigma}) - u_a$, defined as the excess of mean stress over air pressure) as state variables. Additionally, it incorporates the specific volume, υ, to reproduce volumetric behavior.

The BBM defines two yield surfaces in the (*p,s*) space to delimit the region where the soil behaves elastically: the Loading-Collapse (LC) curve and the Suction Increase (SI) curve. The limits defined by the SI and LC curves are coupled; in other words, if the soil suction induces the shift of SI limit curve, the LC curve will also be shifted. Once the elastic limit is surpassed, the soil undergoes plastic deformation and the SI and LC limit curves are translated to a new position in the (*p, s*) space (Figure 1).

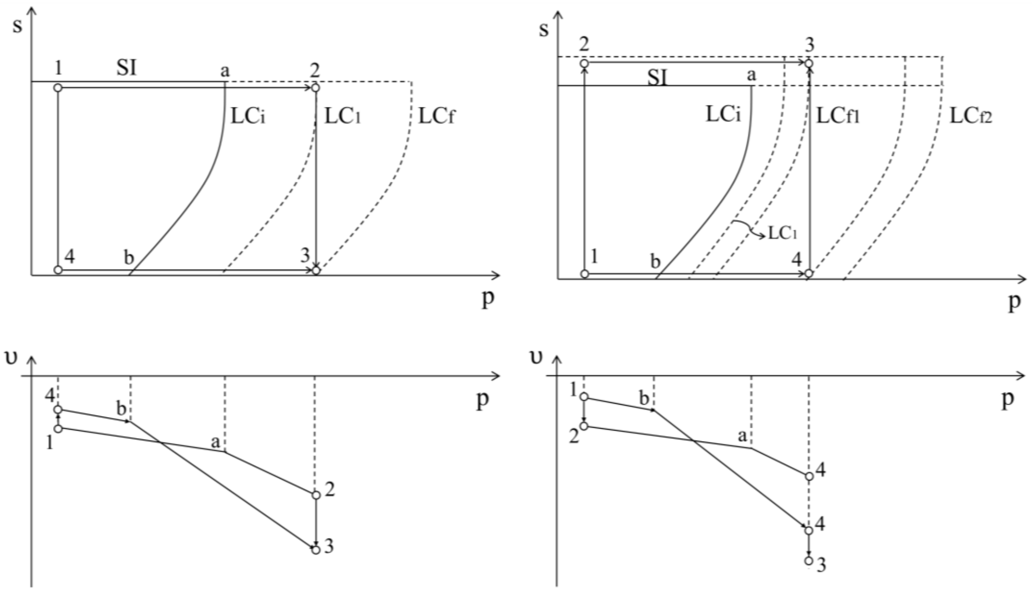

(a) (b)

Figure 1. Volumetric deformations paths to increments of (a) net mean stress and wetting, and (b) net mean stress and drying (ALONSO; GENS; HIGHT, 1987)

Figure 2 illustrates the three-dimensional yield surface in (p, q, s) space, where p is the net mean stress and q is deviatoric stress $(\sigma_1 - \sigma_3)$. The yield surface corresponds to the Modified Cam Clay (MCC) when saturated conditions are attained. The size of the elastic domain expands with an increase in suction, and the rate of this expansion is given by the LC curve, which is one of the fundamental characteristics of the model.

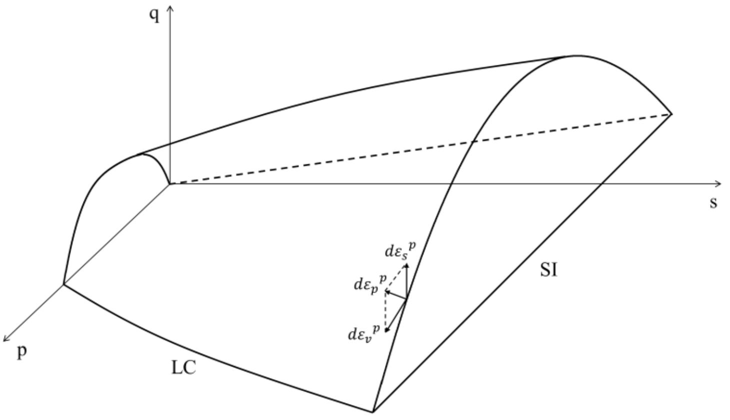

Figure 2. Three-dimensional view of the yield surfaces in (*p*,*q*,*s*) stress space (ALONSO; GENS; JOSA, 1990)

The model requires a set of material parameters that encompass elastic behavior (isotropic), including κ and κ_s; volumetric behavior (plastic states), represented by λ(0); parameters β (MPa^{-1}) and *r* defining the LC yield curve; parameters k, *G* (MPa), and *M* defining shear behavior and strength; and a reference stress parameter, p_c (MPa). The parameter p_c serves as a reference pressure in the definition of the LC yield curve.

Specifically, κ represents the elastic stiffness for changes in net mean stress, while κ_s is the elastic stiffness parameter for changes in suction. λ(0) serves as the stiffness parameter for changes in net mean stress for virgin states of the saturated soil. Parameters β and r control the stiffness on the LC curve. k describes the increase in cohesion with suction, and M represents the slope of the projection of the critical state line.

The hardening law establishes a connection between the rates of pre-consolidation pressure under saturated condition $(p_0{}^*)$ to the volumetric plastic strain rate. In essence, the BBM has four key characteristics: a single yield surface; a single plastic potential only depending on the first and the second invariant of the net stress (I1 e J2); a hardening parameter $(p_0{}^*)$; and a relationship for the deviatoric stress rate based on the deviatoric elastic strain rate through the shear modulus, *G* (PERTL; HOFMANN; HOFSTETTER, 2011).

BBM facilitates qualitative prediction similar to the way often used by the conceptual critical state framework. This implies the use of net stress as the basic stress variable, due to the simplicity to replicate effectively conventional laboratory stress paths (GENS; SÁNCHEZ; SHENG, 2006).

The BBM has provided a comprehensive understanding of essential aspects related to unsaturated soils and has widespread acceptance within the scientific community. Detailed information about its formulation can be readily located in the literature, particularly in the pioneer paper by Alonso, Gens, Josa (1990), and will not be reiterated here. For a condensed overview of the BBM formulation, refer to Table 1.

Moreover, there exist extensive reviews of constitutive models for unsaturated soil (GENS; SÁNCHEZ; SHENG, 2006; LI et al., 2011; PHOON; KULHAWY, 1999; SHENG et al., 2008), practical recommendations for selecting parameter values (GALLIPOLI; D'ONZA; WHEELER, 2010; WHEELER; GALLIPOLI; KARSTUNEN, 2002), and methodologies for parameter selection, such as the use of modified state surface approach (ZHANG; XIAO, 2013). In addition, enhanced models have been proposed to capture specific behaviors of interest, such as the Barcelona Expansive Model (BExM) for the simulation of expansive clay behavior (ALONSO; VAUNAT; GENS, 1999) and the double-structure plasticity model for expansive materials (SÁNCHEZ et al., 2005).

Table 1. Summary of the BBM equations (ALONSO; GENS; JOSA, 1990; ALONSO; OLIVELLA; PINYOL, 2005)

Isotropic Elastoplastic Volumetric Deformation	$d\varepsilon_v = \frac{\lambda(s)}{1+e}\frac{dp}{p}$
Volumetric Compressibility Index	$\lambda(s) = \lambda(0)[(1-r)\exp(-\beta s) + r]$
Hardening Law	$dp_0^* = \frac{(1+e)p_0^*}{\lambda(0)-\kappa} d\varepsilon_v^p$
Loading-Collapse Curve (LC)	$p_0(s) = p_c \left(\frac{p_0^*}{p_c}\right)^{\frac{\lambda(0)-\kappa}{\lambda(s)-\kappa}}$
Shear Strength Critical-State Parameter	$M(s) = M$
Tensile Strength Parameter	$p_s(s) = ks$
Yield Surface (Triaxial)	$F(p,q,s) = q^2 - M^2[p + p_s(s)][p_0(s) - p] = 0$
Plastic Potential (Triaxial)	$G(p,q,s) = q^2 - \alpha M^2[p + p_s(s)][p_0(s) - p] = 0$

3.2.2 *Hydraulic Constitutive Equations (Two phase flow)*

Constitutive equations and equilibrium restriction links dependent and state variables of the mass balance equation. The hydraulic constitutive equations used in this research are presented here.

Darcy's law, generalized for unsaturated soil, relates the advective flux of the phase liquid or gas due to gradient of fluid pressure (liquid or gas, respectively) (Equation 2)

.

$$\mathbf{q}_\alpha = -\frac{\mathbf{k}k_{r\alpha}}{\mu_\alpha}(\nabla P_\alpha - \rho_\alpha \mathbf{g}) \tag{2}$$

where α is the phase liquid or gas; $\mathbf{k}$ is the intrinsic permeability (m²); $k_{r\alpha}$ is the relative permeability (m/s); μ_α is the dynamic viscosity; P_α is the pressure (MPa); **g** is the acceleration due to gravity vector.

The soil water retention curve (SWRC) relates suction and degree of saturation. Many models has been proposed to the SWRC (BROOKS; COREY, 1964; GALLIPOLI; WHEELER; KARSTUNEN, 2003; MAŠÍN, 2010) but the one commonly used is the van Genuchten Model (VAN GENUCHTEN, 1980), as follow:

$$S_e = \frac{S_l - S_{rl}}{S_{ls} - S_{rl}} = \left(1 + \left(\frac{u_a - u_w}{P_0}\right)^{1/(1-\lambda)}\right)^{-\lambda} \tag{3}$$

where S_{rl} and S_{ls} are the residual and maximum degree of saturation ($m^3.m^{-3}$); P_0 is the reference pressure in certain temperature (MPa); λ is the parameter that controls the shape of the curve.

Equation 3 is used to soils that exhibit a monomodal pore size distribution, *i.e*, it has a single air entry value associated with the macropores. As the amount of fine increases, the particles tend to group into larger aggregates, whose size depends on the amount of water added. Soils with a substantial clay content typically display a fabric made up of aggregates of varying sizes and tend to have a bimodal pore size distribution. This implies the presence of two air entry values corresponding to the macropores and micropores, respectively. Macropores predominantly consist of inter-aggregate pores between aggregations, while micropores constitute intra-aggregate pores within these elementary units.

Casini, Vaunat and Romero (2012) presented a multimodal retention curve model to characterize the behavior of soil with a bimodal pore size distribution. This model incorporates a linear superposition of two subcurves of the Van Genuchten (1980) model (Equation 4). The multimodal retention curve model was employed in this research, since the studied soil exhibits a bimodal SWRC.

$$S_e = \frac{S_l - S_{rl}}{S_{ls} - S_{rl}} = (1 - w)\left[\frac{1}{1 + \left(\frac{s}{P_M}\right)^{\frac{1}{1-M_{RC}}}}\right]^{M_{RC}} + w\left[\frac{1}{1 + \left(\frac{s}{P_m}\right)^{\frac{1}{1-m_{RC}}}}\right]^{m_{RC}} \tag{4}$$

where s is the suction; P_M is the air entry value of the macrostructural SWRC; M_{RC} is the shape coefficient of the macrostructural SWRC; P_m is the air entry value of the microstructural SWRC; m_{RC} is the shape coefficient of the microstructural SWRC; w is the weight.

Generalized Darcy's law to multiphase flow requires defining the relative permeability of each phase, representing the dimensionless measure of the effective permeability of that particular phase (liquid or gas). Relative permeability expresses the ratio of the effective permeability (for a specific saturation) of that phase to the absolute permeability (i.e., when the porous medium is fully saturated with that phase).

Different models can be employed to establish the relationship between permeability and suction in unsaturated soil (*e.g.* Richards Model and Power Law). The Van Genuchten (1980) model for the relative permeability for the liquid phase (Equation 5) was used. A function relating the relative permeability with the amount of pore water in the soil is essential because water only flows through spaces filled with water (FREDLUND; RAHARDJO, 1993).

For the air phase, it is common to represent the gas relative permeability as one minus the liquid relative permeability (Equation 6). Alternatively, an independent model can be adopted if necessary.

$$k_{rl} = \sqrt{S_e}\left(1 - \left(1 - {S_l}^{1/\lambda}\right)^{\lambda}\right)^2 \tag{5}$$

$$k_{rg} = 1 - K_{rl} \tag{6}$$

Other constitutive equations (for phase density in the liquid and gas phases) and equilibrium restrictions (psychrometric law and Henry's law) are necessary to determine the unknowns: pressure in the liquid and pressure in the gas, in the mass balance equations. Table 2 lists all the equations (constitutive equations, equilibrium restrictions, and constraints) for two-phase flow in a porous medium, along with the number of unknowns for each equation used.

Equilibrium restrictions establish the relationship between state variables and the quantity of species in the phase. In this type of relationship, it is generally assumed that the phase changes occur rapidly. Therefore, the porous medium needs to be in a local equilibrium, leading to a set of equilibrium restrictions that must be satisfied at all times.

Table 2. Summary of the two phase flow equations: Mass Balance, Constitutive Equations, Equilibrium Restrictions and Constraints (SANCHEZ, 2018)

Equation Name	**Mathematical Form**	**Num. Equations**	**Num. Unknowns**
Water Mass Balance	$\frac{\partial}{\partial t}\left(\theta_l^w S_l \phi + \theta_g^w S_g \phi\right) + \nabla \cdot \left(\mathbf{j}_l^w + \mathbf{j}_g^w\right) = f^w$	1	1 (P_l)
Air Mass Balance	$\frac{\partial}{\partial t}\left(\theta_l^a S_l \phi + \theta_g^a S_g \phi\right) + \nabla \cdot \left(\mathbf{j}_l^a + \mathbf{j}_g^a\right) = f^a$	1	1 (P_g)
Darcy Law (Liquid)	$\mathbf{q}_l = -\frac{\mathbf{k}k_{rl}}{\mu_l}(\nabla P_l - \rho_l \mathbf{g})$	3	3 $(\mathbf{q}_l)$
Darcy Law (Gas)	$\mathbf{q}_g = -\frac{\mathbf{k}k_{rg}}{\mu_g}(\nabla P_g - \rho_g \mathbf{g})$	3	3 $(\mathbf{q}_g)$
Fick's Law (Vapor in gas)	$\mathbf{i}_g^w = -\mathbf{D}_g^w \nabla \omega_g^w$	3	3 $(\mathbf{i}_g^w)$
Fick's Law (Air in liquid)	$\mathbf{i}_l^a = -\mathbf{D}_l^a \nabla \omega_l^a$	3	3 $(\mathbf{i}_l^a)$
Gas/Liquid Density	$\rho_l = \rho_{l0} \exp[\beta(P_l - P_{l0}) + \alpha_T T + \gamma C]$ $\rho_g = \rho_v + \rho_a$	2	2 $(\rho_l,\ \rho_g)$
Gas/Liquid Viscosity	$\mu_l = A\exp\left(\frac{B}{273.15 + T}\right)$ $\mu_g = A\sqrt{273 + T}\left(1 + \frac{B}{273 + T}\right)^{-1}$	2	2 $(\mu_l,\ \mu_g)$
Retention Curve	$S_e = (1 - w)\left[\frac{1}{1 + \left(\frac{S}{P_M}\right)^{\frac{1}{1 - M_{RC}}}}\right]^{M_{RC}} + w\left[\frac{1}{1 + \left(\frac{S}{P_m}\right)^{\frac{1}{1 - m_{RC}}}}\right]^{m_{RC}}$	1	1 (S_l)
Henry's Law	$\theta_l^a = \omega_l^a \rho_l = \frac{P_a}{H}\frac{M_a}{M_w}\rho_l$	1	1 (ω_l^a)
Psychometric Law	$\theta_g^w = \left(\theta_g^w\right)^0 \exp\left(\frac{\psi M_w}{R(273.15 + T)\rho_l}\right)$	1	1 (ω_g^w)
Constrains	$\omega_l^a + \omega_l^w = 1$ $\omega_g^a + \omega_g^w = 1$ $S_l + S_g = 1$	3	3 $(S_g, \omega_g^a, \omega_l^w)$
Constrains	$\mathbf{i}_g^a + \mathbf{i}_g^w = 1$ $\mathbf{i}_l^a + \mathbf{i}_l^w = 1$	6	6 $(\mathbf{i}_g^a, \mathbf{i}_l^w)$
Total		30	30

3.2.3 ***CODE_BRIGHT: A Finite Element Program***

The finite element program CODE_BRIGHT is an important reference for addressing geotechnical-coupling problems. The formulation of CODE_BRIGHT is presented in Olivella et al (1996), including the weak form of the governing equations along with explicit definitions of the resulting matrices and vectors. The authors also provide insights into how variables are treated at nodes and elements.

CODE_BRIGHT adopts a compositional approach to tackle problems, focusing on a porous medium comprising solid grains, water, and gas. The interactions among these components are considered simultaneously and in a coupled manner. The program addresses three phases: solid (mineral), liquid (water and dissolved air), and gas (mixture of dry air and water vapor), with three species: water, air, and solid. To numerically solve the problem, each species is associated with a differential equation known as the balance equations. These equations are derived from the principles of mass conservation and tension equilibrium, formulated within representative elementary volumes. The solution to these equations involves determining the state variables or unknowns for numerical computation.

The specie water is present in all three phases, and the total mass balance of water is expressed as:

$$\frac{\partial}{\partial t}\left(\theta_l^w S_l \phi + \theta_g^w S_g \phi\right) + \nabla \cdot \left(\mathbf{j}_l^w + \mathbf{j}_g^w\right) = f^w \tag{7}$$

where θ_{phase}^{specie} is the volumetric mass (mass of the specie divided by the volume of the phase); S_{phase} is the degree of saturation of the phase; ϕ is the porosity; $\mathbf{j}_{phase}^{specie}$ is the net flow of the specie in the phase; f^{specie} is an external supply of the species.

Equation 8 gives the net flow of the water species in the gas phase. The first term $\left(\mathbf{j'}_g^w\right)$ corresponds to the flux of water in the gas phase relative to the solid skeleton, while the second term represents the flux of water in the gas phase associated with the movement, or velocity, of the solid respect to a fixed reference system. Similarly, Equation 9 presents the net flow of the water species in the liquid phase.

$$\mathbf{j}_g^w = \theta_g^w \mathbf{q}_g + \mathbf{i}_g^w + \theta_g^w S_g \phi \dot{\mathbf{u}} = \mathbf{j'}_g^w + \theta_g^w S_g \phi \dot{\mathbf{u}} \tag{8}$$

$$\mathbf{j}_l^w = \theta_l^w \mathbf{q}_l + \mathbf{i}_l^w + \theta_l^w S_l \phi \dot{\mathbf{u}} = \mathbf{j'}_l^w + \theta_l^w S_l \phi \dot{\mathbf{u}} \tag{9}$$

where $\mathbf{q}_{phase}$ is the Darcy's flux of the phase and $\mathbf{i}_{phase}^{specie}$ is the diffusive flux of the species, given by Fick's law.

The mass balance equation for the specie air, i.e. the main component of the gas phase and potentially found as dissolved air in the liquid phase, is similar to that of the water and it is expressed as follows:

$$\frac{\partial}{\partial t}\left(\theta_l^a S_l \phi + \theta_g^a S_g \phi\right) + \nabla \cdot \left(\mathbf{j}_l^a + \mathbf{j}_g^a\right) = f^a \tag{10}$$

Following the same approach as for the total mass balance of water, the net flows of the air species in the gas and liquid phases are given by:

$$\mathbf{j}_g^a = \theta_g^a \mathbf{q}_g + \mathbf{i}_g^a + \theta_g^a S_g \phi \dot{\mathbf{u}} = \mathbf{j}'^a_g + \theta_g^a S_g \phi \dot{\mathbf{u}} \tag{11}$$

$$\mathbf{j}_l^w = \theta_l^w \mathbf{q}_l + \mathbf{i}_l^w + \theta_l^w S_l \phi \dot{\mathbf{u}} = \mathbf{j}'^w_l + \theta_l^w S_l \phi \dot{\mathbf{u}} \tag{12}$$

In both equations 7 and 10, the first left-hand term represent the mass per unit volume of the porous media (mass of water or air in liquid and gas phases); the second left-hand term represents the fluxes of mass (total flow of water or air); and the right-hand term denotes the external supply of water or air.

The momentum balance reduces to the equilibrium of total stress within the volume of a porous media when inertial terms are neglected, assuming a quasi-static problem with small deformations (Equation 13).

$$\nabla \cdot \boldsymbol{\sigma} + \mathbf{b} = \mathbf{0} \tag{13}$$

where $\boldsymbol{\sigma}$ is the stress tensor; $\mathbf{b}$ is the body force per unit volume of the medium.

The mass balance of solid, tracking the evolution of the porosity, is written as:

$$\frac{\partial}{\partial t}\left(\rho_s(1-\phi)\right) + \nabla \cdot \left(\rho_s(1-\phi)\dot{\mathbf{u}}\right) = 0 \tag{14}$$

where $\dot{\mathbf{u}} = {}^{d\mathbf{u}}/_{dt}$ is the velocity; ρ_s is the mass of solid per unit volume of solid.

Equations 7 to 14 are written in Eulerian/local coordinates, i.e., the description of the motion is in terms of spatial coordinates, with the current configuration as the reference configuration. A more convenient form is to write the balance equations with respect to the solid velocity in the Lagrangian (or material) description, where the position and physical properties are described in terms of material coordinates. The material derivative $(D(\circ)/Dt)$ links Eulerian and Lagrangian description of motion, which is expressed generically as:

$$\frac{D(\circ)}{Dt} = \frac{\partial(\circ)}{\partial t} + \dot{\mathbf{u}} \cdot \nabla(\circ) \tag{15}$$

The term in the left part is the material derivative, which corresponds to the variation of a property in time following a specific material point. The first term in the right part is the local derivative, corresponding to the variation of a property in time of a fix point in the space. Lastly, the second term in the right part is the convective derivative.

The mass balance of water, the mass balance of air, and the mass balance of solid in Lagrangian/Material coordinates is given in equations 16 to 18, respectively.

$$\phi \frac{D\left(\theta_l^w S_l + \theta_g^w S_g\right)}{Dt} + \frac{\left(\theta_l^w S_l + \theta_g^w S_g\right)}{\rho_s}\left[(1-\phi)\frac{D\rho_s}{Dt} + \rho_s \nabla \cdot \dot{\mathbf{u}}\right] + \nabla\left(\mathbf{j}'^w_l + \mathbf{j}'^w_g\right) = f^w \tag{16}$$

$$\phi \frac{D\left(\theta_l^a S_l + \theta_g^a S_g\right)}{Dt} + \frac{\left(\theta_l^a S_l + \theta_g^a S_g\right)}{\rho_s}\left[(1-\phi)\frac{D\rho_s}{Dt} + \rho_s \nabla \cdot \dot{\mathbf{u}}\right] + \nabla\left(\mathbf{j}'^a_l + \mathbf{j}'^a_g\right) = f^a \tag{17}$$

$$\frac{D\phi}{Dt} = \frac{(1-\phi)}{\rho_s}\frac{D\rho_s}{Dt} + (1-\phi)\nabla \cdot \dot{\mathbf{u}} \tag{18}$$

In the mass balance of water (Equation 16), the first term represents the variation in water storage due to variation in partial saturation $(S_l;\ S_g)$ and/or variation in water concentration in the two phases $(\theta_l^w;\ \theta_g^w)$. The second term refers to the variation in water storage due to the solid compressibility $(D\rho_s/Dt)$ and change in volume of the skeleton of the porous medium. The third term represents the flux of water (in relation to the solid particles) in the liquid and gas phase entering/leaving the volume. The mass balance of air (Equation 17) is similar.

Solving these equations requires a set of constitutive and equilibrium restrictions. The mechanical constitutive model and the hydraulic constitutive equations were described in the previous subtopics (3.2.1 and 3.2.2, respectively).

3.3 Earth Dams analysis and unsaturated soil

Earth dams and the core zones of rockfill dams are typically constructed with compacted soil and, therefore, can be considered as unsaturated materials. However, other types of rockfill dams may include different impervious elements, such as upstream concrete faces or asphaltic cores. In the case of compacted earth structures, understanding the hydro-mechanical behavior of partially saturated soils becomes essential**,** since their response differs significantly from that of saturated soils. Both volumetric deformation and stiffness variations are strongly influenced by changes in water content, or suction.

The generation and dissipation of pore water pressure in the core of the dam is an issue in the design and construction of the earth dams. Both the safety condition and the deformations are depending on the pore pressure, being this dictated by the total stress accumulated during the construction, the as-compacted conditions and the ability of the soil to dissipate excess of pore pressure (ALONSO; BATLLE, 1995).

The stability of earth dams must be ensured under a set of conditions that occurs during the project life, which include the stability of the upstream and downstream slope during the end of construction, during reservoir impoundment and during operation. The deformations along the construction and operation phase is also a concern (ALONSO; PINYOL, 2008)

Costa and Alonso (2009) and Alonso, Olivella and Pinyol (2005) present a review of the evolution of dam behavior prediction, as outlined here. The initial attempts to model dams occurred in the late 1960s, using finite difference technique and considered solely on fluid flow. During these early studies, saturated flow was applied in analyzing pore pressure distribution for the steady condition. This analysis required explicit determination of the free surface position, followed by solving the steady state flow equation for saturated media (Laplace equation) together with Darcy Law in the saturated domain. This methodology assumed no flow through the unsaturated zone. However, during the dam operation, steady state conditions may not be reached in several years or during the lifetime of the dam, making it a conservative assumption (ALONSO; PINYOL, 2008).

The first finite element consolidation analysis of dams, reported in the 1970s, considered only saturated conditions or uncoupled analysis. The introduction of interstitial fluid compressibility, valid for unsaturated domain, and maintaining Terzaghi's effective stress principle marked a significant improvement in the analysis (e.g. GHABOUSSI; KIM, 1982 apud COSTA; ALONSO, 2009). Developing a method to describe and analyze the consolidation of unsaturated soils was crucial, as dams typically consist of these materials.

Chang and Duncan (1977) developed a practical procedure for performing finite element analyses of dam behavior during construction, impoundment and operation. This procedure accounts for the coupled effects of stress and flow in the unsaturated soil by using a modified Cam Clay Model. The model considers varying permeability and compressibility of the pore fluid, as well as the nonlinear stress-strain behavior of the soil. Alonso and Batlle (1995) developed a coupled flow-deformations theory for unsaturated soils applied in a dam case, with net stress and suction as independent variables. The volumetric behavior was defined using the concept of state surfaces and encompassed swelling and collapse phenomena.

One of the earliest applications of unsaturated soil models to dams considering three-phase soil was reported by Alonso et al. (1988 apud COSTA; ALONSO, 2009). Currently, the BBM is widely employed in the analysis of earth dam cases (discussed in subtopic 3.4).

Beliche Dam is a real-life case illustrating the evolution of dam analysis. Naylor et al. (1986) predicted the dam's behavior before construction and before field data was available, using two nonlinear elastic models: K-G model (NAYLOR et al., 1981) and Hyperbolic Model. They predicted a maximum settlement of 40 cm in the center of the dam at the end of construction; while the actual end-of-construction settlement was over 1 m. The underestimation of actual values was later attributed to the collapse effects associated with unexpected partial impoundment during construction.

Naylor, das Neves and Pinto (1997) conducted a finite element back analysis of the Beliche Dam due to the substantial underestimation of settlement. The authors used a critical state elasto-plastic model instead of the nonlinear elastic models used in the earlier work. Collapse settlement was modeled through a numerical algorithm reproducing a change in material properties from a dry state to a saturated state. The results successfully fit the measured settlements in the center of the dam, although underpredicting the settlement on the crest and downstream. The analysis did not attempt to model the effects of partial saturation.

Finally, Alonso, Olivella and Pinyol (2005) simulated the complete history of Beliche dam construction, impoundment, and rainfall using a coupled flow–deformation model considering the partial saturation. The BBM was adopted for the clay core, and the Rockfill Model was used for the shoulder. The results found by Alonso, Olivella and Pinyol (2005) are further detailed in subtopic 3.4.

In summary, the Beliche dam underwent an initial analysis employing nonlinear elastic models and a critical state elasto-plastic model developed within the framework of effective stress analysis, both uncoupled from water flow. The first prediction, utilizing the nonlinear elastic model, yielded a settlement significantly lower than the actual field measurements. Meanwhile, the analysis employing the critical state elasto-plastic model, while approaching more accurate settlements, failed to anticipate the rockfill collapse induced by partial, as well as, full wetting. The coupled hydro-mechanical model, featuring the BBM and the Rockfill as the mechanical models, proved effective in addressing the environmental factor. Climatic effects influence the dam deformation and the coupled model successfully considered the interplay between mechanical and hydrological aspects, providing a more comprehensive understanding of the dam's behavior.

Understanding the behavior of compacted soil is essential to understand the behavior of earth dams. Compaction control relies on two fundamental parameters: dry density and water content. These parameters are not explicitly incorporated into constitutive models such as BBM, which handles stress-strain relationships. However, the dry density can be linked indirectly to pre-consolidation stress, as an increase in yielding stress implies an increase in density. Conversely, water content and dry density (or void ratio) determine soil suction. The stress pair (${p_0}^*$: isotropic yield stress for saturated conditions; s: suction) describes the compaction state (ρ_d, w).

When the initial compaction state significantly influences the mechanical behavior, models such as the BBM offer a straightforward and robust means of representing compacted soil behavior. A unique set of material parameters characterizes soil mineralogy and grain size distribution, and initial compaction states is described by the pair (${p_0}^*$; s) (PINYOL; ALONSO, 2019).

The compacted conditions will determine the initial conditions; that is, the initial stress state, which is a state of negligible stress immediately after compaction, before any subsequent loading due to construction. The other effects of the compaction procedure on the mechanical response of the soil that cannot be explained by the initial conditions must be attributed to the constitutive parameters (ALONSO; PINYOL, 2008).

3.4 Numerical Simulation of Earth Dams

Earth and rockfill dams have been designed and built worldwide predating the development of unsaturated soil theory, and even saturated soils theory. This indicates that accumulated experience and traditional design principles have resulted in safety designs. However, contemporary unsaturated soil mechanics provides theories, experimental procedures and computational tools that has the potential to enhance the state of art in the design and operation of dams (ALONSO; PINYOL, 2008).

The BBM is one of the elastoplastic constitutive models for unsaturated soils that has been implemented relatively widely within finite element codes. In this context, an overview of numerical simulations in dam engineering, with a specific focus on employing the BBM as a mechanical model, will be presented here. A review of the literature reveals three primary categories within this domain: i) numerical simulation and analysis of historical cases involving earth and rockfill dams; ii) numerical simulation of scenarios involving rapid drawdown; and iii) enhancements in the analysis using numerical simulation, for example, applying reliability theory.

The Beliche dam, included among the historical case simulations, had been previously studied; however, its first numerical simulation with an elastoplastic model (using the BBM for the core) and incorporating hydro-mechanical coupling was carried out by Alonso, Olivella, and Pinyol (2005). Beliche Dam is a 54 m high located in Algarve, Portugal. The dam has a large set of laboratory tests (oedometer and triaxial tests), as well as extensive field monitoring data, covering both the construction and impoundment, along with several years of operation data.

The historical significance of the case lies in a notable collapse of the upstream shell (rockfill) during construction, caused by an unexpected temporary rise in the reservoir level due to heavy rainfall. This collapse occurred within the lightly compacted inner zone of the rockfill. The numerical simulation of the dam successfully captures the plastic deformations resulting from the rockfill collapse, encompassing the entire construction process, the variation of water level in the reservoir, and the rainfall patterns. The analysis revealed that the downstream shell and core experienced wetting and drying cycles, mostly remaining within the elastic zone. However, extreme rainfall events have the potential to displace the current yield locus, leading to irreversible plastic volumetric deformations (Figure 3).

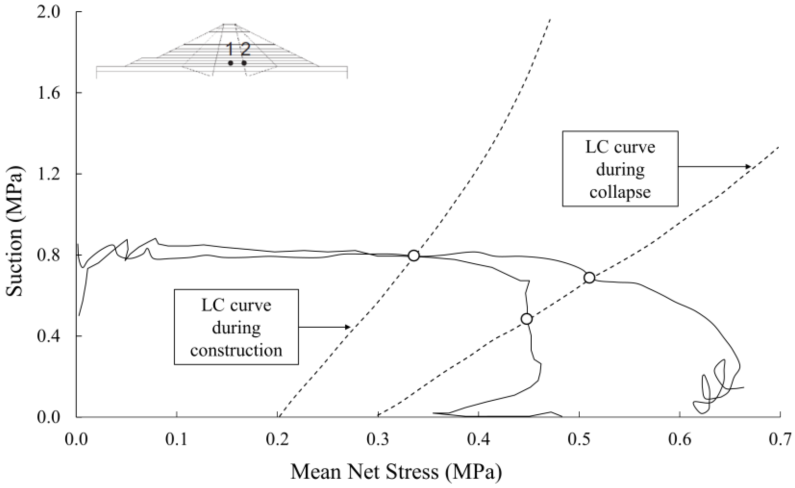

Figure 3. Loading collapse curve during construction and during collapse for the clay core (ALONSO; OLIVELLA; PINYOL, 2005)

Alonso and Olivella (2006) state that the deformation of dams is influenced by climatic effects, requiring an elasto-plastic formulation of the stress-strain behavior to accurately capture this response. According to the authors, the case of Beliche Dam is an important insight into the potential of coupled flow-deformation analysis in understanding dam behavior. Traditionally, dams have been analyzed using finite element techniques within the framework of Terzaghi's effective stress. However, this method is insufficient in addressing environmental factors. Analysis within the context of unsaturated soil mechanics not only aids in discerning deformations associated with suction changes but also separates them from pure creep effects. The former may remain significant for several years of dam operation, in which the effects of the water level are dominant.

The construction and impoundment of El Infernillo Dam were also subjected to numerical simulation using the BBM as a mechanical model (ALONSO; OLIVELLA; HUGAS, 2005). This 150-meter high dam, constructed in Mexico in the 1960s, has been revisited as a historical case from the perspective of modeling unsaturated soils. The availability of laboratory information, coupled with well-documented field behavior, allowed the opportunity to check the performance and capabilities of both theoretical and numerical models.

Costa and Alonso (2009) predicted the behavior of Lechago's Dam during its construction phase. The BBM model was applied to the dam's shoulders, filter, and core. The uniqueness of Lechago's Dam lies in specific construction aspects, including a preloading stage to enhance the strength of the soft foundation soils and use of treated soil columns to increase foundation stiffness. However, a direct comparison with field measurements was not possible as the dam was still under construction at the time. Some years later, Alonso et al. (2011) conducted a comparative analysis of the model's performance for Lechago's dam using the now available field data obtained from total stress cells, hydraulic gauges, and piezometers. The results demonstrated consistency when comparing real data with modeled data. Additionally, the authors simulated the dam filling process, which had not yet occurred at the time of the predictions.

Kolev (2017) conducted a case study on the Denis Perron Dam. The 171-meter high dam, situated in Canada, was constructed as a rockfill with a central till core. The numerical simulation, employing both the BBM and the CODE_BRIGHT, effectively captured the staged construction, reservoir impoundment and rainfall history recorded. The simulations successfully replicated deformations measured by the inclinometers during construction and impoundment phases, both upstream and downstream. Additionally, the model accurately reproduced measurements from piezometer and pressure cell measurements.

Pinyol and Alonso (2019) discussed the challenges associated with characterizing the behavior of compacted materials used in the construction of earth dams and assessing the calculated response against field monitoring data, even when data on geotechnical properties is available. The authors employed the CODE_BRIGHT to model the behavior of the Albagés Earth Dam (Spain). Initially, they calibrated the dam model, which has a height of 40 meters. Subsequently, with field compaction data and additional in situ tests, they updated the model prediction once the dam reached a reasonable height during the construction (specifically when the dam reached two-thirds of the total final height). The model prediction was then compared with monitoring data, focusing on stress, pore pressure, and settlements. The results demonstrated the model's ability to reproduce the key aspects of the dam's performance.

Table 3 summarizes the main characteristics of the described historical cases involving Earth and Rockfill dams. As previously mentioned, these cases correspond to numerical analyses of dam behavior reported in the literature, in which the Barcelona Basic Model (BBM) was adopted as the constitutive framework. The information regarding instrumentation and laboratory testing was compiled from the consulted references and reflects what is reported therein, without claiming to be exhaustive.

Table 3. Main characteristics of the of historical cases involving Earth and Rockfill dams using the BBM

Dam and reference	Instrumentation available	Laboratory tests available	Geometry / Materials
Beliche Dam (ALONSO; OLIVELLA; PINYOL, 2005)	Stress cells, piezometers, extensometers, surface settlement markers	Oedometer and triaxial tests	Central core of low-plasticity clay stabilized by two rockfill shells; inner shell of lightly compacted fractured schists, outer shell of compacted greywacke
El Infernillo Dam (ALONSO; OLIVELLA; HUGAS, 2005)	Cross-arms, inclinometers, horizontal extensometers, piezometers, accelerographs, seismoscopes, reference monuments	Triaxial tests (CU and UU), oedometer tests, shear tests	Core of compacted sandy silt of medium plasticity; filters made of sand; shells of compacted and dumped rockfill
Lechago's Dam (ALONSO *et al.*, 2011; COSTA; ALONSO, 2009)	Vibrating wire piezometers, hydraulic settlement gauges, total stress cells, surface topographic marks, leveling points	Oedometer tests (with and without inundation, with suction control), triaxial tests (saturated and under RH control), Brazilian tests, soil water retention curves, permeability tests	Central compacted clay core, protected by granular filters and wide rockfill shoulders
Denis Perron Dam (KOLEV, 2017)	Pneumatic piezometers, total stress cells, inclined and vertical inclinometers, observation terminals	Triaxial-permeability tests, oedometer tests	Rockfill dam with central till core, filters, and transition zones
Albagés Dam (PINYOL; ALONSO, 2019)	Total stress cells, settlement measurements, piezometers	Permeability tests, triaxial tests, direct shear tests, ring shear tests, oedometer tests	Zoned earth dam with central symmetric compacted silty clay core; shoulders of compacted claystone; upstream rockfill mantle; downstream rockfill foot

The historical cases mentioned earlier were all simulated using the BBM, the model also employed in this research. Dam-related issues also have been analyzed in the literature through coupled hydro-mechanical analyses using other mechanical approaches. Alonso and Batlle (1995) describe the construction and impoundment of Limone Dam (Spain) using the concept of state surface (MATYAS; RADHAKRISHNA, 1968), providing an accurate representation of the collapse of unsaturated soils during monotonic confining load and wetting processes. Chen et al (2015) used the Mohr-Coulomb yield criterion (CHEN; ZHANG, 1991) to simulate the sequential construction and impoundment of a high embankment dam. However, the authors emphasized that an elasto-plastic constitutive model is required to capture successfully the influence of soil collapse.

Coupled hydro-mechanical analyses are also useful in issues related to rapid drawdown of upstream reservoirs in earth dams and embankments. The water level changes during dam's operation, modifying the safety factor of the upstream slope. A reduction of the water level, particularly during a rapid drawdown, leads to the removal of the external confining stress from the embankment's surface. This reduction diminishes the stabilizing external hydrostatic pressure and modifies the internal pore water pressure. The pore pressure within the dam must adjust to the new hydraulic boundary condition imposed by the change in the water level. Additionally, a rapid drawdown could increase the shear stress due to the removal of the confining stresses.

Traditionally, there is two different approaches to predict the pore pressure regime after a rapid drawdown: undrained analysis and flow method. The former is applied to cases of impervious soils slope, where pore pressure does not dissipate during the changes in water level. The second method calculates the pore water pressure during drawdown by solving the flow problems caused by the change in hydraulic boundary conditions, assuming that the soil skeleton is rigid, i.e., no mechanical equation is solved, and no effects of soil deformation during drainage are considered. However, these two approaches oversimplify the behavior of the natural and compacted dam soil, as they do not behave as rigid or undrained soils. In practice, these approaches do not approximate the real behavior of the soil in the field.

Rapid drawdown creates a time-dependent seepage and internal stress condition. Changes in total stresses boundary result in a new distribution within the earth dam slope. This stress reduction causes a change in pore pressure, dependent on the stress-strain behavior of the soil skeleton. If the soil skeleton exhibits elastic behavior, changes in the pore pressures results in a change in mean stress. Additionally, shear effects generate additional pore water pressure in cases where dilatancy occurs. The soil behavior during changes in water level, especially during rapid drawdown, justifies the need for estimating pore pressure changes as a function of the coupled effect of the hydraulic boundary changes and changes in both normal and shear stress (ALONSO; PINYOL, 2016; PINYOL; ALONSO; OLIVELLA, 2008; TURKSON; VANDENBERGE, 2023).

Pinyol, Alonso and Olivella (2008) and Alonso and Pinyol (2016) provided reference examples on coupled analyses. Pinyol, Alonso and Olivella (2008) conducted an analysis of the rapid drawdown of a hypothetical slope, considering the elastic constitutive law for both an instantaneous drawdown and a drawdown rate of rate of 0.5 m/day, a common scenario in dam engineering. In their study, they examined three different elastic soil moduli and compared coupled and uncoupled analyses

The authors also discussed the application of elastoplastic models, such as the BBM, for the analysis of rapid drawdown. While drawdown typically leads to a reduction in mean stress, in some cases the geometry of the problem and the non-uniformity of applied boundary stress conditions can result in significant shearing. The reduction in pore pressure implies an increase in effective confining stress. This could lead to plastic deformation if the yield conditions are met (Figure 4).

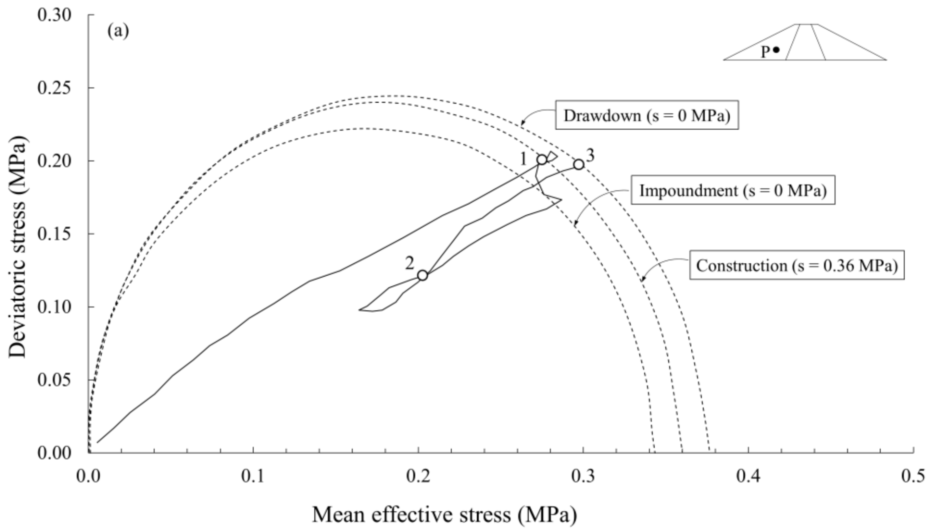

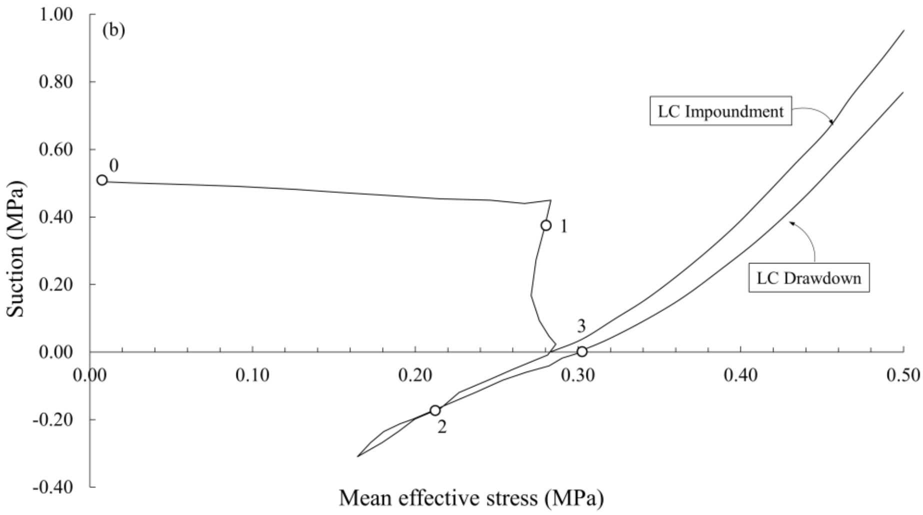

Figure 4. Stress-suction path during: 0-1, construction; 1-2, impoundment; and 2-3, drawdown. (a) Effective mean stress versus deviatoric stress path; (b) Effective mean stress versus suction path (PINYOL; ALONSO; OLIVELLA, 2008)

Finally, Pinyol, Alonso and Olivella (2008) analyzed the Glen Shira Dam (northern Scotland), an well documented case of rapid drawdown. The simulation employed an elastoplastic model and revealed that upon the completion of dam construction, the reservoir impoundment triggered a reversal of the stress path, transitioning into the elastic zone. Throughout the drawdown phase, the stress path remained within the elastic locus, as the dam exhibited a stable geometry, and shear stresses within the dam were relatively small. For this case, a simpler elastic approach is enough to provide a good approximation to the recorded water pressure, but the full elastoplastic simulation provides a thorough understanding of the phenomena during construction and impoundment. The difficulty of predicting the distribution of pore pressure using simplified approaches during and after a rapid drawdown is also presented in Alonso and Pinyol (2016).

Stability analyses during rapid drawdown are crucial due to the risk of slope failure from excess pore pressures if not rapidly dissipated (TURKSON; VANDENBERGE, 2023). The authors assessed the stability during rapid drawdown by using predicted pore pressure from a coupled flow-deformation analysis using the BBM. This analysis was applied to both a hypothetical geometry and the failed Sparmos Dam (located in Greece). The Sparmos Dam coupled flow-deformation analysis provided the most reasonable safety factor compared to other conventional rapid drawdown methods.

Once again, the cases discussed here highlight the analysis of rapid drawdown scenarios employing coupled hydro-mechanical analysis, with the BBM as the mechanical model. However, these problems can also be investigated using alternative mechanical models, as exemplified in Sica, Pagano and Rotili (2019).

Lastly, the final group identified in the literature review focuses on enhancements in the analysis of dams through coupled hydro-mechanical numerical simulation of dams and embankments, using the BBM as a mechanical model.

Poorly compacted earth dams, especially emergency dams, are susceptible to drastic collapse during the first impoundment. In such cases, suboptimal compaction conditions and inadequate water content can result in a meta-stable and collapsible soil structure (DE FARIAS; CORDÃO NETO, 2010). The authors conducted simulation covering all design stages of a hypothetical earth dam 30 meters in height, with stress level sufficient to trigger relevant collapse displacements, varying the compaction condition (soil at optimum condition, at dry of optimum condition and mixed section, combining both soils). Additionally, the safety factor at the end of the analysis was calculated using the limit equilibrium method. The stress and pore pressure fields obtained from the finite element analysis were imported into a slope stability program.

The results from De Farias and Cordão Neto (2010) revealed differences in pore pressure distributions for sections with varied compaction condition, attributed to the influence of the compaction conditions on the material parameters and state variables. They demonstrated that designing a mixed section, composed of poorly compacted material in less stressed zones, is an economically viable alternative. The safety factors underscored the importance of considering coupled hydro-mechanical effects in collapsible dams. In all compaction conditions, the safety factors from the uncoupled analysis were higher than those from the coupled analysis.

The conclusion reached by De Farias and Cordão Neto (2010) did not account for any soil variability and was solely based only on the deterministic factor of safety. To addresses this gap, Amaral, Loyola and Cordão Neto (2020) introduced a probabilistic approach to the analysis performed by de Farias and Cordão Neto (2010), considering the variability of the BBM parameter, whose uncertainties were assumed to arise from statistical errors due to laboratory limitations. The authors evaluated the parameters sensibility and analyzed the behavior of dams constructed with the collapsible soil based on deterministic and probabilistic criteria.

A careful analysis of the literature regarding numerical simulations employing the BBM in dam-related problems revealed the potential of this mechanical model in comprehending the behavior of earth dams. The numerical simulation of historical cases covering construction, impoundment and operation yielded results in line with those observed in the field (ALONSO et al., 2011; ALONSO; OLIVELLA; HUGAS, 2005; ALONSO; OLIVELLA; PINYOL, 2005; COSTA; ALONSO, 2009; KOLEV, 2017; PINYOL; ALONSO, 2019). In addition, numerical simulations play a crucial role in the analysis of rapid drawdown, providing essential information for calculating the stability and safety of earth dams (ALONSO; PINYOL, 2016; PINYOL; ALONSO; OLIVELLA, 2008; TURKSON; VANDENBERGE, 2023).

Finally, some studies presented advances in the analysis of earth dams using numerical simulations, including scenarios involving collapsible soils (DE FARIAS; CORDÃO NETO, 2010), and reliability analysis (AMARAL; LOYOLA; CORDÃO NETO, 2020).

However, upon reviewing the literature, despite the presence of well-supported examples for the design, construction and operation of earth dams, none of them address the hypothesis of settlement caused by the drying phenomenon, as explored in this study. The analysis of historical data from Itaipu significantly advances the field of numerical simulations in the context of earth dams. Moreover, studies that applied advanced models like the BBM, in dam-cases, are generally not supported by experimental data obtained through suction-controlled tests. Instead, parameter calibration is commonly carried out by back-analysis using conventional tests results without suction control. In this context, the present study provides a novel contribution by numerically analyzing the hydro-mechanical behavior of an existing structure by combining laboratory characterization based on unsaturated soil mechanics and coupled finite element simulations.

4 ITAIPU'S LEFT BANK EARTH DAM – HISTORICAL INFORMATION AND CASE DESCRIPTION

Itaipu Binational Hydroelectric Power Plant (HPP) is situated along the Paraná River, with its right bank located on Paraguay and the left bank in Brazil. It began operating in 1984 and, according to data from 2024, accounted for approximately 6.7% of Brazil's total energy consumption and 77.9% of Paraguay's (ITAIPU BINACIONAL, 2025).

The HHP complex encompasses a variety of dam structures. On the right bank, the damming starts with 872 meters-long earth dam, reaching a maximum height of 25 meters. Subsequently, the spillway, which has 14 gates and a maximum discharge capacity of 62200 m^3/s. The main concrete structure is a counterfort-type and relieved gravity-type concrete blocks, with a maximum height up to 196 meters. The dam also includes sections of solid gravity-type concrete structures and another section of counterfort-type concrete blocks. It continues to a rockfill structure with a clay core, gradually transitioning to the earth dam on the left bank, which extends 1989 meters until reaching the natural terrain on the left abutment (Figure 5) (RODRIGUES, 2017). This study focuses particularly on the left bank earth dam of Itaipu.

4.1 Geometry and typical geological sections

The left earth dam has two distinct sections distinguished by their geometries: the so-called "first section", exceeding a height of 10 meters, and the "second section", with a maximum height of 10 meters. Between these sections lies a transitional section measuring 150 meters in length. The first section is 483 meters long and extends from stations 122+47.17 to 127+30.00. The second section, 1357 meters long, runs from station

128+80.00 to station 142+36.50, where it meets the natural ground level. The total length of the left earth dam is 1990 meters.

This study focuses on station 135+50.00, situated within the second section of the left earth dam. It is a compacted homogeneous plastic clay with a high of 10 meters and 1V:3H slope both upstream and downstream and no berms. Figure 6 illustrates the geometry of station 135+50.00.

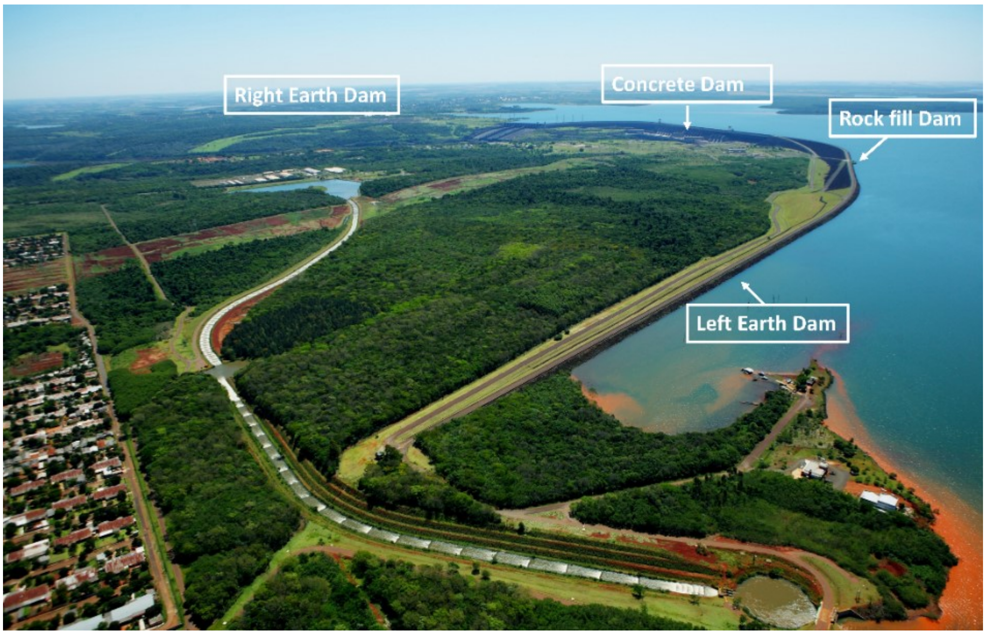

Figure 5. Itaipu Binational Hydroelectric Power Plant (ITAIPU BINACIONAL, 2017)

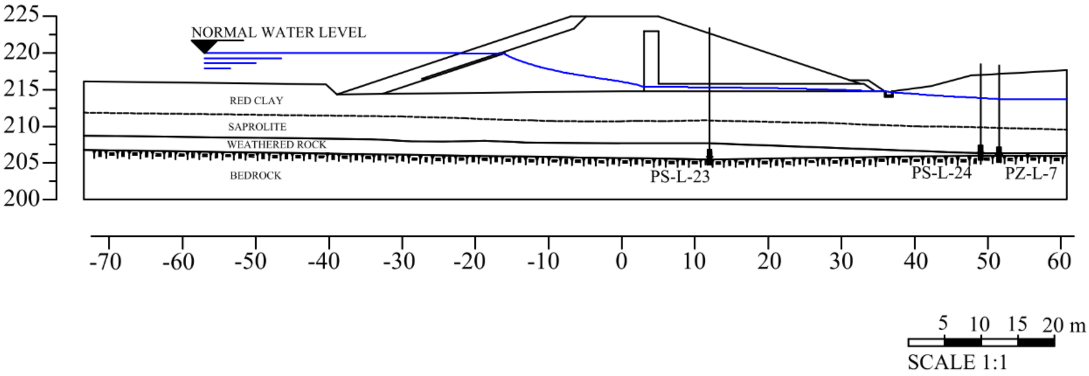

Figure 6. Geometry of the section at station 135+50.00

The Itaipu dam is supported by basaltic flows from the *Paraná* Basin, specifically from the *Serra Geral* Group. The residual soil and weathered rocks resulting from the decomposition of basalt form what is referred to as the Weathering Profile, upon which the earth dam is fully supported. The typical foundation profile of the left bank earth dam of Itaipu consists of three distinct layers: residual soil, weathered basalt, and bedrock.

4.1.1 *Residual Soil*

The residual soil occupies the entire foundation area of the left earth dam and consists of three distinct horizons: mature red clay, transitional soil, and saprolite.

The uppermost and most developed horizon is the mature red clay, with a typical thickness ranging from 3 to 11 meters and average depth of 7 meters.

The transitional horizon is a mixture of materials from the upper red clay horizon and the lower saprolite horizon. It is easily identified by its yellowish color and has an average thickness of 3 meters, occasionally reaching up to 6 meters.

Lastly, the saprolite forms the deepest horizon of the residual soil. It represents the youngest stage of weathering and has traces of the bedrock's structure. The saprolite has an average thickness of 6 meters, varying from 1 meter to 17 meters. In some surveys, this horizon may be absent.

4.1.2 *Weathered basalt and Bedrock*

Immediately beneath the residual soil lies the weathering basalt, which is divided into two horizons: the upper horizon is a transition zone between saprolite and partially weathered rock, while the lower horizon is a partially weathered rock. The average thickness of the weathering basalt layer is one meter, ranging from a few centimeters to 2 meters.

Below the Weathering Profile lies the bedrock layer, formed by a dense, slightly fractured basalt. The upper basalt flow exhibits minimal fracturing and has a rock quality index (RQI) exceeding 85%. These characteristics confer impermeability upon the foundation basalt layer.

4.2 Historical data

The materials used in constructing the earth dam underwent laboratory and in situ tests during the design phase. These tests included characterization and compaction tests, permeability test, consolidation tests with and without inundation, as well as triaxial compression tests, including consolidated and drained (CD), consolidated and undrained (CU), and unconsolidated and undrained (UU) types.

Table 4 and Table 5 summarize the test results conducted during the design phase of the earth dam and are part of the historical data of the Itaipu dam (REPORT 4280.50.8007-E-R0, 1992).

Table 4 presents the key properties of the red clay and saprolite, constituting the natural foundation soils. The red clay is an inorganic, highly plastic (CH) soil with low penetration resistance. It contains a high clay fraction, approximately 10–12% silt, and the remainder sand. This horizon represents the most mature soil layer, where weathering is more advanced. From a mineralogical perspective, the red plastic clay is composed mainly of rounded to subrounded quartz clasts with a well-defined crystalline habit, and ferruginous limonite nodules. Its formation occurred *in situ*, with no evidence of transport, as a result of the weathering of an amygdaloidal basalt, in which quartz-filled amygdales remained unaltered due to the inert nature of quartz. Quartz crystals may also have formed from silica released during feldspar decomposition, which filled larger cavities, while limonite nodules resulted from leaching processes (REPORT 4280.50.8003-E, 1977). The swelling test under inundation conditions indicated that the soil does not exhibit expansive behavior, with a recorded pressure of 235 kPa (REPORT 2063.50.0253.P, 1979).

The saprolite is a highly plastic inorganic sandy-silt-clay (MH), with a porous structure and high permeability. These characteristics enable the saprolite to behave as a natural drain, facilitating preferential water percolation through this layer.

Table 5 presents the key characteristics of the plastic clay used in the compacted massif and the artificial sand used in the filter. The compacted massif was constructed using plastic clay sourced from the borrow area known as *Pomba-Quê*, situated 500 meters away from the construction site. Building the compacted massif required rigorous quality control over the construction method and compaction procedures. Layers were built with a loose soil thickness of 15 cm, resulting in compacted soil layers of 10 cm after compaction by roller passes. Compaction progress was monitored using the Hilf method, and samples were systematically collected for laboratory testing (REPORT 2061.50.1757.P, 1982). The water content deviation (Δw) and the relative compaction (RC), as specified in the design phase according to the normal Proctor, were set at $\Delta w = \pm 2\%$ and RC $\geq 95\%$. The overall average water content deviation was 0.38% below the optimum water content and the RC was 99.83% at the end of the construction. The average thickness of the compacted layer was 10.2 cm (REPORT 2061.50.1757.P, 1982).

The filter was constructed using artificial sand from crushing basalt obtained during mandatory excavations. Post-compaction, the relative compaction reached 90%, surpassing the minimum RC specified in the design phase by 25%.

Table 4. Key properties of the red clay and the saprolite – Historical data (Report 4280.50.8007-E-R0, 1992)

	Plastic Red Clay (CH)	**Saprolite (MH)**
Liquid Limit, LL (%)	63	73
Plasticity Index, PI (%)	38	27
Specific gravity, G	2.95	3.03
Clay fraction (%)	68	42
Silt fraction (%)	19	36
Sand fraction (%)	12	20
Gravel fraction (%)	1	2
Natural water content, *w* (%)	28	46
Dry density, ρ_d (g/cm^3)	1.23	1.22
Natural degree of saturation, S_r (%)	51.6	89.1
Specific mass of saturated soil, ρ_{sat} (g/cm^3)	1.82	1.84
Saturated soil water content, w_{sat} (%)	39	49
Void ratio, e	1.489	1.621
Porosity, n (%)	59.8	68.8
Coefficient of permeability, k (m/s)	4.4×10^{-7}	2.5×10^{-5}
Pre-consolidation stress, σ_v (kPa)	181	840
Friction angle (CU), ϕ (°)	23	-
Soil cohesion (CU), c (kPa)	10	
Friction angle (CD), ϕ (°)	25	-
Soil cohesion (CD), c (kPa)	0	

Table 5. Key properties of the red clay used in the compacted massif and the artificial sand used in the filter – Historical data (Report 4280.50.8007-E-R0, 1992)

	Plastic Red Clay (CH)	**Artificial sand**
Liquid Limit, LL (%)	59	-
Plasticity index, PI (%)	33	-
Specific gravity, G	2.82	3.00
Clay fraction (%)	79	0
Silt fraction (%)	13	31
Sand fraction (%)	7	50
Gravel fraction (%)	1	47
Maximum dry density, $\rho_{d,max}$ (g/cm^3)	1.50	2.00
Optimum water content, w_{opt} (%)	29.3	-
Degree of saturation, S_r (%)	91.4	-
Specific mass of saturated soil, ρ_{sat} (g/cm^3)	1.94	2.25
Saturated soil water content, w_{sat} (%)	29.0	19.0
Void ratio, e	0.90	0.56
Porosity, n (%)	47.4	37.0
Coefficient of permeability, k (m/s)	4.4×10^{-7}	8.0×10^{-1}

Pre-consolidation stress, σ_V (kPa)	541	-
Friction angle (CU), (°)	27.4	-
Soil cohesion (CU), (kPa)	52	
Friction angle (CD), (°)	27.4	-
Soil cohesion (CD), (kPa)	54	

4.3 Updating historical data – Unsaturated Soil Mechanics

The parameters used in the actual design of the dam were obtained from laboratory and in situ tests employing traditional soil mechanics concepts. Although very valuable, these results do not encompass the unsaturated soil condition, as compacted soils are inherently unsaturated.

Analyzing soils under unsaturated condition, incorporating the state variables suction and net mean stress, enables the evaluation of their behavior regarding shear strength, deformability and flow in soils subject to suction variation. The survey of geotechnical parameters using laboratory techniques that allow knowledge and control of the state variables of unsaturated soil also enable the use of more modern and sophisticated techniques for analyzing soil behavior. These include numerical simulations and finite element methods, allowing the consideration of mechanical and hydraulic models suitable for evaluating the behavior of unsaturated soils.

In this context, Mello (2022) undertook an experimental study to update the mechanical and hydraulic geotechnical parameters of the soil used in the construction of the left bank earth dam of Itaipu. The experimental framework used concepts and laboratory techniques of unsaturated soil mechanics. The laboratory tests carried out included soil characterization and compaction; determination of the soil water retention curve (SWRC); permeability test; oedometric and triaxial compression tests saturated and with suction control; and, volumetric drying shrinkage tests. The findings from Mello (2022) will be detailed here, as they were used to calibrate the mechanical and hydraulic parameters used in the numerical simulations of the left earth dam carried out in the present study.

Sampling was conducted upstream of the left earth dam, near the *Pomba-Quê* borrow area, in the form of deformed samples for the tests representing the compacted massif, and undisturbed samples for the tests representing the foundation clay. The soil was compacted in the laboratory following field compaction control information, with RC = 98% and Δw = -1%.

Table 6 provides an overview of the primary characterization and compaction results of the soil, classified as a dark purple slightly silty clay with high plasticity (CH), according to the Unified Soil Classification System (USCS).

Table 6. Summary of the key properties of the studied soil (MELLO, 2022)

Liquid Limit, LL (%)	67
Plasticity Index, PI (%)	36
Specific density, G	2.68
Clay fraction (%)	76.2
Silt fraction (%)	15
Sand fraction (%)	8.8
Optimum water content, w_{opt} (%)	27.8
Maximum dry density, $\rho_{d,max}$ (g/cm^3)	1.5

Mello (2022) determined the soil water retention curves (SWRC) for both undisturbed and compacted soil, covering both drying and wetting paths. The experimental data points for the drying path were obtained by combining the suction plate and filter paper techniques. The experimental points for the wetting path were determined using only the filter paper technique. The SWRC for all cases were fitted using the multimodal retention curve model (CASINI; VAUNAT; ROMERO, 2012), with the fitting parameters detailed in Table 7. Figure 7 and Figure 8 illustrate the SWRC for the compacted and undisturbed soils, respectively.

Table 7. SWRC fitting parameters for both undisturbed and compacted soil, and for drying and wetting paths

	Undisturbed Drying	**Undisturbed Wetting**	**Compacted Drying**	**Compacted Wetting**
M_{RC}	0.194	0.295	0.127	0.130
P_M (MPa)	4.32×10^{-3}	0.008	0.010	2.99×10^{-3}
m_{RC}	0.794	0.781	0.870	0.793
P_m (MPa)	16.264	15.200	20.306	15.171
w	0.654	0.578	0.620	0.566
S_{rl}	0.0	0.0	0.0	0.0

M_{RC} = Shape coefficient of the macrostructural SWRC; P_M = Air entry value of the macrostructural SWRC; m_{RC} = Shape coefficient of the microstructural SWRC; P_m = Air entry value of the microstructural SWRC; w = weight; S_{rl} = Residual saturation

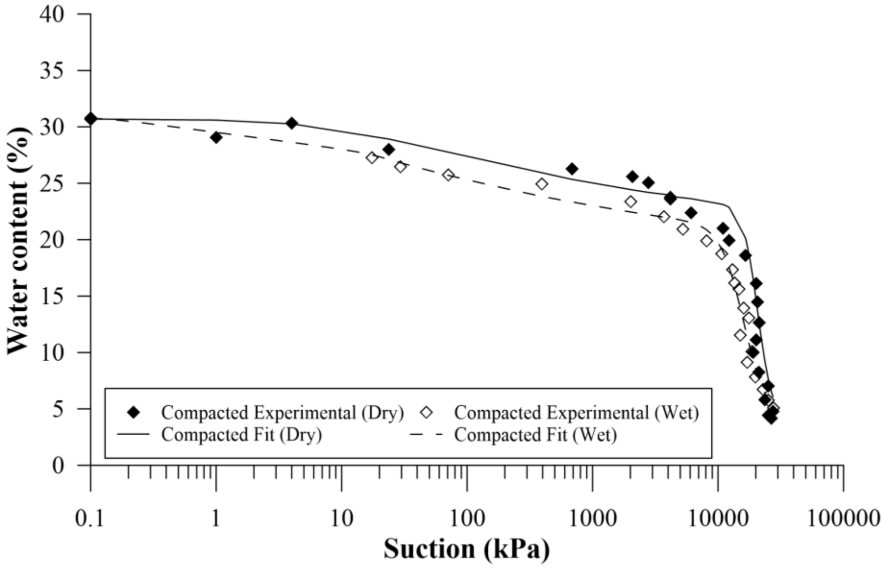

Figure 7. SWRC for the compacted soil: drying and wetting paths – Experimental data points and fitting curves (modified from MELLO, 2022)

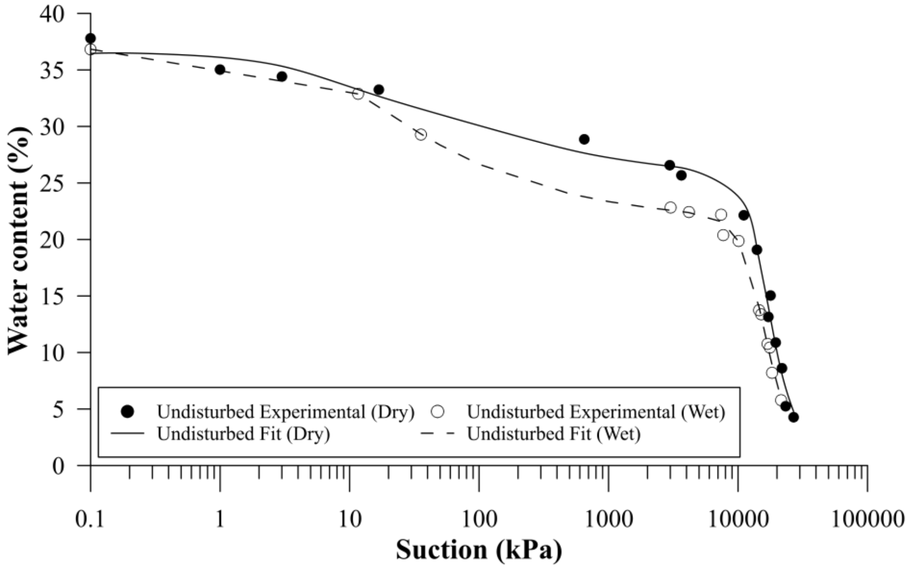

Figure 8. SWRC for the undisturbed soil: drying and wetting paths – Experimental data points and fitting curves (modified from MELLO, 2022)

The curves exhibit slight desaturation in the initial zone, with significant desaturation occurring primarily at high suction values, approximately 10 MPa. These characteristics are typical of plastic clays with high water retention capacity. Additionally, the soil retention curves reveal the presence of hysteresis for both undisturbed and compacted soil, resulting in higher water content values for a given suction along the drying path compared to the wetting path.

Mello (2022) carried out permeability tests using the flexible wall permeameter test under isotropic confining stresses of 0, 50, 100, 200 and 300 kPa. Table 8 presents the calculated values for intrinsic permeability (m²), which are of interest for calibrating hydraulic model parameters. Unlike permeability (typically expressed in m/s), intrinsic permeability depends solely on the properties of the solid matrix, disregarding fluid properties.

Table 8. Intrinsic permeability (m²) under different confining stresses for both compacted and undisturbed soil (modified from MELLO, 2022)

	0 kPa	**50 kPa**	**100 kPa**	**200 kPa**	**300 kPa**
Compacted	3.5×10^{-16}	8.3×10^{-17}	3.9×10^{-17}	3.0×10^{-17}	2.2×10^{-17}
Undisturbed	1.4×10^{-12}	1.2×10^{-12}	7.4×10^{-13}	2.0×10^{-13}	1.7×10^{-13}

The experimental set of mechanical tests included oedometer and triaxial compression tests, both conventional and with suction control. It also included volumetric drying shrinkage tests. All the mechanical tests were performed on undisturbed samples representing the soil foundation and compacted samples representing the compacted massif. Similar to the hydraulic tests detailed earlier, the samples were compacted according to reference values obtained from field compaction control.

The oedometer tests were carried out on saturated soil samples and soil samples subject to constant and controlled suction, using the axis translation technique, at a value of 200 kPa. Figure 9 and Figure 10 depict the results of the conventional saturated and controlled suction oedometer tests for compacted and undisturbed soil, respectively.

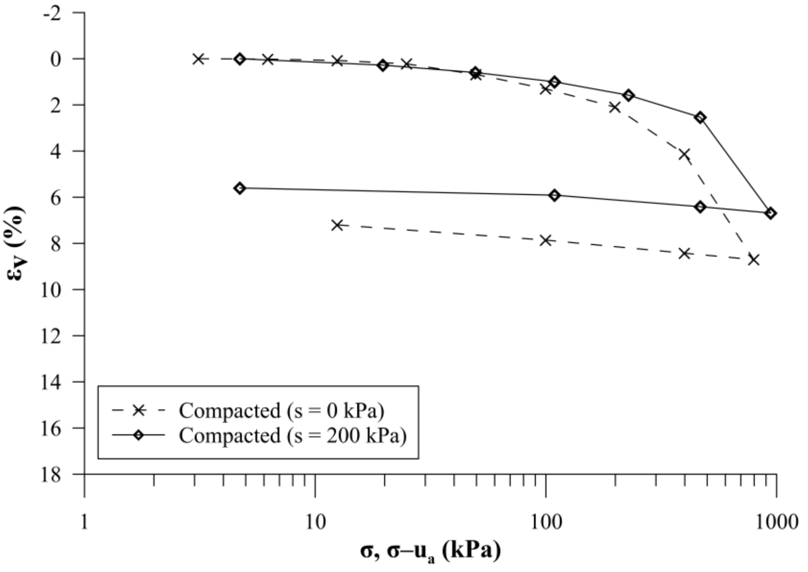

Figure 9. Oedometric curves for compacted soil – Conventional oedometer test (s = 0 kPa) and suction-controlled test (s = 200 kPa) (MELLO, 2022)

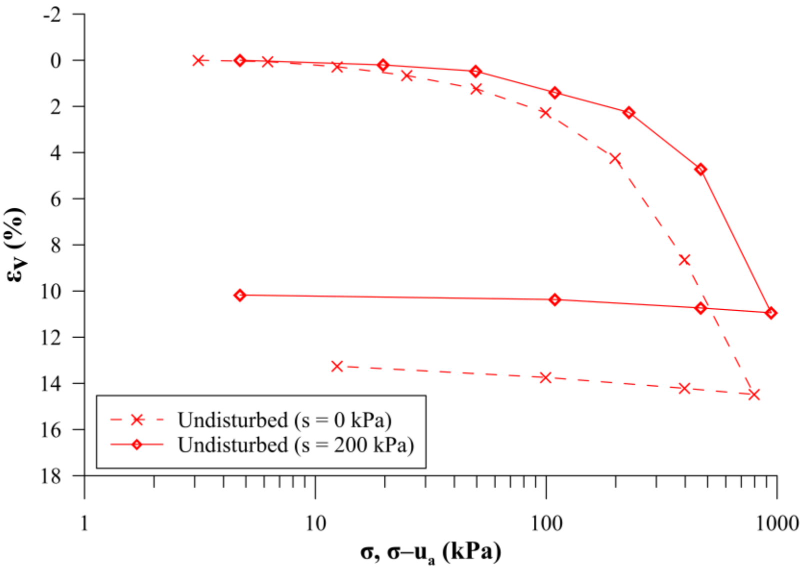

Figure 10. Oedometric curves for undisturbed soil – Conventional oedometer test (s = 0 kPa) and suction-controlled test (s = 200 kPa) (MELLO, 2022)

The compacted clay soil, representative of the compacted massif, exhibited a collapse potential of less than 2% for the range of stresses analyzed. The undisturbed soil, representative of the foundation, showed a collapse potential of more than 2% only for stresses greater than 400 kPa. In practice, the stresses are lower than this value and the foundation soil remains saturated during the operation of the dam, indicating the impossibility of recent collapse due to inundation.

Shear strength was evaluated through consolidated and drained (CD) triaxial compression tests. Mello (2022) conducted these tests on both undisturbed and compacted soil samples under saturated conditions (conventional test) and under controlled suction of 200 kPa. The confining stresses for the saturated conventional test were 100, 200 and 300 kPa; while for the test with controlled suction via the axis translation technique, the confining stresses were 50, 100 and 200 kPa.

Figure 11 and Figure 12 illustrate the resistance envelopes for the evaluated suctions, 0 and 200 kPa, for both the compacted and undisturbed soils, respectively. The resistance of the soil was evaluated using the peak stress, and a summary of the results is provided in

Table 9.

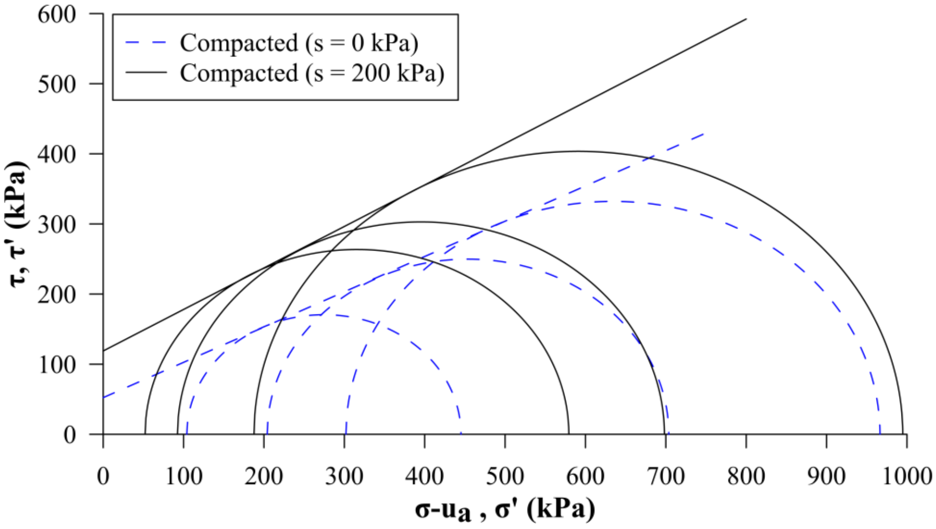

Figure 11. Resistance envelopes for compacted soil – Conventional triaxial test (s = 0 kPa) and suction-controlled triaxial test (s = 200 kPa) (MELLO, 2022)

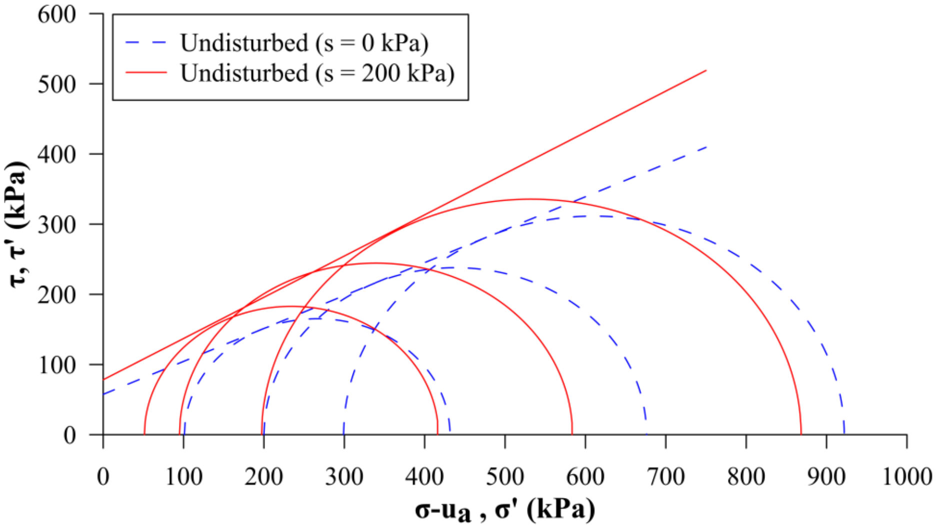

Figure 12. Resistance envelopes for undisturbed soil – Conventional triaxial test (s = 0 kPa) and suction-controlled triaxial test (s = 200 kPa) (MELLO, 2022)

Table 9. Effective resistance parameters for compacted and undisturbed soil – saturated and unsaturated conditions (MELLO, 2022)

		c' (kPa)	**ϕ' (°)**
Compacted Soil (CD test)	**Saturated (s = 0kPa)**	52.3	26.7
	Unsaturated (s = 200 kPa)	118.9	30.6
Undisturbed Soil (CD test)	**Saturated (s = 0kPa)**	57.5	25.1
	Unsaturated (s = 200 kPa)	78.3	30.4

Finally, Mello (2022) investigated the volumetric shrinkage due to drying for both the compacted and undisturbed soil. Figure 13 and Figure 14 illustrate the variation in water content and volumetric strain with suction for compacted and undisturbed soil, respectively.

In both scenarios, volumetric variation induced by shrinkage predominantly occurs in the desaturation zone of the SWRC, specifically for suctions exceeding 10 MPa.

The total volumetric shrinkage for the compacted soil was 10% and for the undisturbed soil was 3.5%. The compacted soil exhibits higher volumetric shrinkage due to drying compared to the oedometric compression deformation in the saturated condition, at 6.6%. These findings suggest that the compacted soil is more susceptible to volumetric variation due drying than external loading, supporting the hypothesis that the settlements observed in the field may have resulted from shrinkage during reservoir drawdown.

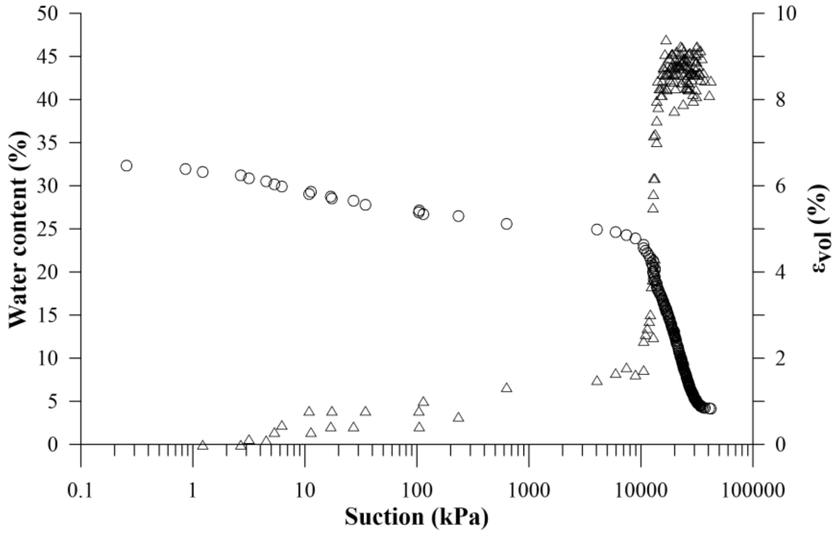

Figure 13. Variation of water content and volumetric strain of the compacted soil with suction during drying shrinkage (modified from MELLO, 2022)

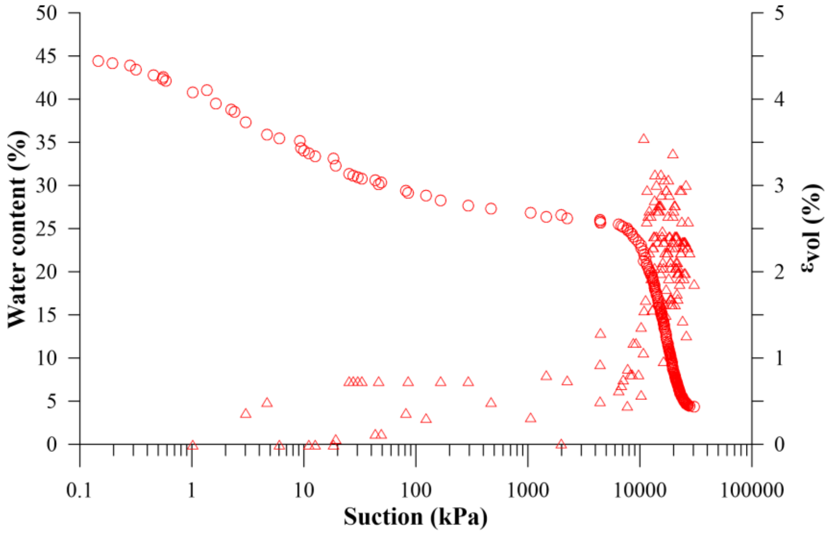

Figure 14. Variation of water content and volumetric strain of the undisturbed soil with suction during drying shrinkage (modified from MELLO, 2022)

Further details regarding the laboratory tests carried out on the soil samples representative of the foundation and compacted massif of Itaipu dam are described in Mello (2022).

4.4 Instrumentation and measurements

Instrumentation installed in dams plays a crucial role in assessing the structure's performance during the construction and operation phases. An adequate set of instrumentation enables accurate monitoring, evaluating of the dam's safety condition, validating design assumptions, and assessment of potential interventions.

The left bank earth dam of Itaipu has various instruments including standpipe (PS-L) and electric piezometers (PG-L), water level gauges (PZ-L), settlement gauges (MA-L), survey markers (MR-L), and flow meters (MV-L). The original nomenclature employed during the project phase has been retained herein.

The specific section analyzed in this study, station 135+50, has two standpipe piezometers and one water level gauge. The location of these instruments is illustrated in Figure 6. Additionally, there are two settlement gauges installed in the compacted massif.

The coupled hydro-mechanical analysis of the earth dam's behavior at station 135+50 required knowledge of the data of the piezometers, settlement gauges and information from survey markers installed near station 135+50. These results will be detailed here.

4.4.1 ***Standpipe Piezometer***

Two standpipe piezometers, designated as PS-L-23 and PS-L-24, are installed at station 135+50 (Figure 6). These piezometers consist of 0.5-inch PVC pipes and are positioned in the foundation downstream of the dam axis, between the saprolite and the basalt. The monitoring is particularly relevant given the higher permeability of the saprolite compared to the basalt. Measurements of piezometric level, recorded in meters above the sea level (masl), are taken every two weeks (Figure 15).

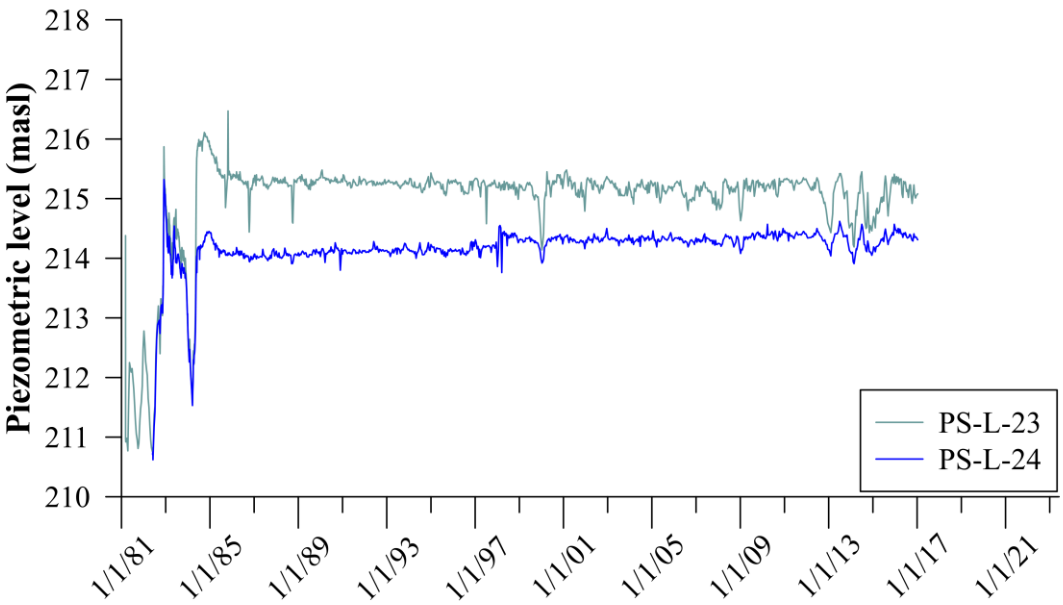

Figure 15. Piezometric level at station 135+50 (PS-L-23 and PS-L-24)

4.4.2 *Settlement gauges*

The settlement gauges determine the vertical displacement of plates installed within the foundation or inside the compacted massif, relative to a fixed reference point. There are two settlement gauges installed in the compacted massif at station 135+50. The first, MA-L-008 (1), is between the foundation and the compacted massif at elevation 214.865m, while the second, MA-L-008 (2), is installed in the middle of the compacted massif at elevation 220.069m.

Readings of these instruments were conducted at regular intervals until 2006, at which point the readings were suspended due to the stabilization of the settlements post-construction of the dam. Sporadic readings were taken after 2006: two in 2014, one in 2018 and 2019, and eight readings in 2020.

Figure 16 shows the settlements that have occurred since the construction of the earth dam and Figure 17 shows the additional settlements post-construction state. In this figure, the settlement measured immediately after construction is subtracted from all subsequent measurements, so that the graph shows only the additional settlements occurring after the construction period. It is apparent that until 2006, settlements remained relatively constant after construction. The sporadic readings taken after 2006 indicate additional settlement of approximately 2 centimeters.

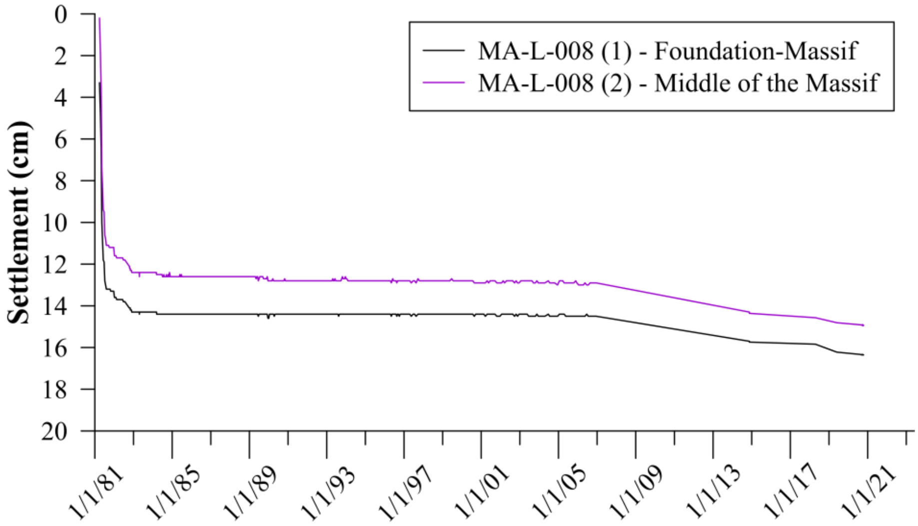

Figure 16. Total settlement recorded by settlement gauges at station 135+50 – MA-L-008

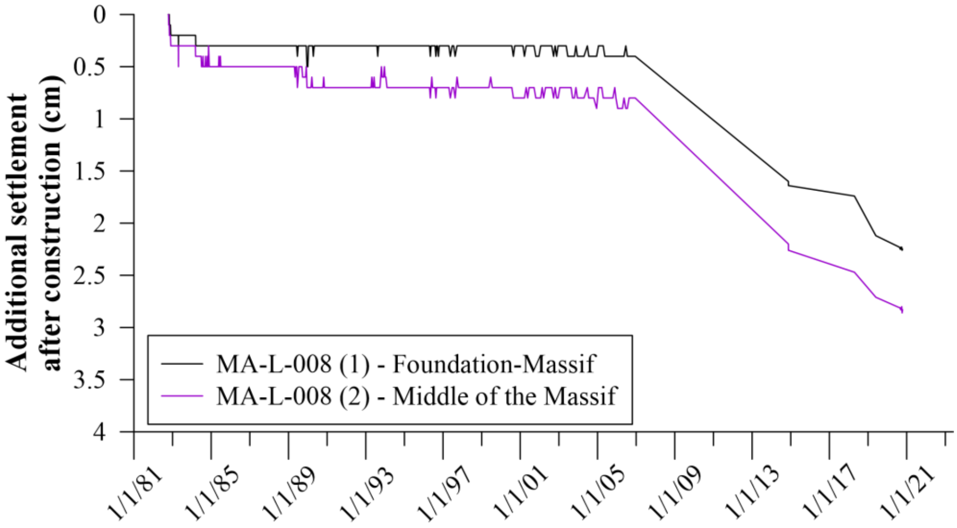

Figure 17. Additional settlement after the construction of the dam recorded by settlement gauges at station 135+50 – MA-L-008

4.4.3 ***Survey markers***

The survey markers installed in the concrete measure the vertical displacements of the earth dam's crest. Survey markers are spaced longitudinally along the left earth dam at intervals of 60 meters, and readings are taken twice a year, usually once in summer and once in winter.

Station 135+50 does not have a specific survey marker. Instead, we used as a reference the data from three nearby survey markers: MR-L-22 (station 135+19), MR-L-23 (station 135+75), and MR-L-24 (station 136+39), whose readings data are shown in Figure 18.

Since the completion of the earth dam’s construction in June 1982, the settlement of the crest has generally remained stable, except for MR-L-23. Between 1999 and 2000, MR-L-23 experienced a settlement of approximately 2.5 centimeters, followed by stabilization. Subsequently, between 2012 and 2015, both MR-L-23 and MR-L-24 recorded a settlement in the dam's crest of around 3 centimeters, which then stabilized once more.

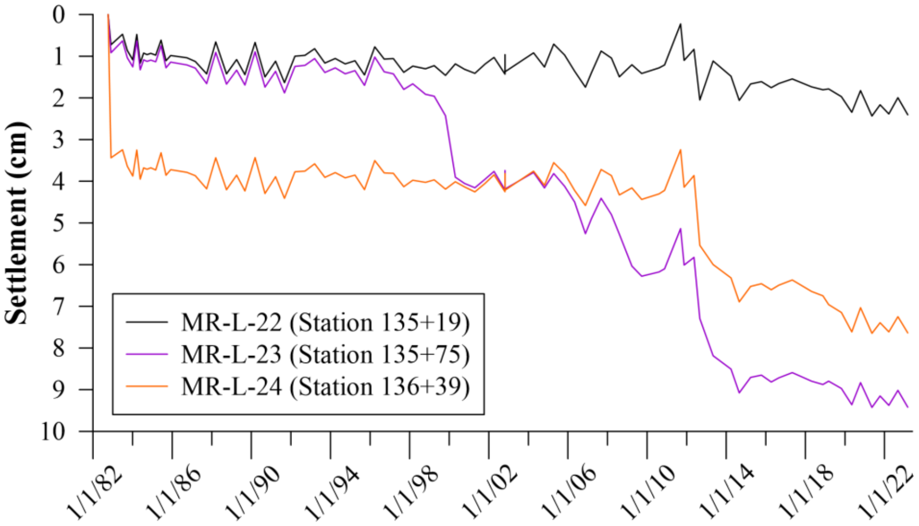

Figure 18. Settlement recorded by the survey markers at the crest near station 135+50

4.5 Motivation for the study case

The reservoir level of the Itaipu dam is measured daily at a station near the dam. The historical data since the initial filling and throughout its years of operation are depicted in Figure 19. The dashed lines represent the operational levels for which the dam was designed, ranging between 219.0 and 220.5 meters above the sea level.

Since its filling in 1985, the dam has operated at its normal design levels 80.4% of the time. Only one measurement has been recorded above the normal value; all other deviations from the normal levels refers to values below the design level.

Figure 19 shows that after its initial filling, the dam operated at normal levels until 1999-2000, when it reached its lowest historical operating level of 215.15 masl. During this period, the reservoir remained below the design level for approximately four months, from November 1999 to March 2000, before returning to the design level with occasional periods of lowering over the following years.

A series of drops in the water level began starting in 2012, keeping the reservoir operating below the design level for an extended period of three years. The reservoir stabilized at the normal operating level again from 2015 onwards (Figure 20). Between October 2012 and October 2015, the dam operated with reservoir water levels below the normal operating level approximately 70% of the time, with a minimum level recorded during this period of 215.45 masl.

During 2012-2015 years, Brazil experienced a water crisis leading to reduced energy production by hydroelectric power plants due to water scarcity. From 2013 to 2015, the Itaipu region underwent above-average rainfall, enabling Itaipu Dam to increase energy production to meet the demands of the *Sistema Interligado Nacional* (SNI). During these years, Itaipu's turbine flow exceeded the inflow, resulting in an extended period of operation below the normal design level (RODRIGUES, 2017).

From 2018 onwards, Itaipu Dam once again operated below the normal design level for an extended period. Between November 2018 and September 2022, the reservoir level remained below normal operating levels for 76% of the time, with a recorded minimum level of 216.40 masl during this period.

The crest settlement of the earth dam has generally remained stable over nearly 30 years of operation, except for MR-L-23 that experienced a settlement of approximately 2.5 centimeters between 1999 and 2000 followed by stabilization. Both MR-L-23 and MR-L-24 recorded a crest settlement of around 3 centimeters between 2012 and 2015 (Figure 18). Understanding the causes of these settlements recorded on the crest during the dam's operation period is crucial, especially since historical records indicated that settlements following construction and reservoir filling had already stabilized. Analyzing settlement patterns after many years of operation not only aids in understanding their causes but also enables the prediction of potential future settlements scenarios.

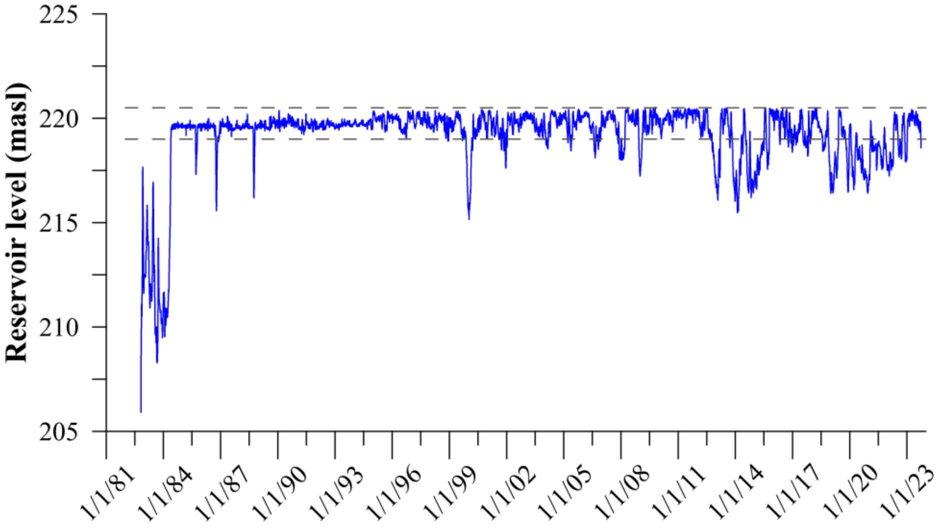

Figure 19. Reservoir level history - 1982 to 2023

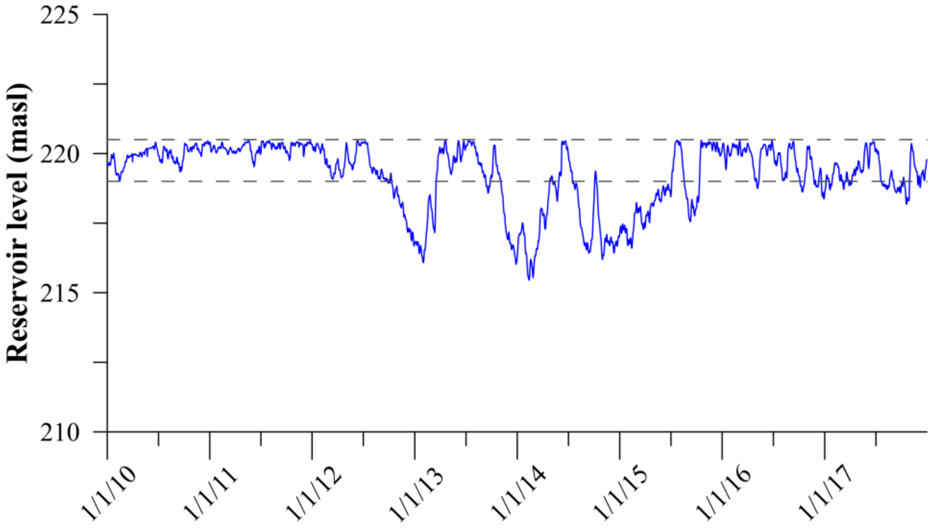

Figure 20. Reservoir level history - 2010 to 2017

By comparing the reservoir level data with the crest settlement records documented by survey markers (Figure 21), settlement may be related with low water levels in the reservoir. Extended periods of low reservoir levels can induce plastic strain due drying. During reservoir drawdown, both the upstream slope and part of the foundation are exposed, as the areas where settlements were observed are located in the final section (closure) on the left abutment of the dam complex.

Therefore, the motivation behind this study is to conduct numerical simulations to investigate the causes of settlement observed at survey makers during the operation of the earth dam. Additionally, the research aims to analyze the coupled hydro-mechanical behavior spanning the entire history of the earth dam, encompassing construction, reservoir filling, and operational phases.

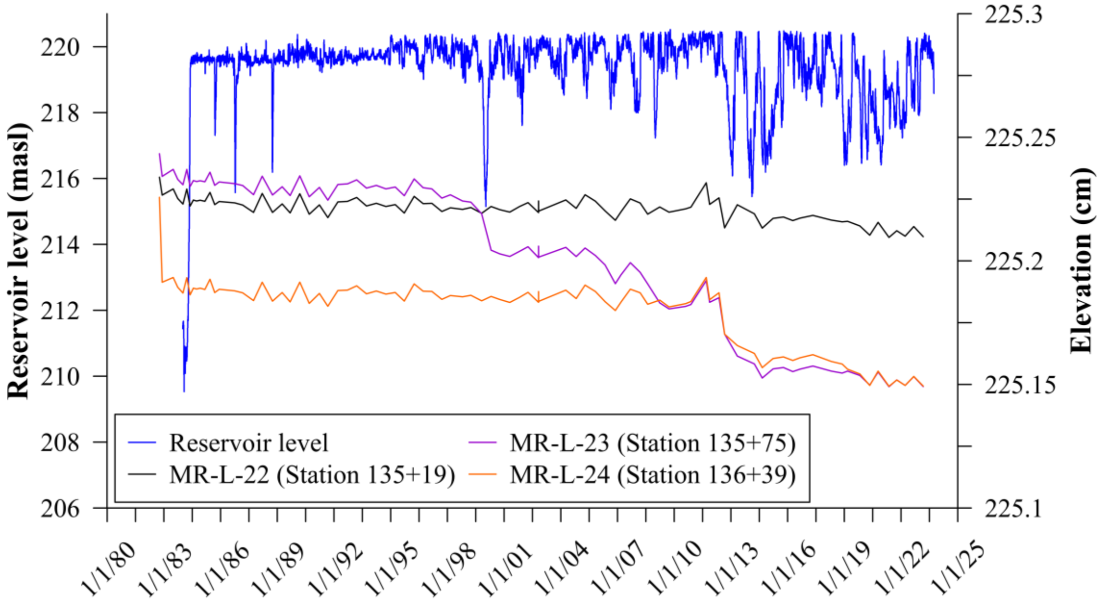

Figure 21. Reservoir level history and settlement recorded by the survey markers at the crest near station 135+50: construction, impoundment and operation

5 NUMERICAL SIMULATION OF THE LEFT BANK EARTH DAM OF ITAIPU

The numerical simulation was set up in the finite element program CODE_BRIGHT. The program handles the modeling of thermo-hydro-mechanical (THM) problems in geological media, whether coupled or not. Section 3.2 provides a summary of the governing equations and constitutive laws applicable to the coupled hydro-mechanical problems of interest in this research.

CODE_BRIGHT uses the GiD interface for pre and post-processing. GiD is a graphical interface that facilitates the preparation and visualization of the numeric problem. The program enables the generation of the finite element mesh and provides all the necessary information and files for initiating numerical simulation calculations directly from the system. These calculations incorporate the defined geometry, material parameters based on the adopted constitutive laws, boundary conditions, and interval time definitions.

5.1 Geometry, zoning and constitutive models

The numerical simulation of the left bank earth dam of Itaipu includes three key stages: construction, impoundment, and operation, covering a 37-years period (from 1980 to 2017). The simulated geometry is based on the typical cross-section at station 135+50, a location of particular interest. This represents a simplification of the original design. The dam stands at a height of approximately 10 meters and reaches an elevation of 225 meters (Figure 22).

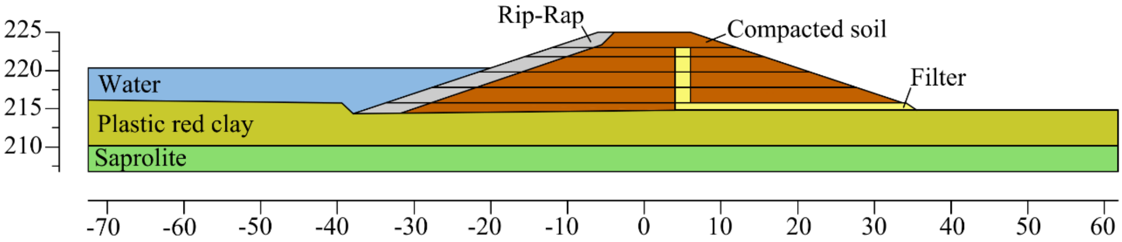

Figure 22. Section 135+50: Itaipu dam material zones and construction sequence for model simulation

Figure 22 also outline the materials forming the earth dam, with horizontal lines representing the idealized layers used in the construction simulation. The overall average thickness of the compacted layer was 10.2 cm, as documented in historical records and reports from the dam's construction. The dam's geometry was divided into multiple layers to facilitate numerical modeling, each with depths ranging from 1 to 2 meters, as depicted by the horizontal lines.

The construction simulation specifically covers the time interval from January 1981 to May 1981 (REPORT 4280.50.8006, 1991), corresponding to the actual dates of construction of this section. During this simulation, the dam layers were systematically constructed by adding layers to the initial foundation geometry. The CODE_BRIGHT program simulates the gradual construction process of the layers, applying the weight of each layer incrementally in intervals until reaching full weight at the conclusion of the construction time interval for each layer. Figure 22 visually captures this construction process and the distinct layers involved in the simulation.

Two constitutive mechanical models were employed to simulate the dam: the linear elastic model (LE) and the Barcelona Basic Model (BBM). The BBM is implemented into different constitutive formulation in CODE_BRIGHT, and in this study, the Thermo-Elastoplastic (TEP) model for soils was used. Table 10 gathered the respective constitutive models assigned to each material zone.

Table 10. Assigned constitutive model to the dam zones

Saprolite	LE
Plastic red clay	BBM
Compacted red clay	BBM
Rip-Rap	LE
Filter	LE
Water	LE

Saprolite is distributed uniformly across the entire dam area, characterized by varying thickness. This soil type is younger and exhibits higher permeability compared to the mature residual soil. In the simulation, the saprolite was modeled within the linear elastic regime, given its pre-consolidation stress of 840 kPa that significantly surpass the stress increase of the compacted massif weight (approximately 200 kPa).

Water was modeled as a linear elastic material. In this approach, water is a highly porous and soft material. Reservoir impoundment and determination of water levels during dam operation gets through the "saturation" and "desaturation" processes of this material using a hydraulic boundary condition linked to water pressure.

This method of simulating water levels has notable advantages. Traditionally, the conventional approach involved calculating pore pressure and its corresponding equivalent mechanical pressure (weight of the water) to simulate the water level position. These boundary conditions were then applied to the foundation's base and the upstream face for each time interval. By simulating water as a porous material, only one hydraulic boundary condition is needed per time interval, eliminating the mechanical boundary condition associated with the weight of the water. From a computational perspective, simulating water as a material reduces calculation time and effort, as only one boundary condition is considered.

The numerical simulation of the construction and impoundment process for the Beliche Dam (ALONSO; OLIVELLA; PINYOL, 2005) employed a methodology requiring the calculation of pore pressure and corresponding mechanical pressures at each stage of reservoir impoundment. In a subsequent study, Kolev (2017) replicated the problem under identical conditions, introducing the methodology where modeled water is a highly porous and soft material. The author confirmed the compatibility of results obtained through both methods.

5.2 Material Parameters

Each material requires a set of parameters related to its mechanical and hydraulic properties, in order to solve the stress equilibrium and mass balance of water equations. These parameters are calibrated based on the selected mechanical and hydraulic constitutive laws, which represent the material behavior. The assignment of material parameters is carried out on the respective surfaces.

The material parameters of the red clay foundation and the compacted soil were calibrated based on laboratory results conducted by Mello (2022) and historical documents detailing tests done during the construction of the left bank earth dam of Itaipu.

Calibrating the mechanical parameters requires results of oedometer tests carried out under suction control conditions. In this case, Mello (2022) carried out both conventional saturated oedometer tests and suction-controlled tests with suction of 200 kPa. Additionally, triaxial tests, also under suction control, were performed at suction levels of both 0 and 200 kPa.

Calibration of hydraulic parameters requires data from soil water retention curve (SWRC) tests and the hydraulic conductivity value. The last one was obtained from the Flexible Wall Permeability test (MELLO, 2022).

5.2.1 *Saprolite*

The mechanical and hydraulic parameters of the saprolite were calibrated using data from Itaipu's reports and historical records. No additional laboratory tests were conducted specifically for unsaturated soil properties within this layer.

Table 4 (section 4.2) gathers the primary characteristics of the saprolite, which were used for parameter calibration. Due to the absence of SWRC test for this layer, a typical curve for porous soils was employed, characterized by high air entry value and high desaturation capacity. The Van Genuchten (1980) unimodal model was applied for the SWRC.

Table 11 and Table 12 summarize the mechanical and hydraulic parameters of the saprolite, respectively.

Table 11. Mechanical constitutive parameter for saprolite

		Saprolite	**Unit**
E	Young Modulus	12.5	MPa
υ	Poisson's ratio	0.3	-
ρ	Solid phase density	3030	kg/m³

Table 12. Hydraulic constitutive parameter for saprolite

		Saprolite	**Unit**
P_0	Measured P at certain temperature	0.01	MPa
λ	Shape function for retention curve	0.5	-
S_{ls}	Maximum saturation	1	-
S_{rl}	Residual Saturation	0	-
$(k_{11})_0$	Intrinsic Permeability	2.5×10^{-12}	m²

5.2.2 *Red Clay – Foundation*

The set of mechanical parameters of the foundation clay were calibrated based on laboratory results carried out by Mello (2022). Conventional and suction-controlled triaxial tests allow determining the slope parameter of the critical state line (M) and the parameter describing the increase in cohesion with suction (k). Conventional and suction-controlled oedometer tests provide calibration of the parameters related to elastic stiffness for changes in stress (κ) and stiffness for changes in stress in the virgin state of saturated soil, λ(0).

The BBM requires a single hardening parameter, p_0^*, denoting the isotropic pre-consolidation net stress under saturated condition. The parameter relates to the pre-consolidation stress obtained from the saturated oedometer test, which is then adjust to fit the BBM model, originally calibrated for isotropic compression.

This set of mechanical parameters enables the visualization of yield curves in (p,q) stress plane (Figure 23), for both investigated suctions. The complete three-dimensional view of the yield surfaces in (p,q,s) plane requires the definition of the Loading-collapse (LC) curve. This curve delimits the region where the soil behaves elastically for both loading and collapse paths. The definition of the LC curve requires the calibration of the parameters r and β, both of which control the shape of the LC curve. Parameter r defines the maximum soil stiffness and parameter β controls the rate of increase of soil stiffness with suction. Figure 24 illustrates the LC curve for red clay soil foundation.

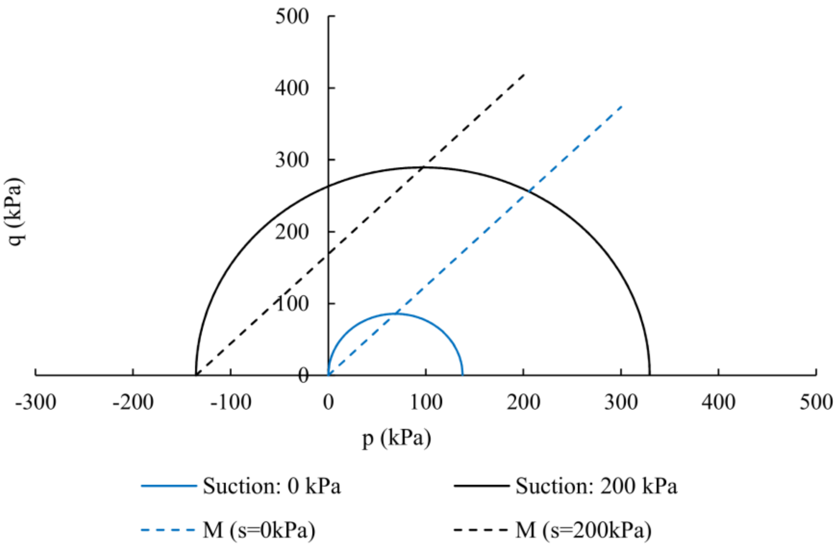

Figure 23. View of the yield curves in (p,q) stress plane for the red clay foundation soil

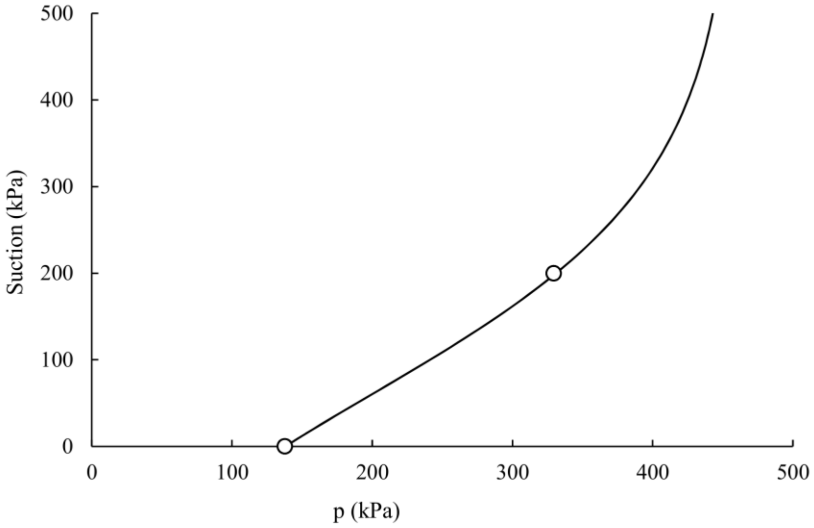

Figure 24. Loading-Collapse (LC) curve for red clay soil foundation – (p,s) stress plane

Table 13 summarizes the BBM mechanical constitutive parameters for the foundation soil. This set of parameters allows the definition of the single yield surface and single plastic potential, and therefore the tree dimensional view of the yield surfaces in (p,q,s) plane.

Table 13. Mechanical constitutive parameter for red clay soil foundation

	Mechanical Constitutive Parameters	**Red Clay - Foundation**	**Unit**
κ	Elastic stiffness parameter for changes in net mean stress	0.010	-
$\lambda(0)$	Stiffness parameter for changes in net mean stress for virgin states of the soil (saturated soil)	0.143	-
$p0^*$	Isotropic pre-consolidation net stress for saturated condition	138.0	kPa
M	Slope of critical state line	1.24	-
k	Parameter describing the increase in cohesion with suction	0.678	-
r	Parameter defining the maximum soil stiffness	0.820	-
β	Parameter controlling the rate of increase of soil stiffness with suction	0.0073	kPa^{-1}
p_c	Reference stress	1	kPa
κ_{s0}	Initial (suction zero) elastic slope for specific volume-suction	4×10^{-3}	-
K_{min}	Minimum Bulk module	5.0	MPa
υ	Poisson's ratio	0.3	-
ρ_s	Solid phase density	2950	kg/m³

The mechanical parameters were validated by numerical simulation of conventional (s = 0 kPa) and suction-controlled (s = 200 kPa) oedometer compression tests. The tests were simulated by means of a one-dimensional mesh, applying an increasing ramp stress to the nodes on the upper face of the soil. Figure 25 gathers the numerically simulated oedometric curves and the experimental points.

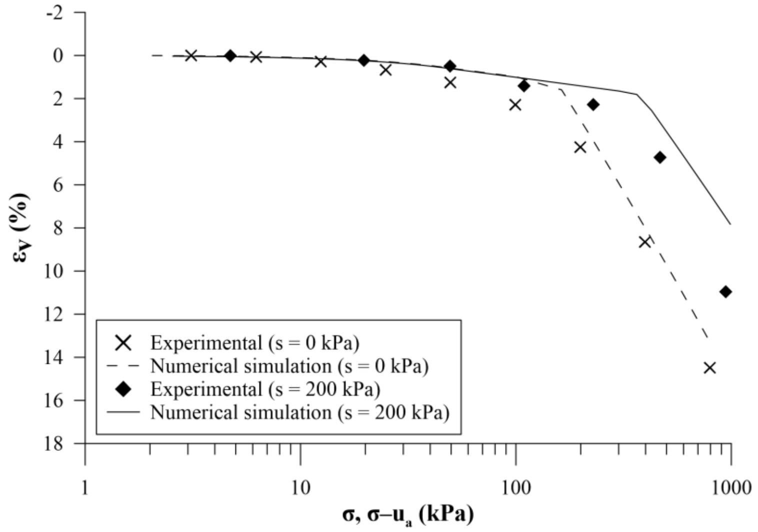

Figure 25. Numerical simulation of the oedometer test for undisturbed soil (red clay - foundation) both saturated (s = 0 kPa) and with suction control (s = 200 kPa)

The set of hydraulic parameters was calibrated using laboratory tests carried out by Mello (2022) and historical data from Itaipu (REPORT 4280.50.8007-E, 1992). The multimodal retention curve model (CASINI; VAUNAT; ROMERO, 2012) was adopted as the retention curve model, as it is a bimodal SWRC. The intrinsic permeability value was defined based on the historical records of tests carried out during the design and construction phase of the earth dam (Table 4). Table 14 lists the hydraulic parameters of the red clay soil foundation used in the numerical simulation.

Table 14. Hydraulic constitutive parameter for red clay soil foundation

Hydraulic Constitutive Parameters		Red Clay - Foundation	Unit
S_{ls}	Maximum saturation	1	-
S_{rl}	Residual saturation	0	-
w	Weight	0.654	-
M_{RC}	Shape coefficient of the macrostructural SWRC	0.194	-
P_M	Air Entry value of the macrostructural SWRC	4.32×10^{-3}	MPa
m_{RC}	Shape coefficient of the microstructure SWRC	0.794	-
P_m	Air entry value of the microstructure SWRC	16.246	MPa
$(k_{11})_0$	Intrinsic Permeability	4.4×10^{-14}	m²
Φ_0	Reference porosity for read intrinsic permeability	0.598	-

The parameters adopted for the SWRC were also evaluated using numerical simulation. The simulated problem consists of a soil column with a high initial suction value, subjected to a constant liquid pressure from saturation to the bottom boundary. The soil water retention curve is obtained at the equilibrium of the liquid pressure (Figure 26).

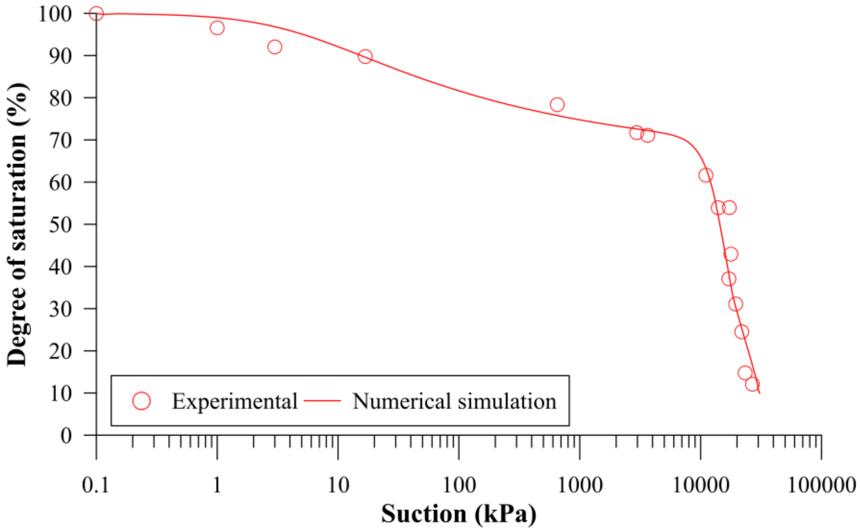

Figure 26. Numerical simulation of the SWRC for undisturbed soil (red clay - foundation)

5.2.3 *Compacted Soil*

The mechanical properties of the compacted soil, representative of the compacted massif, were calibrated using laboratory tests conducted by Mello (2022). These tests includes oedometer and triaxial compression tests under conventional condition and with suction control. The calibration process for the mechanical parameters of the compacted soil followed a methodology consistent with that used for calibrating parameters for the red clay foundation soil. Figure 27 depicts the yield curves in (*p*,*q*) stress plane, while Figure 28 illustrates the LC curve, both for the compacted soil.

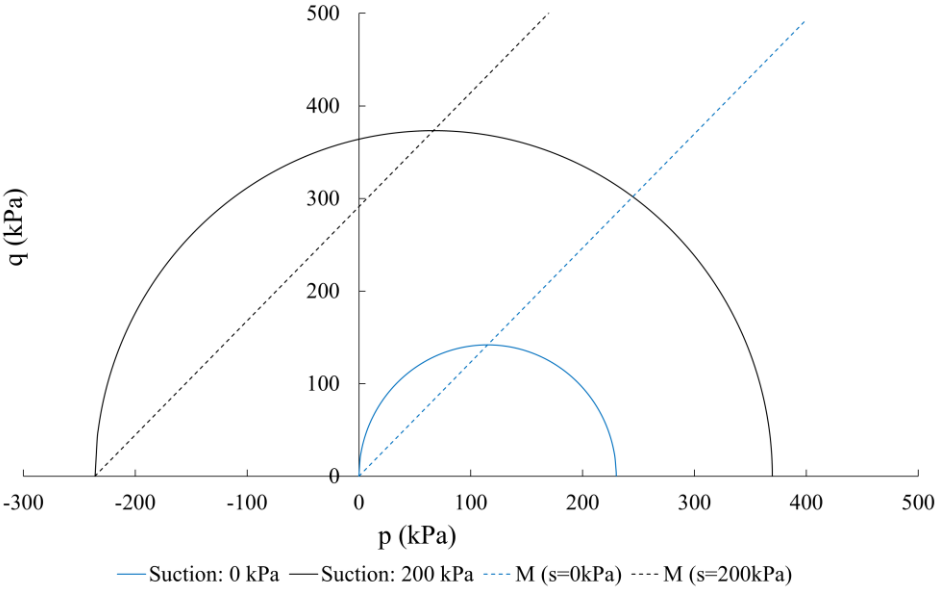

Figure 27. View of the yield curves in (*p*,*q*) stress plane for compacted soil

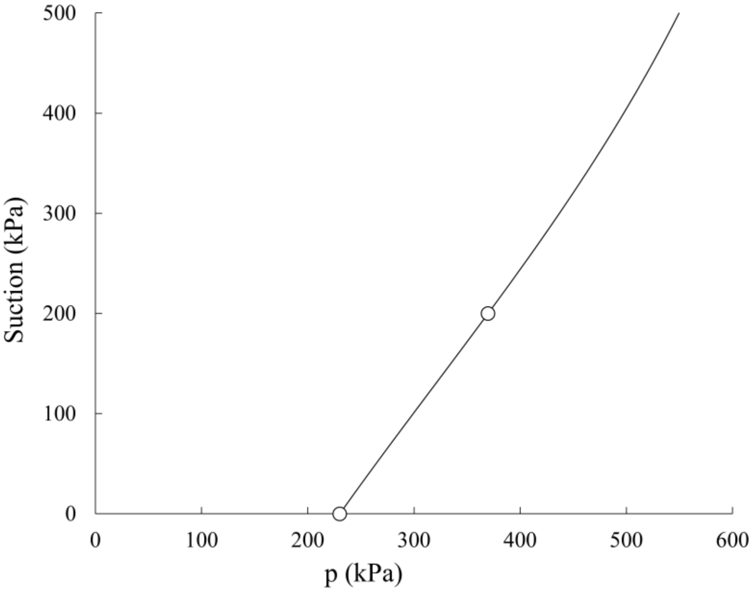

Figure 28. Loading-Collapse (LC) curve for compacted soil – (*p*,*s*) stress plane

Table 15 summarizes the mechanical constitutive parameters of the BBM for compacted soil.

Table 15. Mechanical constitutive parameter for compacted soil

	Mechanical Constitutive Parameters	Compacted Soil	Unit
κ	Elastic stiffness parameter for changes in net mean stress	0.006	-
$\lambda(0)$	Stiffness parameter for changes in net mean stress for virgin states of the soil (saturated soil)	0.120	-
$p0^*$	Isotropic pre-consolidation net stress for saturated condition	230.0	kPa
M	Slope of critical state line	1.23	-
k	Parameter describing the increase in cohesion with suction	1.180	-
r	Parameter defining the maximum soil stiffness	0.832	-
β	Parameter controlling the rate of increase of soil stiffness with suction	0.0030	kPa^{-1}
p_c	Reference stress	1	kPa
κ_{s0}	Initial (suction zero) elastic slope for specific volume-suction	8×10^{-3}	-
K_{min}	Minimum Bulk module	5.0	MPa
υ	Poisson's ratio	0.3	-
ρ_s	Solid phase density	2680	kg/m³

Numerical simulation of both the conventional oedometer test and the oedometer test with suction control allowed validating the selected mechanical parameters (Figure 29). This validation approach was previously employed for the natural foundation soil.

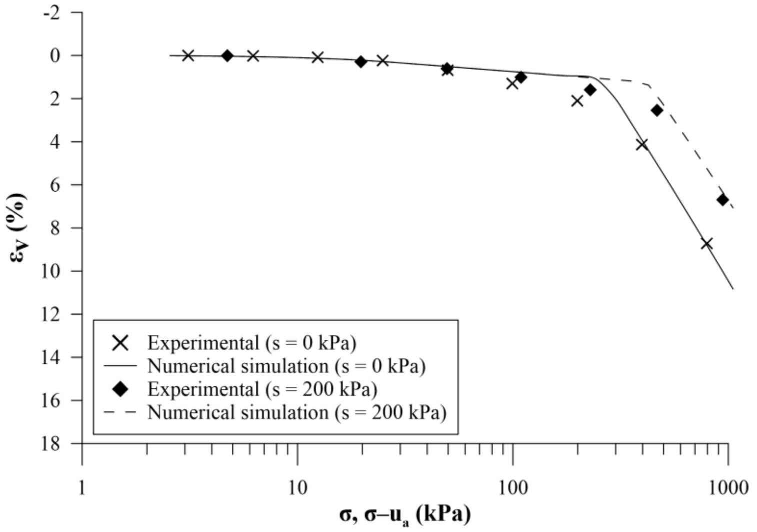

Figure 29. Numerical simulation of the oedometer test for compacted soil both saturated (s = 0 kPa) and with suction control (s = 200 kPa)

The SWRC of the compacted massif also displays bimodal behavior, leading to the adoption of a multimodal retention curve model (CASINI; VAUNAT; ROMERO, 2012). The intrinsic permeability value was determined through the flexible wall permeameter test under isotropic confining stresses of 0 kPa (MELLO, 2022).

Table 16 presents the hydraulic parameters of the compacted soil used in the numerical simulation. Figure 30 illustrates the numerical simulation alongside the SWRC experimental data points, employing the same methodology as that employed for the natural foundation soil.

Table 16. Hydraulic constitutive parameter for compacted soil

Hydraulic Constitutive Parameters		Compacted Soil	Unit
S_{ls}	Maximum saturation	1	-
S_{rl}	Residual saturation	0	-
w	Weight	0.620	-
M_{RC}	Shape coefficient of the macrostructural SWRC	0.127	-
P_M	Air Entry value of the macrostructural SWRC	0.01	MPa
m_{RC}	Shape coefficient of the microstructure SWRC	0.87	-
P_m	Air entry value of the microstructure SWRC	20.306	MPa
$(k_{11})_0$	Intrinsic Permeability	3.5×10^{-16}	m²
Φ_0	Reference porosity for read intrinsic permeability	0.435	-

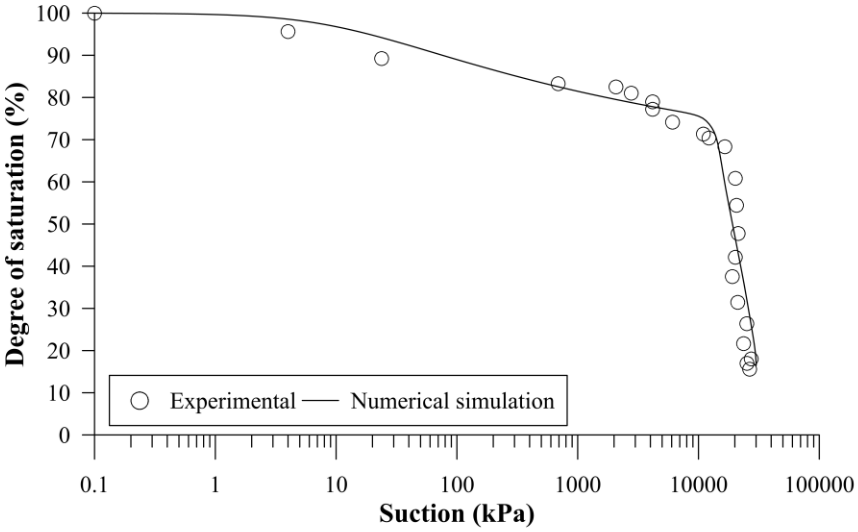

Figure 30. Numerical simulation of the SWRC for compacted soil

5.2.4 *Filters, Rip-Rap and Water*

The parameters for the filter and rip-rap materials were established based on information from historical documents detailing the construction of Itaipu's left bank earth dam. For simplicity and due to the lack of laboratory data, both materials were assumed to be within a linear elastic regime. In the absence of the necessary data for numerical simulation, parameter values consistent with the material type employed in the filter and rip-rap were adopted.

The construction of the filter used artificial sand from the crushing of basalt extracted during mandatory excavations, resulting in an average grain size composition of 47% gravel, 50% sand, and 3% silt. The filter exhibited an average porosity of 37%, with an average relative compaction reaching 90%. The average permeability for the filter was 8.0×10^{-3} m/s, as reported in Document 4280.50.8007-E-R0 (1992).

The rip-rap was composed of rock material obtained from the excavation of the deviation channel, and no specific laboratory tests were conducted on this material. Water was simulated as an independent material, characterized as highly porous and soft material.

The fitting model employed for the water retention curves of the filter materials, rip-rap, and water was the Van Genuchten model (1980). Table 17 and

Table *18* present the mechanical and hydraulic parameters, respectively, for the filter, rip-rap, and water materials. In the absence of specific data for these materials, the parameters were adopted based on their corresponding soil types. It should be noted that treating water as a material with the listed parameters was a numerical device to facilitate the simulation of the reservoir water level variations.

Table 17. Mechanical constitutive parameter for Filter, Rip-Rap and Water

		Filter and Rip-Rap	**Water**	**Unit**
E	Young Modulus	20	10	MPa
υ	Poisson's ratio	0.3	0.48	-
ρ	Solid phase density	2700 (default)	0.001	kg/m³

Table 18. Hydraulic constitutive parameter: Filter, Rip-Rap and water (REPORT 4280.50.8007-E-R0, 1992)

		Filter and Rip-Rap	**Water**	**Unit**
P_0	Measured P at certain temperature	0.01	0.001	MPa
λ	Shape function for retention curve	0.5	0.33	-
S_{ls}	Maximum saturation	1	1	-
S_{rl}	Residual Saturation	0	0	-
$(k_{11})_0$	Intrinsic Permeability	8×10^{-10}	1×10^{-10}	m²

5.3 Initial and Boundary Conditions

Solving the hydraulic and mechanical constitutive equations requires knowledge of the initial conditions and boundary conditions of the problem. Initial conditions are assigned to the surfaces, including the initial suction value and the initial porosity value.

The initial suction values (Figure 31) were determined from laboratory results, and historical documents (REPORT 4280.50.8007-E, 1992). The initial suction value for the water is set at 0.1 MPa, corresponding to atmospheric pressure (1 atm).

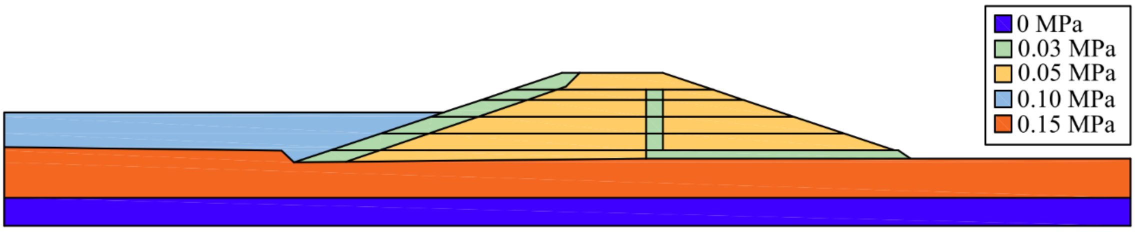

Figure 31. Initial conditions – Initial suction values for the material zoned

The construction project for the earth dam specified a water content deviation limit of ±2% from the optimum water content, with a minimum relative compaction (RC) set at 95%. Field control used the Hilf method. Analysis of all compaction tests revealed an overall average water content deviation of 0.38% below optimum water content, achieving an RC of 99.63% (REPORT 2061.50.1757.P, 1982).

Suction values were estimated from field data using the soil water retention curve for the compacted soil (MELLO, 2022). An adjusted value between the wetting and drying curves was considered for a water content of 27.4% (0.38% below the optimum water content) to account for hysteresis effect. The adopted suction value for the compacted soil in the numerical simulation was 50 kPa (Figure 32).

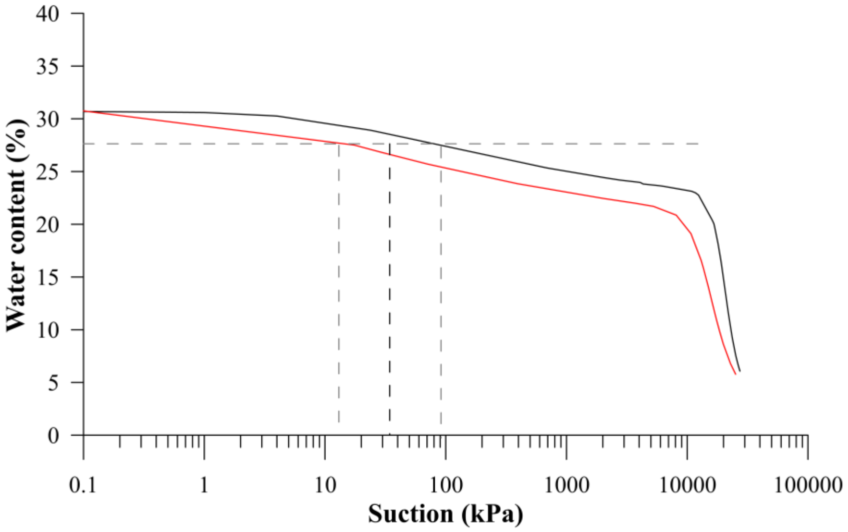

Figure 32. Definition of the initial suction value for the compacted soil using the SWRC

The reported average natural water content of the foundation clay is 28% (REPORT 4280.50.8007-E, 1992). Additionally, all borings conducted confirmed that the water level table consistently remained below the red clay layer before construction (REPORT 2080.54.15717-P, 1977). The initial suction for the foundation clay was determined following the same methodology as for the compacted soil, using the SWRC and incorporating both wetting and drying paths (MELLO, 2022), as depicted in Figure 33. The adopted initial suction value for the foundation clay was set at 150 kPa, distributed linearly. The saprolite beneath the foundation clay was assumed to be saturated.

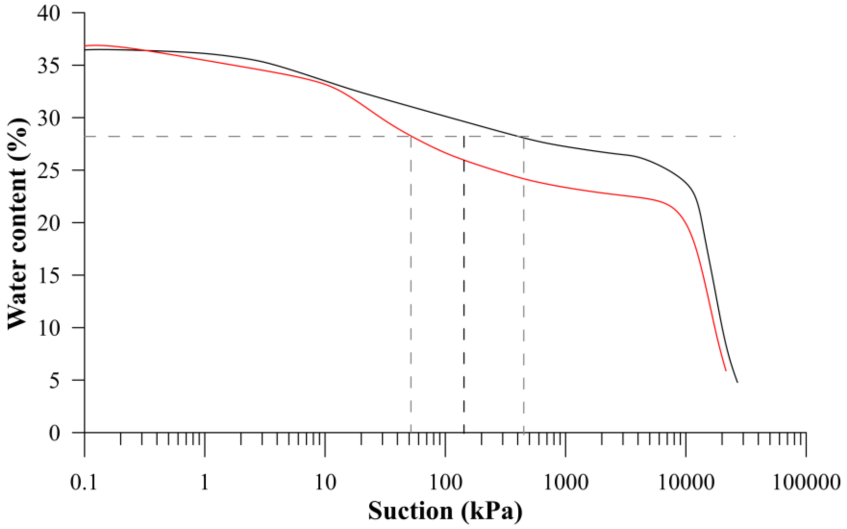

Figure 33. Definition of the initial suction value for the foundation soil using the SWRC

Laboratory tests conducted by Mello (2022) and historical reports related to the dam established the initial porosity of all materials. Figure 34 illustrates the porosity values for the zoned materials.

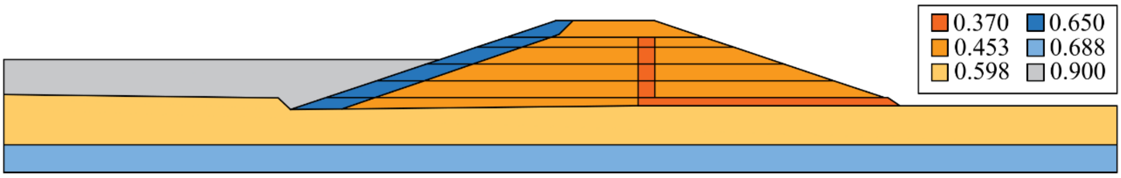

Figure 34. Initial conditions - Porosity values for the material zoned

The simulation of the Itaipu dam, treated as a coupled hydro-mechanical problem, required defining a set of mechanical and hydraulic boundary conditions, both applied as line conditions. Mechanical boundary conditions involve displacement restrictions. Specifically, a displacement constraint applied in the X and Y directions at the bottom boundary of the foundation, and in the X direction at the side boundaries.

Regarding the hydraulic boundary conditions, the base of the model geometry, corresponding to the saprolite foundation, was assumed to be impermeable. A seepage condition was applied to the downstream face of the dam to allow water to flow out. Additionally, variations in the water level were controlled by applying a hydraulic boundary condition at the top of the water layer. The constant "Gamma for liquid" allows specifying pressure with more or less strength. Negative values of this constant indicate that nodes with this type of boundary condition permit seepage, i.e., only allowing flow out. When the constant assumes a zero value, the nodes are impermeable.

Figure 35 visually illustrates the hydraulic and mechanical boundary conditions imposed on the problem.

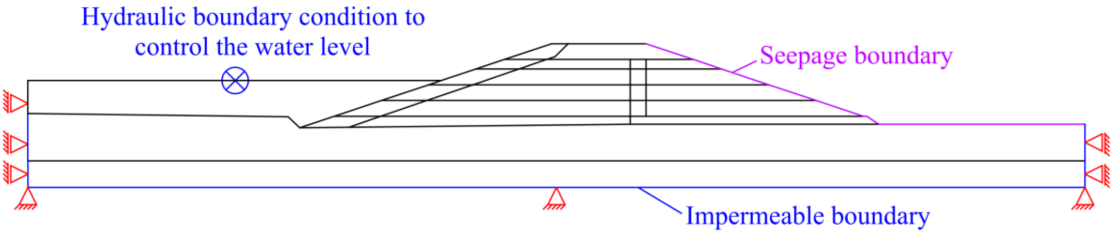

Figure 35. Hydraulic and mechanical boundary conditions

5.4 Time Interval

5.4.1 Construction and impoundment

The simulation of the construction and impoundment followed the Itaipu Dam construction memorial records, the reservoir water level records, and the piezometric level measurements of PS-L-23, located at the station of interest.

Construction of the second section (with a height of less than 10 meters), from station 128+80.00 to station 142+36.50, began in October 1980 and work on the compacted massif was completed in June 1982. Station 135+50, the focus of this research, was constructed between January and May 1981 (REPORT 4280.50.8006, 1991). The filling of the reservoir began in May 1984.

The construction of the Itaipu dam was simulated by systematically adding layers to the initial foundation geometry, as shown in Figure 22. The CODE_BRIGHT program simulates the gradual construction of these layers at each specified interval date. In CODE_BRIGHT, the time intervals control the construction stages and the application of boundary conditions, such as hydraulic boundary condition to simulate the reservoir impoundment. The simulation of the construction of the Earth dam at station 135+50 is illustrated in Figure 36.

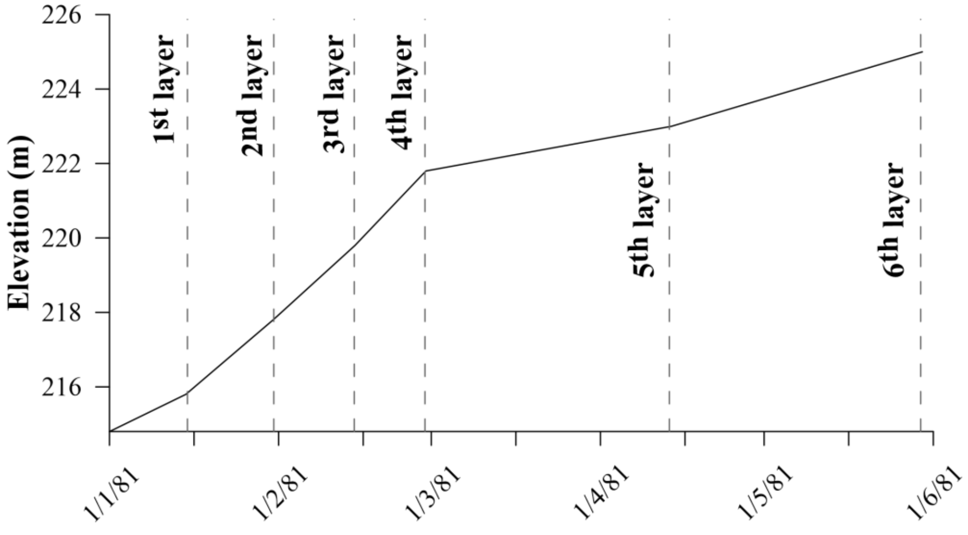

Figure 36. Simulation of the gradual construction of the compacted massif layers

Figure 37 illustrates the intervals to simulate the construction and impoundment at the station 135+50. The first six intervals correspond to the systematic construction of the compacted layers. The reservoir impoundment was carried out in three phases: the first took place in October 1982, reaching an elevation of 205.6 m; the second occurred between October 1982 and April 1984, reaching 217 m; and finally, the third phase was completed between April and May 1984, reaching the normal operating level of 219.4 m. This third phase of the reservoir impoundment occurred approximately thirty-six months after the construction of this section was completed (IECO-ECL, 1995). During this period, piezometric measurements recorded at PS-L-23 showed fluctuations in the water level within the dam foundation prior to the initial reservoir filling. The numerical simulation of the reservoir impoundment considered in this study begins from the third phase.

The piezometric head measurements from PS-L-23 (Figure 15) were used as a reference for setting the water level in the foundation layer during construction and before the third phase of the reservoir's filling and operation, between April 1981 and May 1984 (interval 7 to 16). From May 1984 onwards (from interval 17), reservoir level records were used to simulate the dam's third phase of impoundment and the initial months of operation.

The simulation of the water level in the foundation between April 1981 and May 1984 was conducted by imposing hydraulic boundary conditions, specifically prescribed liquid pressure and incremental liquid pressure, on the upper boundary of the "Red Clay Foundation" material downstream of the dam. Similarly, the simulation of the reservoir filling and the initial months of dam operation involved applying hydraulic boundary conditions on the upper boundary of the "Water" material, following the activation of this layer.

Figure 37 illustrates the construction and reservoir impoundment stages. The initial intervals (1 to 6) represent the systematic construction of the compacted layers. Between April 1981 and May 1984, during intervals 6 to 16, the water level in the clay foundation was simulated using piezometer readings as a reference. This procedure was adopted because even partial saturation of the foundation layer after construction can lead to saturation-induced deformation. Finally, from May 1984 onwards, the hydraulic boundary condition was imposed based on measurements of the reservoir's water level.

The reservoir's water level measurements defined the boundary condition for each time interval during the filling stage and the initial months of operation. This was the only boundary condition that varied with each interval.

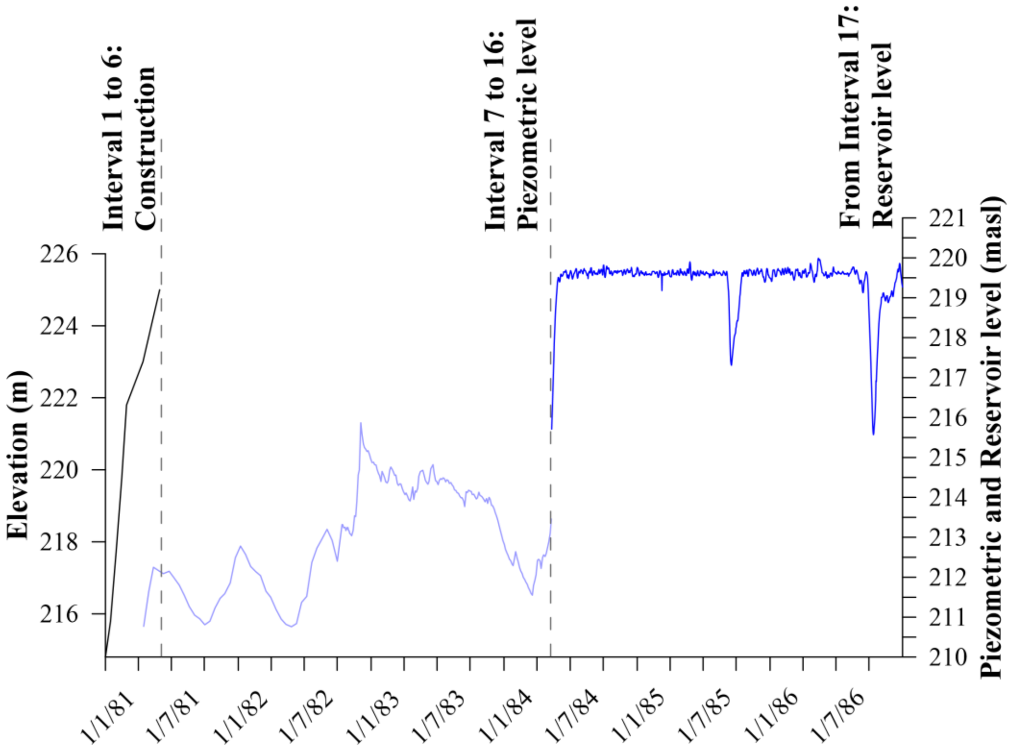

Figure 37. Interval data: Construction and reservoir impoundment

5.4.2 ***Operation***

The numerical simulation of the operation encompasses the entire history of the Itaipu earth dam, from construction, impoundment, and reservoir water level variations up to the year 2016. The initial stages of simulation up to reservoir filling were maintained as previously described (section 5.4.1). The numerical simulation of dam operation applied a hydraulic boundary condition of liquid pressure at the top of the water domain to represent the daily variation of reservoir level over the years. This boundary condition was the only one that varied within the imposed time intervals, and it was automatically inserted using a computer code to handle the calculation files generated during the pre-processing stage.

The simulation time representing the construction, impoundment, and operation stages of the dam were as follows:

Table 19. Simulation time: Construction, impoundment, and operation

Stage	**Description**	**Height (m)**	t_0 **(days)**	t_f **(days)**
A	Construction to elevation 215.8m	1.0	0	14
B	Construction to elevation 217.8m	3.0	14	30
C	Construction to elevation 219.8m	5.0	30	45
D	Construction to elevation 221.8m	7.0	45	58
E	Construction to elevation 223.0m	8.2	58	103
F	Construction to elevation 225.0m (10.2 meters high, completion of construction); and positioning the water table in the foundation layer with piezometer level data.	10.2	103	149
G	Positioning the water level in the foundation layer with piezometer level data	10.2	149	1226
H	Impounding of the reservoir to elevation 219.15m, using the reservoir data	10.2	1226	1260
I	Operation spanning 1984 to 2017, using the reservoir data	10.2	1260	13207

5.5 Mesh

The finite element mesh used in the numerical simulation consists of 3-node linear triangular elements, with 1476 nodes and 2702 elements (Figure 38). The mesh is sufficiently dense to achieve good accuracy. Additional tests with both finer and coarser meshes were performed, confirming that the selected discretization provides reliable results while maintaining computational efficiency. For the coupled hydro-mechanical problem, each node has three degrees of freedom: water pressure, horizontal displacement, and vertical displacement.

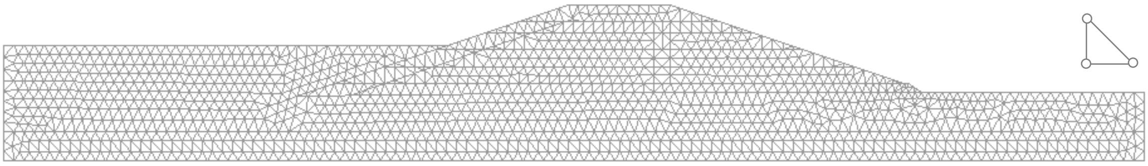

Figure 38. Finite element mesh of left bank earth dam of Itaipu

Figure 39 illustrates the mesh quality criterion based on shape quality. This criterion assess the similarity of the element to the reference shape. In this case, the triangular element is compared to an equilateral triangle. A value of one indicates a perfect element (i.e., an equilateral triangle), and this value decreases as the element deviates from the reference shape.

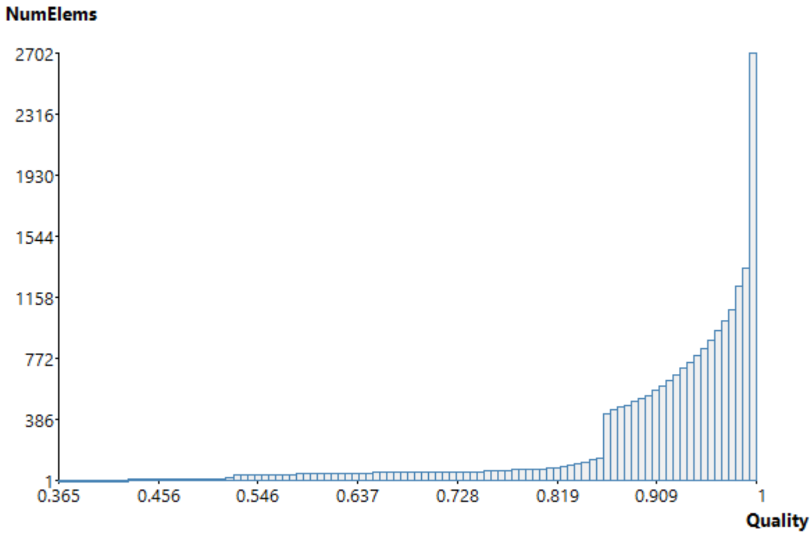

Figure 39. Mesh quality - Shape quality cumulative distribution

6 RESULTS AND DISCUSSIONS: ORIGINAL BBM

In this section, the results of the numerical simulation of the construction, reservoir impoundment, and operation of the earth dam are presented, employing the Barcelona Basic Model (BBM) originally implemented in CODE_BRIGHT.

Results from the coupled hydro-mechanical numerical simulation were compared with field instrumentation data. Station 135+50 is equipped with two standpipe piezometer (PS-L-23 and PS-L-24), two settlement gauges (MA-L-8) and one survey marker (MR-L-23) located nearby. Section 4.4 gathers the instrumentation data and information, while Figure 40 illustrates the installation locations of these instruments in the field. These instruments were used in analyzing the simulation results for both the construction and impoundment phases, as well as during the operational phase of the dam.

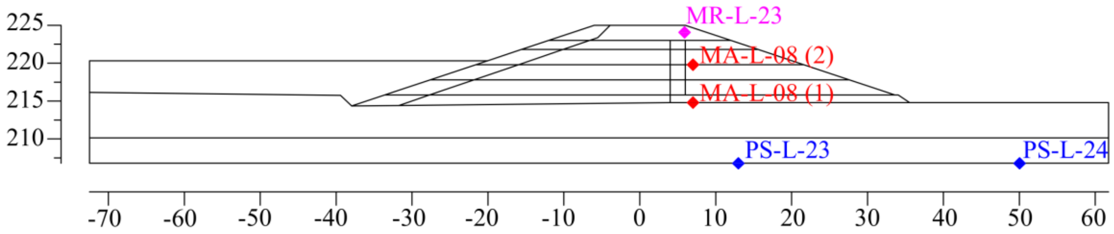

Figure 40. Summary of instruments at station 135+50 used in analysis of simulation results

6.1 Construction and Impoundment

The construction of the station 135+50 occurred between January and May 1981. The filling of the reservoir and the start of operation began in May 1984. During this 36-month period, preliminary reservoir filling stages took place, with water level variations in the foundation layer. These variations were simulated using data from piezometer PS-L-23. The filling and initial operations were simulated using reservoir level data (in masl). Figure 37 (topic 5.4.1) visually captures the construction and impoundment stages, whose numerical simulation corresponds to stages [A] to [H].

Figure 41 shows the simulation of the reservoir level during construction, impoundment, and the initial years of operation. Positioning the water level was done in a simplified way until filling and operation began in 1984. The reservoir water lever was simulated using daily field data during the dam operation.

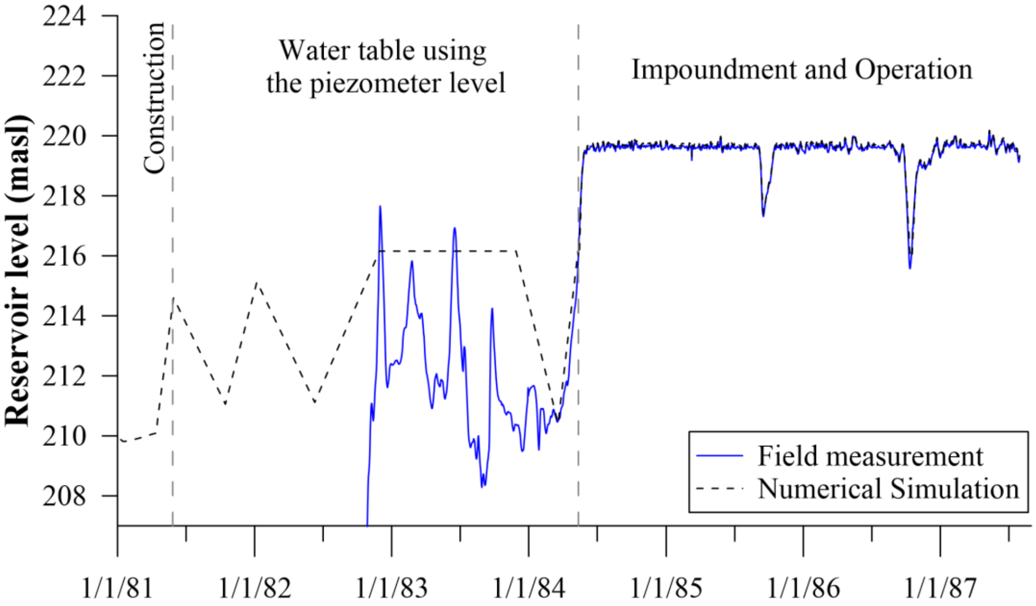

Figure 41. Reservoir levels (in masl) during construction, impoundment and initial years of operation: field measurement and numerical simulation

Figure 42 and Figure 43 show the comparison between the field readings of the PS-L-23 e PS-L-24 piezometers and the numerical simulation, respectively. The simulated piezometer levels from stage [A] to [H] align well with the field data for both piezometer data, even during the simplified variation of water table period before initial reservoir filling.

The vertical stress field was analyzed at the end of stage [F], at 149 days of simulation. This stage marks the construction completion of the last layer of the earth dam and the beginning of the variation in the water level positioning in the foundation.

The stress field was developed by measuring the stresses along horizontal lines positioned in the middle of each simulated layer: saprolite, red clay foundation, and the six compacted layers of the earth dam. Figure 44 illustrates the stress field, where the zero horizontal distance represents the axis of the earth dam. The increase in stress due to the weight of the earth dam, calculated during the design stage, was approximately 190 kPa according to historical reports (REPORT 4280.50.8007-E-R0, 1992). This value, adopted in the design, aligns with the vertical stress value obtained in the numerical simulation of the dam construction.

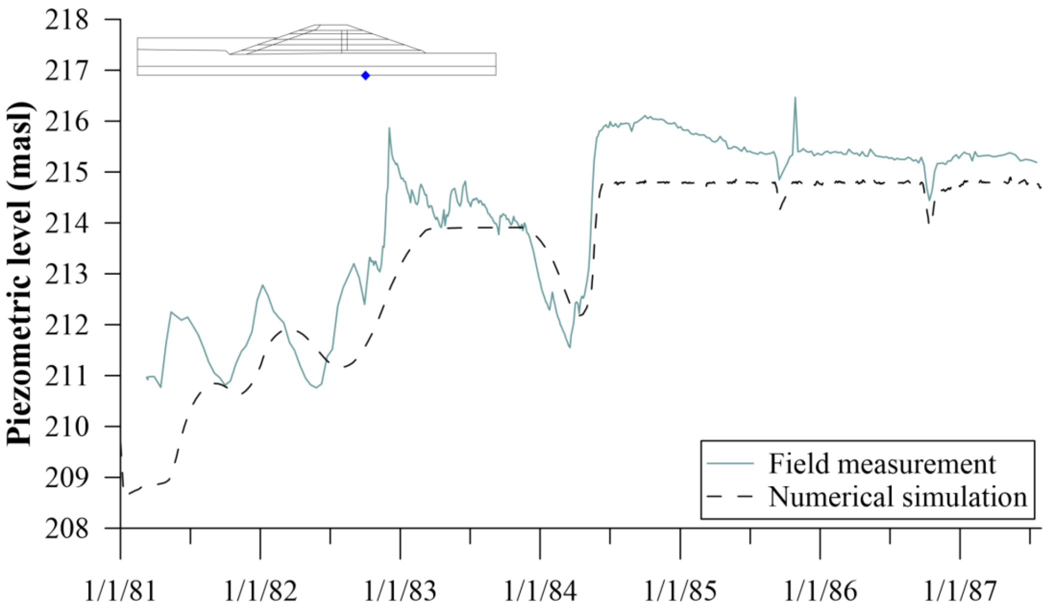

Figure 42. PS-L-23 - Piezometric levels (in masl) during construction, impoundment and initial years of operation: field measurement and numerical simulation

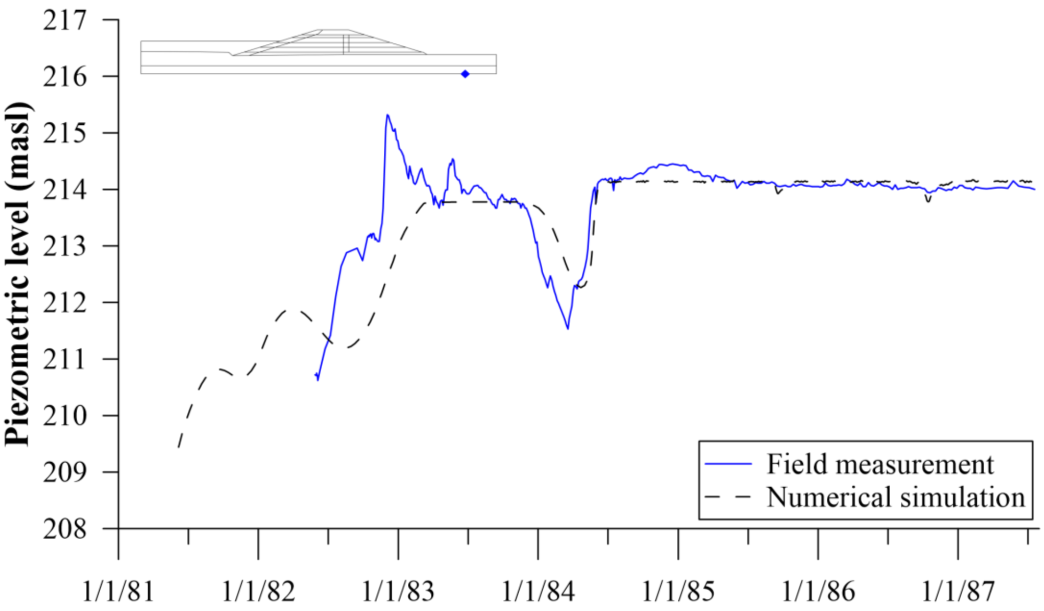

Figure 43. PS-L-24 - Piezometric levels (in masl) during construction, impoundment and initial years of operation: field measurement and numerical simulation

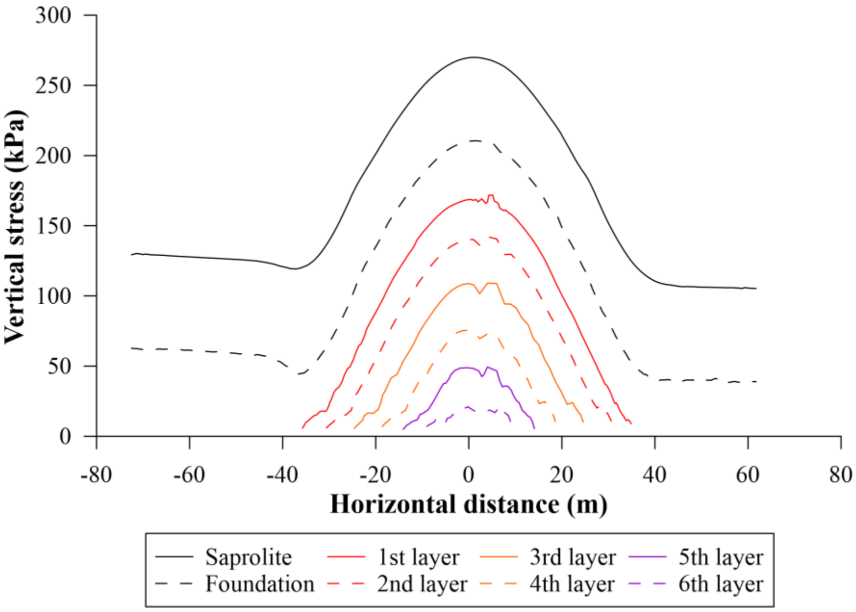

Figure 44. Stress field after construction – End of stage [F]

Simulated settlements during the construction and reservoir filling were compared with field data from two settlement gauges located at station 135+50 (Figure 45). The settlements that occurred between the end of construction, the impoundment and the operation were captured in the numerical simulation by varying the foundation water level based on the piezometric levels readings. The results obtained from the simulation showed a good fit with the field data.

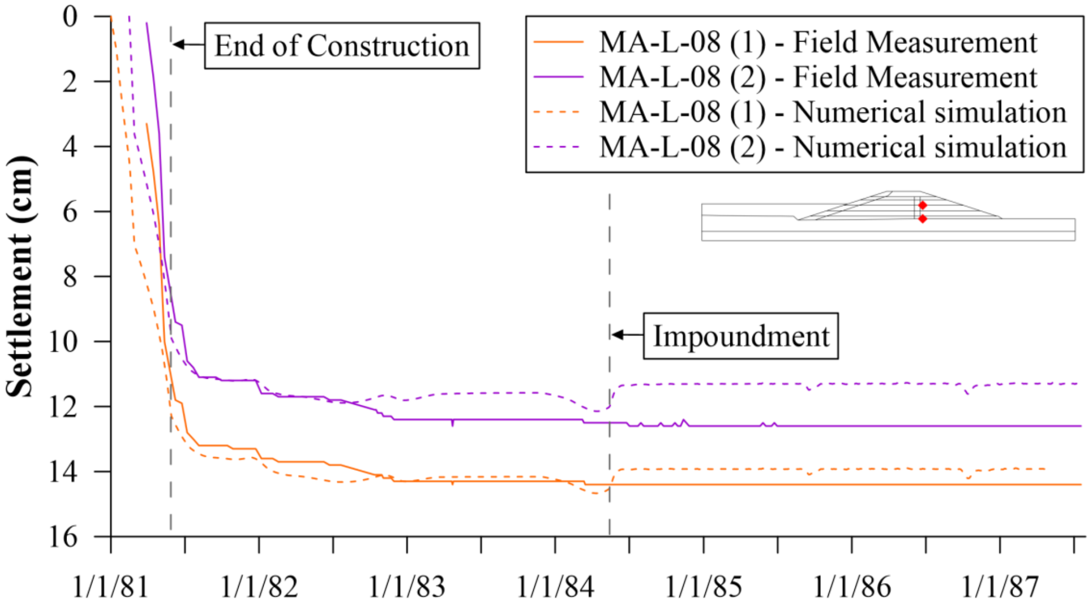

Figure 45. MA-L-08 - Settlement during construction, impoundment and initial years of operation: field measurement and numerical simulation

Figure 46 and Figure 47 illustrate selected post-processing results from the numerical simulation. In Figure 46, positive pore water pressure is shown, representing the position of the phreatic surface at different stages of the simulation: at the end of construction (a), at the end of reservoir impounding (b), and during the initial years of operation (c). The results highlight the progressive development of the phreatic surface over time, reflecting the effects of construction and operational conditions. The observed position of the phreatic surface during the operational period is consistent with field measurements, confirming the consistency of the simulation.

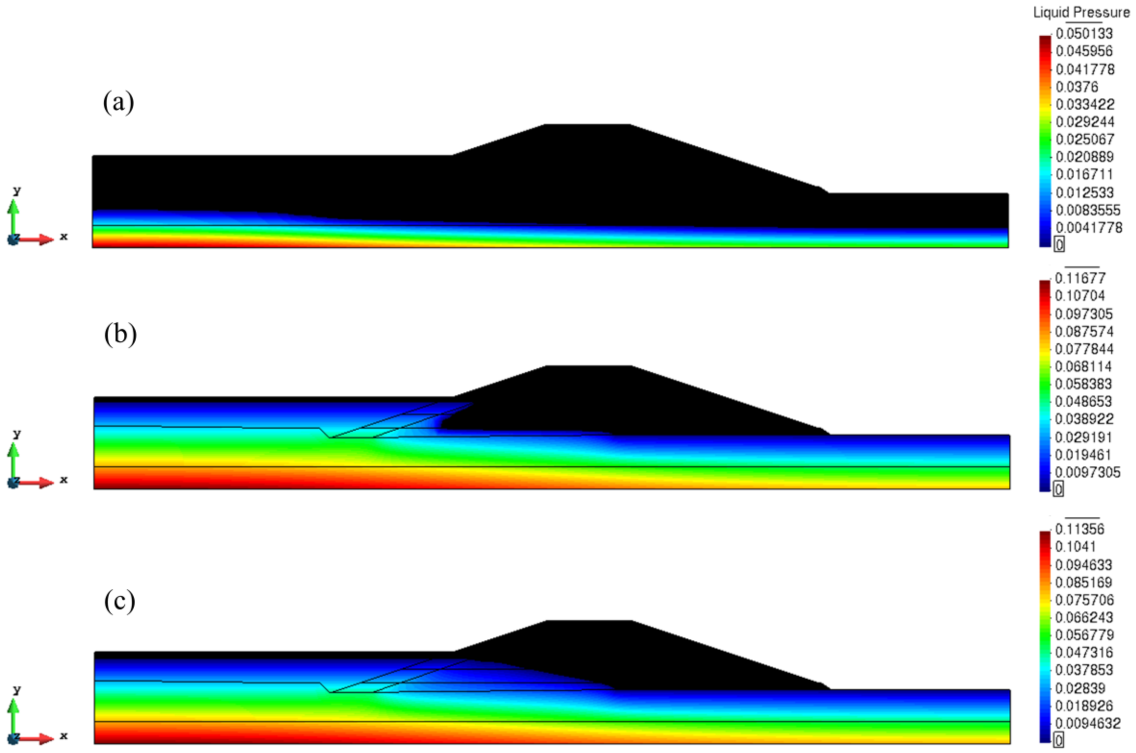

Figure 46. Evolution of pore water pressure for positive values, indicating the position of the phreatic surface: (a) 149 days (end of construction, June 1981, stage [F]); (b) 1260 days (end of reservoir impounding, June 1984, stage [H]); (c) 2402 days (initial years of operation, July 1987)

Figure 47 shows the stress and vertical strain vectors at 2402 days of the numerical simulation, corresponding to the initial years of operation. This representation highlights the layers experiencing the highest concentrations of stress and strain after the construction and reservoir impounding stages.

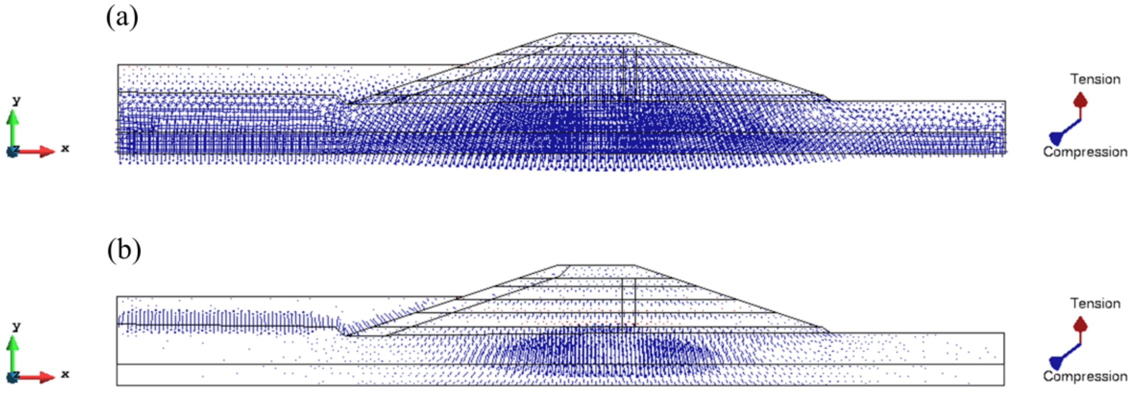

Figure 47 (a). Stress vector (Scale Factor: 20) and (b) Vertical strain vector (Scale Factor: 150), both corresponding to 2402 days (initial years of operation, July 1987)

Numerical simulation of the dam's construction and impoundment history allows for a more detailed evaluation of the flow and deformation behaviors observed in the field. By validating the numerical simulation results with field instrumentation data, including piezometers and settlement gauges, it becomes possible to assess the behavior of the dam considering the stress states consistent with the transient conditions that occur in earth dams during the construction, impoundment and operation phases. One of the main advantages of this modelling approach is the consistent coupling between water transfer and deformation mechanisms.

Loading or collapse paths can shift the yield, resulting in irreversible volumetric strain. Figure 48 shows the evolution of the historical variable p_0^* (isotropic yield stress for saturated conditions) over different periods of the analysis. The time at zero days corresponds to the initial condition, 149 days marks the end of construction (June 1981, stage [F]), and 1260 days represents the end of reservoir impounding (June 1984, stage [H]). The variation profiles of the historical variable p_0^* were measured along the dam's axis.

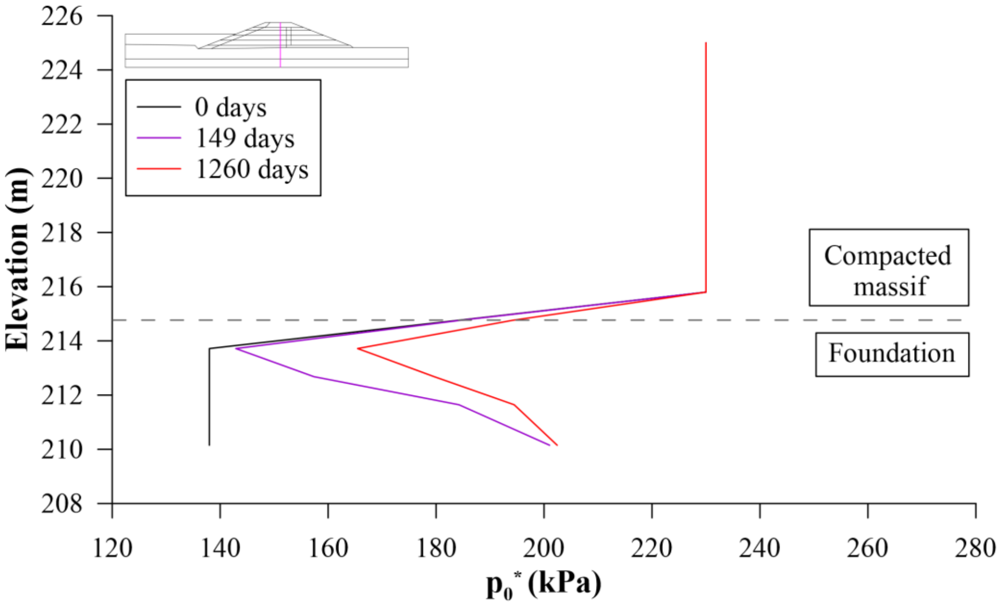

Figure 48. Evolution of the historical variable p₀* during the construction and impoundment of the earth dam

The evolution of the historical variable p_0^* indicates that yielding, i.e., irreversible volumetric strain, occurred only in the red clay foundation layer during the construction of the dam and impoundment periods. At the end of the construction phase, after 149 days of simulation, there was a significant increase in p_0^* because of the loading path. Following the end of the compacted massif and reservoir filling, the yield curve in the foundation layer continued to expand, with the evolution of p0*driven by a wetting path, even in the absence of additional applied loads. Figure 48 captures this trend, showing an increase in p_0^* within the foundation for both loading and wetting paths throughout the construction and impoundment stages. This behavior shows the evolution of the yield curve in response to changes in suctions conditions.

This finding is particularly relevant because it suggests that irreversible volumetric strains occurred only in the red clay foundation layer, while the compacted dam body remained within the elastic range throughout the construction and impoundment periods. Such behavior suggests an adequate construction quality and compaction of the embankment, as the permanent deformations occurred only where expected, in the foundation layer, due to loading and subsequent wetting. Overall, this result supports the interpretation that the dam exhibited a stable and well-controlled geomechanical response during these stages.

The accumulated plastic strain and the increase in the elastic region of the soil are visualized by the displacement of the LC curve due to the stress path occurring in the problem. The displacement of the LC curve and the consequent irreversible strains can occur due to loading or collapse paths. In the case of the construction and reservoir filling of the Itaipu earth dam, both paths led to the shift of the yield locus of the soil foundation.

Upon observing the evolution of strain and liquid pressure at a point in the red clay foundation layer, specifically in the lower portion where the accumulation of plastic deformations is greater, the strains continued to occur after construction was completed due to the rise in the water level in the foundation (Figure 49). After the development of strains caused by the increased stress from the earth dam, following a loading path, there was a slight increase in plastic strains due to the wetting and reduction of suction in this layer, indicating a collapse path, as shown in Figure 47 by the wetting-induced plastic strain, which reached approximately 0.5%.

In geotechnical engineering, soil collapse is typically associated with issues resulting from large deformations, above 2%, due to the wetting of soil under constant stress. In the case of the Itaipu earth dam, the wetting-induced plastic strain that occurred in the foundation layer after construction was fairly small and did not cause any significant geotechnical issues. Identifying this phenomenon in numerical simulations, even when it is of small magnitude, is crucial for a deeper understanding of soil behavior and the coupling between hydraulic and mechanical processes.

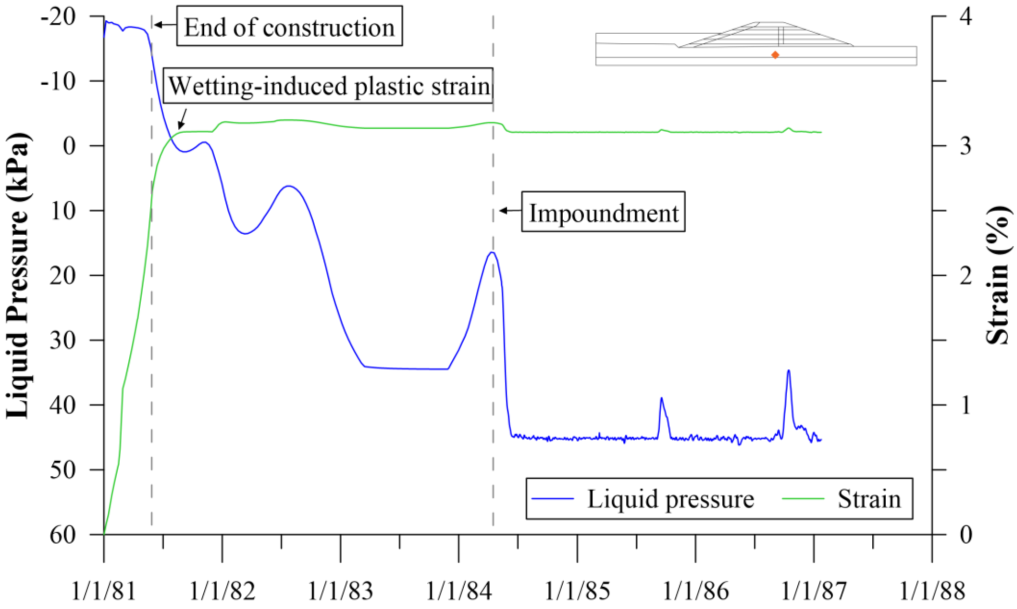

Figure 49. Comparison of liquid pressure and strain in the foundation layer during the construction and reservoir filling phases of the dam

6.2 Operation

The numerical simulation of the Itaipu earth dam's operation was conducted considering daily measurements of the reservoir water level from its filling in 1984 to June 2016, totaling approximately 32 years of operation. The initial stages of construction and reservoir filling were included in the numerical simulation, with the reservoir level variation simulated by imposing hydraulic boundary conditions of liquid pressure at the top of the "water" material.

Figure 50 illustrates the simulated reservoir level compared to field data over the years of operation. As with the construction and impoundment stages, the numerical simulation results were validated and compared with data from field-installed instruments. Figure 51 and Figure 52 show the comparison between the field readings of the PS-L-23 e PS-L-24 piezometers and the numerical simulation, respectively. The simulation results had a good fit with the field data recorded by the piezometers.

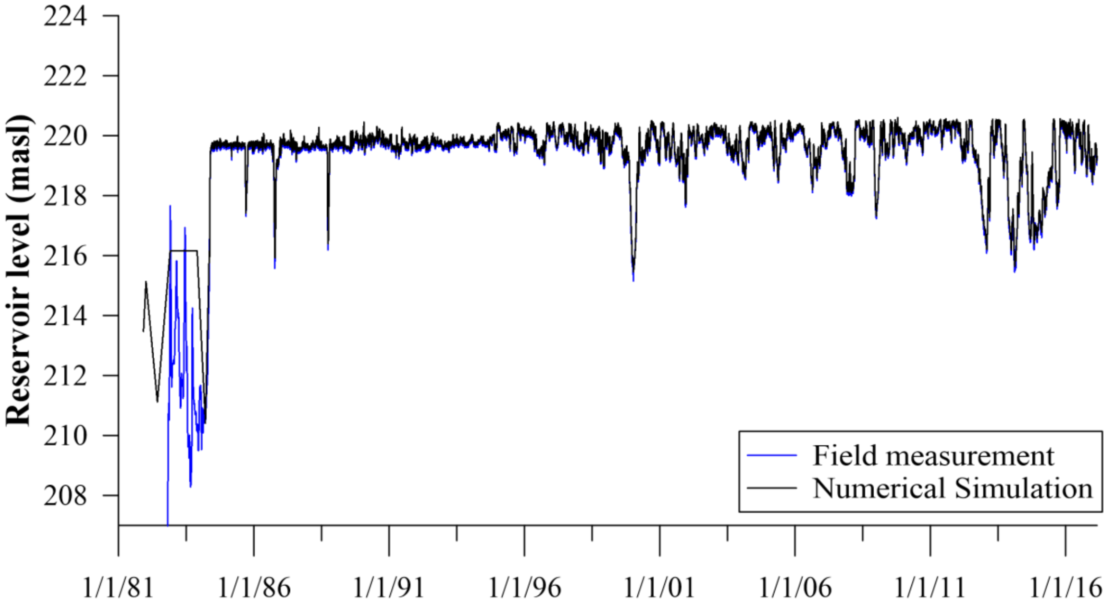

Figure 50. Reservoir levels (in masl) during operation: field measurement and numerical simulation

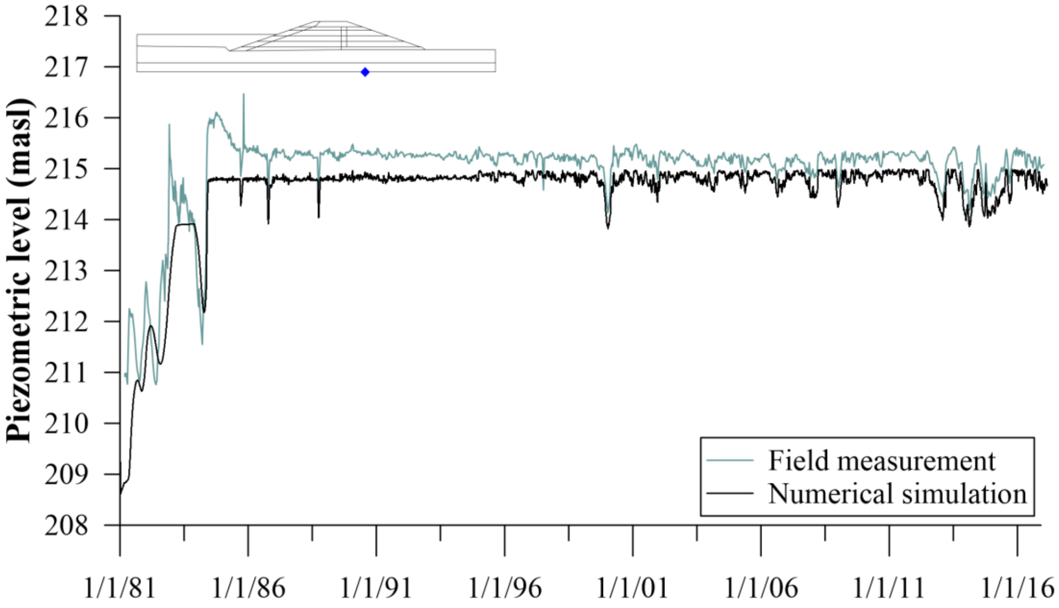

Figure 51. PS-L-23 - Piezometric levels (in masl) during operation: field measurement and numerical simulation

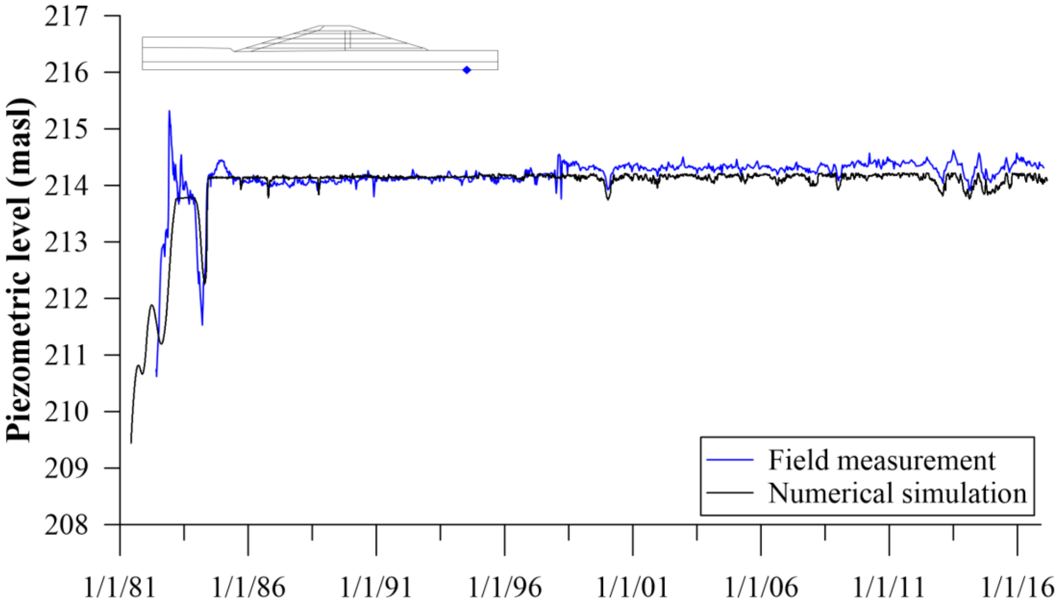

Figure 52. PS-L-24 - Piezometric levels (in masl) during operation: field measurement and numerical simulation

Figure 53 shows the comparison between the numerical simulation and the field settlement records from two settlement gauges located at station 135+50, covering the entire period of operation. Settlement readings were taken twice a year until 2006, at which point they were halted as the settlements were considered stabilized. Sporadic settlement readings resumed from 2014 onwards. The numerical simulation showed good agreement with the field results up to 2006, confirming the stabilization of settlements. However, after readings resumed, settlements of approximately 2 centimeters recorded in the field were not captured by the numerical simulation.

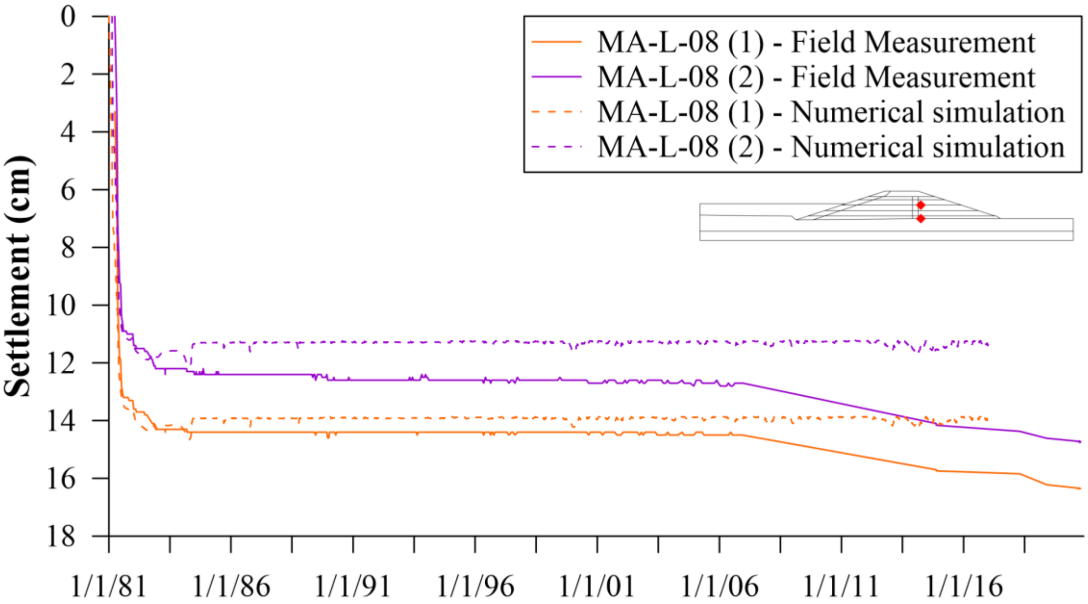

Figure 53. MA-L-08 - Settlement during operation: field measurement and numerical simulation

The objective of numerically simulating the operation of the earth dam, in addition to capturing the entire history since its construction, is to analyze the settlements recorded by the reference marker MR-L-23 installed on the crest, near station 135+50. As described in item 4.5, the hypothesis is that the settlements observed during the dam's operation occurred due to prolonged periods when the reservoir water level was below the normal operating levels, causing plastic settlements due to soil drying processes.

Figure 54 illustrates the numerical simulation results compared to the field data. The numerical simulation did not capture the plastic settlements recorded by MR-L-23, which were approximately 2.5 centimeters between 1999 and 2000, followed by stabilization, and a crest settlement of around 3 centimeters between 2012 and 2015.

The inability of the numerical simulation to capture the settlements was expected, as the yield SI (suction increase) curve, which defines the elastic boundary for suction increments due to drying, is formulated but not implemented in the CODE_BRIGHT program. Further details on the implementation of the SI (suction increase) curve, along with the numerical simulation of the Itapu dam results, are discussed in the following sections.

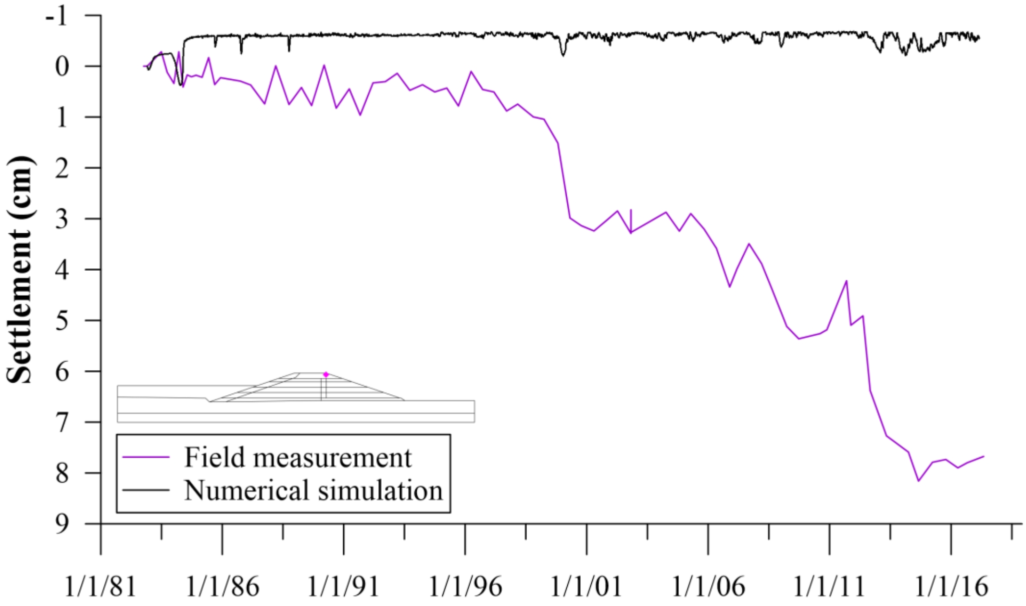

Figure 54. MR-L-23 -Crest settlement during operation: field measurement and numerical simulation

7 SUCTION-INCREASE CURVE IMPLEMENTATION

The finite element program CODE_BRIGHT, described in Section 3 (Item 3.2.3), includes different available mechanical constitutive models, such as the viscoplastic model for saturated and unsaturated soils and rocks, the thermo-elastoplastic model for unsaturated soils (TEP), the Barcelona Expansive Model (BExM), and the argillite model. However, none of these models officially incorporates the SI curve in the current implementation of CODE_BRIGHT. In this study, the TEP model was selected to simulate the mechanical behavior of the Itaipu earth dam, and the SI curve was therefore newly implemented within this framework.

This section introduces the computational approach adopted for stress integration in soils, with emphasis on the elastoplastic "stress-update" method as implemented in CODE_BRIGHT. The presentation is organized in two parts: first, the original formulation of the BBM within the TEP framework is described; then, the modifications introduced to incorporate the SI curve are detailed.

7.1. Thermo-Elastoplastic Model for Soils (TEP Model)

Soils typically exhibit non-linear stress–strain behavior, which must be described using incremental or rate-based constitutive formulations. Solving these equations involves integrating a differential algebraic system, commonly referred as "stress-update" procedure. In the context of the Finite Element Method (FEM), applied to initial and boundary value problems, these constitutive relations are integrated based on prescribed strain increments or strain rates.

Plasticity theory provides the framework for solving such non-linear problems through numerical integration. It relies on fundamental concepts such as the additive decomposition of strains, yield criteria, plastic potentials, and loading/unloading conditions. Within this framework, small total deformations are decomposed into independent elastic and plastic components to derive the elastoplastic constitutive equations. The flow rule governs the evolution of plastic strains, with their directions being defined by the plastic potential.

Integration of constitutive relations to obtain the stress increments is a key step in non-linear FEM analysis. Both implicit and explicit schemes are available for this purpose. In a fully implicit scheme, gradients and the hardening law are evaluated at the unknown (or future) stress state, requiring Newton-Raphson iterative scheme for solving the non-linear equations. Although more complex to implement, this approach has the advantage of automatically satisfying the yield condition when the stress state evolves from the elastic to the plastic regime.

Explicit integration schemes, in contrast, evaluate the yield surface, plastic potential gradients, and hardening law at known stress states. No integration is required to predict the final stress, apart from iterations to correct and restore consistency with the yield surface and hardening law. Explicit integration is simpler to implement and can be enhanced through substepping and error control strategies to improve elastoplastic predictions (SLOAN, 1987; SLOAN; ABBO; SHENG, 2001).

In CODE_BRIGHT, the choice between implicit and explicit integration depends on the selected constitutive model. The Thermo-Elastoplastic (TEP) model for soils, used in this research, employs an explicit integration scheme with error control proposed by Sloan (1987).

In elastoplastic FEM analysis, external forces are applied incrementally, and the corresponding nodal displacements are obtained by solving the global stiffness equations. Strain increments are then computed at discrete integration points within each element using strain–displacement relations, and the stress state is updated through stress–strain relations based on the Generalized Hooke’s Law. Typically, integration algorithms start from a trial elastic stress, obtained by applying a strain increment to check whether the stress state remains within the elastic domain or lies on the yield surface boundary. Based on this, elastic or plastic integration is performed.

If the applied strain increment induces elastic or plastic yielding, the governing system of differential equations generally takes the form:

$$d\boldsymbol{\varepsilon} = \mathbf{C} : d\boldsymbol{\sigma} \tag{19}$$

where **C** é the fourth-order elastic or elastoplastic stress-strain tensor, depending on whether the imposed strain increment induces elastic or plastic yielding, respectively.

The TEP model is structured into five computational routines, detailed in the following: trial elastic stress, elastic integration, plastic integration, yield surface crossing algorithm, and yield correction algorithm. For clarity, all variables are expressed in this work in terms of finite increments, denoted by *d*, rather than in rate form as is commonly presented in constitutive formulations.

7.1.1 ***Trial Elastic Stress***

Sloan's (1987) substepping algorithm integrates the constitutive law by dividing the strain increment into multiple small substeps and computing the stress-strain response at each one. The integration procedure begins with an initial elastic trial stress, in which the strain increment is divided into 100 to check whether the stress state reaches the yield surface boundary. This approach identifies even if a small strain increment may induce plastic yielding. The initial trial elastic strain increment is defined as:

$$d\boldsymbol{\varepsilon}_{tr} = \frac{d\boldsymbol{\varepsilon}}{100} \tag{20}$$

where $d\boldsymbol{\varepsilon}$ is the total strain increment, being an external subroutine variable.

The same procedure is applied to suction and temperature increments. For instance, the total suction or temperature increment is also subdivided into 100 parts for the initial trial step. For simplicity, temperature and suction increments are omitted.

The elastic constitutive matrix is calculated based on the stress from the previous step $(\boldsymbol{\sigma}^{old})$, using the bulk (*K*) and shear (*G*) moduli. Since the integration scheme is explicit, a known stress state is used. The elastic constitutive matrix is given by Equation 21.

$$\mathbf{C}_e = \begin{bmatrix} K+\frac{4G}{3} & K-\frac{2G}{3} & K-\frac{2G}{3} & 0 & 0 & 0 \\ K-\frac{2G}{3} & K+\frac{4G}{3} & K-\frac{2G}{3} & 0 & 0 & 0 \\ K-\frac{2G}{3} & K-\frac{2G}{3} & K+\frac{4G}{3} & 0 & 0 & 0 \\ 0 & 0 & 0 & G & 0 & 0 \\ 0 & 0 & 0 & 0 & G & 0 \\ 0 & 0 & 0 & 0 & 0 & G \end{bmatrix} \tag{21}$$

With bulk modulus (*K*) and shear modulus (*G*) defined as:

$$K = \frac{(1+e)p'}{\kappa}, \qquad G = \frac{3K(1-2\nu)}{2(1+\nu)} = \frac{3(1-2\nu)}{2(1+\nu)}\frac{(1+e)p'}{\kappa} \tag{22}$$

with p’ as the mean stress, ν as the Poisson’s ration, and κ as the initial elastic slope for specific volume-mean stress.

In conventional elastoplastic constitutive models, *K* and *G* (and therefore the elastic stress-strain matrix) are often assumed independent of the stress state. In critical state models, however, the tangential bulk and shear moduli are typically assumed to depend on the mean effective stress (SLOAN; ABBO; SHENG, 2001).

The elastic trial stress increment ($d\boldsymbol{\sigma}^{tr}$) is then computed from Hooke’s law:

$$d\boldsymbol{\sigma}^{tr} = \mathbf{C}_{\mathrm{e}}: d\boldsymbol{\varepsilon}^{tr} + \alpha_s ds^{tr} \quad ; \quad \boldsymbol{\sigma}^{tr} = \boldsymbol{\sigma}^{old} + d\boldsymbol{\sigma}^{tr} \tag{23}$$

where, ds^{tr} is the suction increment in the analyzed substep, and

$$\alpha_s = -K\frac{\kappa_s}{(1+e)}\frac{1}{(s+p_{atm})} \tag{24}$$

where κ_s is the elastic stiffness parameter for changes in suction, and p_{atm} is the atmospheric pressure.

For conventional plasticity models, the trial stress increment can be directly used in the stress integration procedure. In non-linear critical state elasticity, however, the trial stress is only used to check if the stress state has changed from elastic to plastic domain.

Once the trial stress is updated, the stress invariants mean normal stress (p’) deviatoric stress (*J*), and Lode’s angle (θ) are updated following Equations 25, 26 and 27, respectively:

$$p' = \frac{\sigma'_x + \sigma'_y + \sigma'_z}{3} \tag{25}$$

$$J = \sqrt{\frac{1}{2}\left[(\sigma'_x - p')^2 + \left(\sigma'_y - p'\right)^2 + (\sigma'_z - p')^2 + 2\left(\tau_{xy}^2 + \tau_{xz}^2 + \tau_{yz}^2\right)\right]} \tag{26}$$

$$\theta = -\frac{1}{3} sin^{-1}\left(\frac{3}{2}\sqrt{3} det \frac{s}{J^3}\right) \tag{27}$$

The TEP model employs the Barcelona Basic Model (BBM) as its constitutive framework to define the yield surface for unsaturated soils, with the formulation presented in Section 3.2.1. The yield function is given in Equation 28.

$$F = \frac{3J^2}{{g_y}^2} - {L_y}^2(p' + p_s)(p_0 - p') \tag{28}$$

where g_y is a function of the Lode angle and $L_y = {}^{M}/_{g_y}\Big|_{\theta=-\pi/6}$

The Lode function depends on the second and third deviatoric stress invariants (J_2 and J_3). When the von Mises model is adopted, the Lode function takes the value one, since von Mises criterion depends only on J_2 and not on the principal stresses distribution (J_3). In TEP, von Mises, Mohr-Coulomb and van Eeckelen criteria are implemented.

Finally, the residual strain and the previous integration stress variable are defined as:

$$d\boldsymbol{\varepsilon}_r = d\boldsymbol{\varepsilon} \tag{29}$$

$$\boldsymbol{\sigma}_{prev} = \boldsymbol{\sigma}_{old} \tag{30}$$

The yield function is then evaluated as $F[\boldsymbol{\sigma}^{tr}, s^{tr}]$. If $F[\boldsymbol{\sigma}^{tr}, s^{tr}] \leq 0$, the stress-strain response remains in the elastic domain, and elastic integration is performed. Otherwise, if $F[\boldsymbol{\sigma}^{tr}, s^{tr}] > 0$, the trial substep enters the plastic domain, indicating that the initial stress state was on the yield surface and that even a small strain increment has triggered plastic yielding.

7.1.2 ***Elastic Integration***

If the trial elastic indicates that the stress state remains within elastic domain, the elastic integration procedure begins. In this case, the strain increment is divided into two, with all substeps assumed to be of equal size, as follows:

$$d\boldsymbol{\varepsilon}^{i} = \frac{d\boldsymbol{\varepsilon}}{2} \tag{31}$$

The stress-strain response is computed for each substep. The elastic constitutive matrix is recalculated based on the previous stress ($\boldsymbol{\sigma}_{prev}$), since it depends on the current stress state and cannot be computed just once. The predicted stress is then obtained as follows:

$$d\boldsymbol{\sigma}^{pred} = \mathbf{C}_{e}\left[\boldsymbol{\sigma}_{prev}\right]: d\boldsymbol{\varepsilon}^{i} + \alpha_{s}\, ds^{i} \quad ; \quad \boldsymbol{\sigma}^{pred} = \boldsymbol{\sigma}^{prev} + d\boldsymbol{\sigma}^{pred} \tag{32}$$

Second-order integration evaluates the stress at an intermediate point within the strain increment, rather than solely at the beginning or end. For the second-order integration matrix and vector, the weighted stress (second-order stress, $\boldsymbol{\sigma}_{\mu}$) is calculated using an integration weight (μ), which ranges from 0 to 1 (typically 1) and is specified by the user in the TEP Integration Control Parameters (ICL 27). This weighted stress adjusts the final stress over the integration increment, providing control over the iterative substepping process. The weighted stress and strain increment are defined in Equations 33 and 34.

$$\boldsymbol{\sigma}_{\mu} = \boldsymbol{\sigma}^{prev} + \mu d\boldsymbol{\sigma}^{pred} \tag{33}$$

$$d\boldsymbol{\varepsilon}^{\mu} = \mu d\boldsymbol{\varepsilon}^{i} \tag{34}$$

The historical variable void ratio is updated based on the volumetric weighted strain increment:

$$e = e_{old} - (1 - e_{old}) d\varepsilon_{vol}^{\mu} \tag{35}$$

where e_{old} is the previously computed void ratio.

The elastic constitutive matrix is recalculated using $\boldsymbol{\sigma}_{\mu}$, and the second-order final stress is computed as follow:

$$d\boldsymbol{\sigma} = \mathbf{C}_e[\,\boldsymbol{\sigma}_{\mu}]: d\boldsymbol{\varepsilon}^i + +\alpha_s\, ds^i \quad ; \quad \boldsymbol{\sigma}^{int} = \boldsymbol{\sigma}^{prev} + d\boldsymbol{\sigma} \tag{36}$$

where $\boldsymbol{\sigma}^{int}$ is an integration stress.

The relative integration error is evaluated according to Equation 37.

$$error = \frac{\sqrt{\sum\left[(\boldsymbol{\sigma}^{int})_{ij} - (\boldsymbol{\sigma}^{pred})_{ij}\right]^2}}{\sqrt{\sum(\boldsymbol{\sigma}^{pred})_{ij}^2}} \tag{37}$$

This error is compared to the elastic integration tolerance, typically set between 10^{-4} and 10^{-6} (user-defined in ICL 27). If the error exceeds the tolerance, the strain increment is further subdivided for a new iteration. If the error is within tolerance, the elastic integration for the current substep is considered converged. In this case, the strain increment is accumulated, and the next substep is integrated until the full strain increment is completed. Once the total increment has been integrated, the stress is checked to ensure it remains within the elastic domain. If the error exceeds the tolerance, the strain increment is further subdivided, and the integration is repeated for smaller substeps until convergence is achieved.

The yield function is evaluated in terms of the integration stress ($\boldsymbol{\sigma}^{int}$). If $F\left[\boldsymbol{\sigma}^{int},\ s^{int}\right] \leq 0$, the response remains elastic and the entire increment is elastic. In this case, the previous stress is simply set equal to the integration stress, and the residual plastic strain is updated accordingly:

$$\boldsymbol{\sigma}^{prev} = \boldsymbol{\sigma}^{int} \tag{38}$$

$$d\boldsymbol{\varepsilon}_{n+1}^r = d\boldsymbol{\varepsilon}_n^r - d\boldsymbol{\varepsilon}^i \tag{39}$$

The historical variable void ratio is updated using $d\boldsymbol{\varepsilon}^i$. Once the integration process ends, the stress for the next step is updated with the integration value, i.e., $\boldsymbol{\sigma}^{new} = \boldsymbol{\sigma}^{int}$.

If $F\left[\boldsymbol{\sigma}^{int}, s^{int}\right] > 0$, the yield surface is reached, and the crossing yield function algorithm is applied.

Due to the non-linear nature of the constitutive laws in the Barcelona Basic Model (BBM) and the complex evolution of internal variables, the stress-strain relationship is non-linear and load-dependent. Consequently, an iterative approach is necessary even for elastic behavior, as no general analytical solution exists for these constitutive differential equations.

7.1.3 ***Plastic Integration***

Two scenarios can lead to plastic integration. Non-linear critical state models use the elastic trial increment only to verify whether the stress state has changed from elastic to plastic. A small trial strain increment is given to determine if the stress state lies within the elastic domain or on the boundary of the yield surface (Figure 55a). If $F[\boldsymbol{\sigma}^{tr}, s^{tr}] \geq 0$, the stress state is already on the yield surface, and the initial trial substep immediately triggers plastic behavior.

In the second scenario (Figure 55b), if $F[\boldsymbol{\sigma}^{int}, s^{int}] > 0$ after the elastic integration, the stress-strain response lies within the plastic domain, indicating that not all of the increment is elastic. In this case, the yield surface has been reached, and the crossing yield function algorithm is applied.

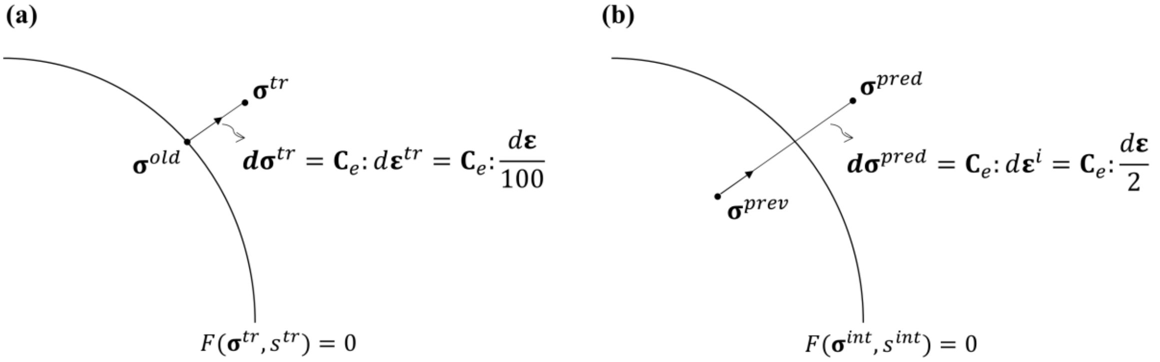

Figure 55. Plastic integration scenarios: (a) After trial elastic stress routine; (b) After elastic integration routine

In the first scenario, the values of $\boldsymbol{\sigma}^{prev}$ ($\boldsymbol{\sigma}^{prev} = \boldsymbol{\sigma}^{old}$) and $d\boldsymbol{\varepsilon}^{r}$ ($d\boldsymbol{\varepsilon}^{r} = d\boldsymbol{\varepsilon}$) are obtained from the trial elastic integration. Plastic integration then begins by dividing the strain increment as:

$$d\boldsymbol{\varepsilon}^{i} = \frac{d\boldsymbol{\varepsilon}^{r}}{2} \tag{40}$$

To proceed, the elastoplastic matrix and the plastic flow matrix associated with the variation in soil suction must be computed. This requires first defining the plastic parameters H and H$_{crit}$:

$$H = -\frac{(1+e){p_0}^*}{\lambda(0)-\kappa}\frac{\partial F}{\partial p_0}\frac{\partial p_0}{\partial {p_0}^*}\frac{\partial G}{\partial \boldsymbol{\sigma}} \tag{41}$$

where:

$$\frac{\partial F}{\partial p_0} = -{L_y}^2(p' + p_s) \quad ; \quad \frac{\partial p_0}{\partial {p_0}^*} = \frac{\lambda(0)-\kappa}{\lambda(s)-\kappa}\left(\frac{{p_0}^*}{p_c}\right)^{\frac{\lambda(0)-\lambda(s)}{\lambda(s)-\kappa}} \tag{42}$$

and,

$$H_{crit} = \frac{\partial F}{\partial \boldsymbol{\sigma}}\mathbf{C}_e\frac{\partial G}{\partial \boldsymbol{\sigma}} \tag{43}$$

The elastoplastic constitutive matrix ($\mathbf{C}_{ep}$) is given by:

$$\mathbf{C}_{ep} = \mathbf{C}_e - \frac{\mathbf{C}_e\frac{\partial G}{\partial \boldsymbol{\sigma}}\left(\frac{\partial F}{\partial \boldsymbol{\sigma}}\right)^T\mathbf{C}_e}{-\frac{\partial F}{\partial \mathcal{H}}\frac{d\mathcal{H}}{d\lambda} + \left(\frac{\partial F}{\partial \boldsymbol{\sigma}}\right)^T\mathbf{C}_e\frac{\partial G}{\partial \boldsymbol{\sigma}}} \tag{44}$$

where $d\mathcal{H}$ is the increment of hardening parameter and, $d\lambda$ being the consistency condition given by:

$$d\lambda = \frac{\left(\frac{\partial \mathrm{F}}{\partial \boldsymbol{\sigma}}\right)^T\mathbf{C}_e d\boldsymbol{\varepsilon}}{-\frac{\partial \mathrm{F}}{\partial \mathcal{H}}\frac{d\mathcal{H}}{d\lambda} + \left(\frac{\partial \mathrm{F}}{\partial \boldsymbol{\sigma}}\right)^T\mathbf{C}_e\frac{\partial \mathrm{G}}{\partial \boldsymbol{\sigma}}} \tag{45}$$

In critical state models, hardening is usually expressed in terms of volumetric plastic strain and isotropic preconsolidation stress. Assuming the hardening parameter ($\mathcal{H}$) corresponds to isotropic preconsolidation stress, the first term of the denominator of Equation 44 reduces to:

$$-\frac{\partial F}{\partial \mathcal{H}}\frac{d\mathcal{H}}{d\lambda} = -\frac{(1+e){p_0}^*}{\lambda(0)-\kappa}\frac{\partial F}{\partial p_0}\frac{\partial p_0}{\partial {p_0}^*}\frac{\partial G}{\partial p} \tag{46}$$

Thus, the denominator of elastoplastic constitutive matrix is the sum of H and H$_{crit}$, i.e., the sums of Equations 41 and 43.

The plastic flow matrix associated with the soil suction variation ($\boldsymbol{\Gamma}_s$) is:

$$\boldsymbol{\Gamma}_s = \left[-K\frac{\kappa_s}{1+e}\left(\frac{1}{s+p_{atm}}\right)\right] - \mathbf{C}_e\left\{\frac{1}{H+H_{crit}}\frac{\partial \mathrm{G}}{\partial \boldsymbol{\sigma}}\frac{\partial \mathrm{F}}{\partial \boldsymbol{\sigma}}\left[-K\frac{\kappa_s}{1+e}\left(\frac{1}{s+p_{atm}}\right)\right] + \frac{\partial \mathrm{F}}{\partial \mathrm{s}}\frac{\partial \mathrm{G}}{\partial \boldsymbol{\sigma}}\right\} \tag{47}$$

The predict stress is then computed as:

$$d\boldsymbol{\sigma}^{pred} = \mathbf{C}_{ep}\colon d\boldsymbol{\varepsilon}^i + \boldsymbol{\Gamma}_s ds^i \quad ; \quad \boldsymbol{\sigma}^{pred} = \boldsymbol{\sigma}^{prev} + d\boldsymbol{\sigma}^{pred} \tag{48}$$

As in the elastic integration, a weighted second-order stress ($\boldsymbol{\sigma}_\mu$) is defined as follow:

$$\boldsymbol{\sigma}_\mu = \boldsymbol{\sigma}^{prev} + \mu d\boldsymbol{\sigma}^{pred} \tag{49}$$

The strain is decomposed into elastic and plastic components, following additive strain decomposition. Throughout this work, the subscript *e* refers to elastic and the subscript *p* to plastic.

$$d\boldsymbol{\varepsilon}_e^{pred} = \mathbf{C}_e^{-1}\colon\left(d\boldsymbol{\sigma}^{pred} - \alpha_s ds^i\right) \quad ; \quad d\boldsymbol{\varepsilon}_p^{pred} = d\boldsymbol{\varepsilon}^i - d\boldsymbol{\varepsilon}_e^{pred} \tag{50}$$

The weighted plastic and total strain increments are:

$$d\boldsymbol{\varepsilon}_p^\mu = \mu d\boldsymbol{\varepsilon}_p^{pred} \quad ; \quad d\boldsymbol{\varepsilon}^\mu = \mu d\boldsymbol{\varepsilon}^i \tag{51}$$

The history variables are updated by considering the volumetric strain for both the plastic increment strain ($d\boldsymbol{\varepsilon}_p^\mu$) and the total increment strain ($d\boldsymbol{\varepsilon}^\mu$). The preconsolidation stress for saturated condition is updated according to the hardening law:

$$dp_0^* = \frac{(1+e)}{\lambda(0)-\kappa}p_{0,prev}^* d\varepsilon_v^p \quad ; \quad p_0^* = p_{0,prev}^* + dp_0^* \tag{52}$$

where $p^*_{0,prev}$ is the previous value of preconsolidation stress for saturated condition stored in the respective historical variable.

The historical variable void ratio is updated as follows:

$$e = e_{prev} - \left(1 + e_{prev}\right) d\varepsilon_v \tag{53}$$

where e_{prev} is the previous value of void ratio stored in the historical variable.

At the end of the plastic integration, the final stress and plastic strain are recomputed with the second-order matrices. Both stress and strain are calculated with the elastic and elastoplastic matrix obtained with the second-order stress ($\boldsymbol{\sigma}_\mu$).

$$d\boldsymbol{\sigma} = \mathbf{C}_{ep}: d\boldsymbol{\varepsilon}^i + \boldsymbol{\Gamma}_s ds^i \quad ; \quad \boldsymbol{\sigma}^{int} = \boldsymbol{\sigma}^{prev} + d\boldsymbol{\sigma} \tag{54}$$

$$d\boldsymbol{\varepsilon}_e = \mathbf{C}_e^{-1}: \left(d\boldsymbol{\sigma} - \alpha_s ds^i\right) \quad ; \; d\boldsymbol{\varepsilon}_p = d\boldsymbol{\varepsilon}^i - d\boldsymbol{\varepsilon}_e \tag{55}$$

Convergence is evaluated by comparing the relative integration error against the tolerance defined for plastic integration (typically between 10^{-4} and 10^{-2}, user-defined input). If the error exceeds the tolerance, plastic integration is restarted with a new value of strain increment. Otherwise, convergence is achieved, and historical variables are updated with the latest computed strain components ($d\boldsymbol{\varepsilon}^i$ and $d\boldsymbol{\varepsilon}_p$).

One drawback of this procedure is that computed stresses may not fully satisfy the yield criterion at the end of each step. In such cases, a correction method, known as the Yield Correction Algorithm, is required to return the stresses to the yield surface.

7.1.4 ***Yield Correction Algorithm***

In the integration process for multiaxial elastoplastic models, an initial stress state may lie inside or on the boundary of admissible stresses domain. Upon a strain increase, the predicted stress may exceed the yield surface tolerance (typically 10^{-8}). If this occurs, the stress state falls outside the admissible domain and requires correction through the yield correction algorithm.

Once plastic integration convergence is achieved, the yield function is recalculated using the integration stress ($\boldsymbol{\sigma}^{int}$) and the integration suction (s^{int}). If $\left|F\left[\boldsymbol{\sigma}^{int}, s^{int}\right]\right|$ exceeds the yield surface tolerance, the yield correction algorithm is applied. Else, if $\left|F\left[\boldsymbol{\sigma}^{int}, s^{int}\right]\right|$ is within the tolerance, the previous stress and residual strain are updated, as follow:

$$\boldsymbol{\sigma}^{prev} = \boldsymbol{\sigma}^{int} \tag{56}$$

$$d\boldsymbol{\varepsilon}_{n+1}^{r} = d\boldsymbol{\varepsilon}_{n}^{r} - d\boldsymbol{\varepsilon}^{i} \tag{57}$$

For non-associative flow, the return path to the yield surface does not follow a normal vector at the nearest point, as in the associated case. Instead, the direction of the plastic increment aligns with the gradient of the plastic potential function. The yield correction algorithm for non-associative flow starts by computing the plastic multiplier obtained from the plastic consistency condition. When the stress state drifts outside the surface after convergence, the plastic multiplier that corrects the stress back to the surface is given by a Taylor series expansion (DONG, 2023):

$$\lambda = \frac{F[\boldsymbol{\sigma}^{int}, s^{int}]}{H_{crit} - \frac{\partial \mathrm{F}}{\partial p_0^*} \frac{(1+e)}{\lambda(0) - \kappa} p_0^* \sum \left(\frac{\partial G}{\partial \boldsymbol{\sigma}}\right)_{ij}} \tag{58}$$

The stress correction considers the plastic multiplier, the elastic matrix evaluated at the previously computed stress ($\boldsymbol{\sigma}^{int}$) and the gradient of the plastic potential function, which indicates the direction of the plastic flow. The stress correction is given by Equation 59.

$$\boldsymbol{\sigma}^{corr} = -\lambda \mathbf{C}_e \frac{\partial G}{\partial \boldsymbol{\sigma}} \quad ; \quad \boldsymbol{\sigma}^{c} = \boldsymbol{\sigma}^{int} + \boldsymbol{\sigma}^{corr} \tag{59}$$

The corrected plastic strain increment is then obtained as:

$$d\boldsymbol{\varepsilon}_{p}^{corr} = \lambda \frac{\partial G}{\partial \boldsymbol{\sigma}} \tag{60}$$

Using this value, the corrected isotropic preconsolidation stress for saturated conditions and historical value update is:

$$p^*_{0,corr} = \frac{1+e}{\lambda(0)-\kappa} p^*_0 \varepsilon^{corr}_{p,v} \quad ; \quad p^*_0 = p^*_0 + p^*_{0,corr} \tag{61}$$

where, $\varepsilon^{corr}_{p,v}$ is the volumetric deformation in relation to the vector $\boldsymbol{\varepsilon}^{corr}_{p}$.

Convergence of the yield correction algorithm is verified by evaluating the yield function with the stress correction ($\boldsymbol{\sigma}^c$). If $F[\boldsymbol{\sigma}^c, s]$ exceeds the yield surface tolerance, the algorithm has not converged, and a new interaction is required. Otherwise, convergence is achieved, and the stress and strain are updated, as follow:

$$\boldsymbol{\sigma}^{int} = \boldsymbol{\sigma}^{c} \tag{62}$$

$$\boldsymbol{\sigma}^{prev} = \boldsymbol{\sigma}^{int} \tag{63}$$

$$d\boldsymbol{\varepsilon}^r_{n+1} = d\boldsymbol{\varepsilon}^r_n - d\boldsymbol{\varepsilon}^i \tag{64}$$

7.1.5 *Crossing Yield Surface Algorithm*

In the second yield scenario (Figure 55b), when $F\left[\boldsymbol{\sigma}^{int}, s^{int}\right] > 0$, the stress state lies within the plastic domain and not all of the increment is elastic. At any point in the solution, the stress-strain response may be either plastic or elastic. When a stress state transitions from elastic to plastic, it is necessary to determine the purely elastic portion of the stress increment (SLOAN, 1987).

To achieve this, the crossing yield surface algorithm identifies the intersection between the stress path and the yield surface. This requires solving for a scalar parameter α that satisfies Equation 65.

$$F[\boldsymbol{\sigma}, \mathcal{H}_0] = 0 \tag{65}$$

where $\mathcal{H}_0$ is a hardening parameter that depends on the strain history, and

$$\boldsymbol{\sigma} = \boldsymbol{\sigma_0} + \alpha\Delta\boldsymbol{\sigma}, \;\; 0 < \alpha < 1 \tag{66}$$

The exact yield condition given in Equation 66 is approximated with a small positive tolerance, to account for finite precision arithmetic. Since the yield function is nonlinear, α is obtained using the Newton–Raphson method:

$$\boldsymbol{\sigma}_k = \boldsymbol{\sigma}_{k-1} + \alpha_k \Delta\boldsymbol{\sigma} \tag{67}$$

$$\alpha_{k+1} = \alpha_k - \frac{F[\boldsymbol{\sigma}_k, \mathcal{H}_0]}{\frac{\partial F}{\partial \boldsymbol{\sigma}} \Delta\boldsymbol{\sigma}} \tag{68}$$

where $(\partial \mathrm{F}/\, \partial \boldsymbol{\sigma})$ is evaluated at the stress $\boldsymbol{\sigma}_k$.

For plasticity models, the Modified Euler Integration with Error Control can be combined with the crossing yield surface algorithm to enhance accuracy by integrating the plastic increment based on mid-point stress. The modified Euler scheme gives the estimate of $\boldsymbol{\sigma}_{k+1}$, as follow (SLOAN, 1987):

$$\boldsymbol{\sigma}_{k+1} = \boldsymbol{\sigma}_k + \frac{1}{2}(\Delta\boldsymbol{\sigma}_1 + \Delta\boldsymbol{\sigma}_2) \tag{69}$$

where:

$$\Delta\boldsymbol{\sigma}_1 = \mathbf{C}_{ep}(\boldsymbol{\sigma}_k, \mathcal{H}_0)\Delta\boldsymbol{\varepsilon}_k \quad ; \quad \Delta\boldsymbol{\sigma}_2 = \mathbf{C}_{ep}(\boldsymbol{\sigma}_{k+1}, \mathcal{H}_{k+1})\Delta\boldsymbol{\varepsilon}_k \tag{70}$$

In the TEP Model, the crossing yield surface algorithm is triggered when $F\left[\boldsymbol{\sigma}^{int}, s^{int}\right] > 0$ during elastic integration. At this stage, the stress tensor $\boldsymbol{\sigma}^{prev}$ is equivalent to $\boldsymbol{\sigma}_k$, whereas $\boldsymbol{\sigma}^{int}$ corresponds to $\boldsymbol{\sigma}_{k+1}$. The scalar α is calculated through the Newton-Raphson technique:

$$\alpha = \frac{F[\boldsymbol{\sigma}^{prev}, s^{prev}]}{\frac{\partial F}{\partial \boldsymbol{\sigma}}(\boldsymbol{\sigma}^{int} - \boldsymbol{\sigma}^{prev}) + \frac{\partial F}{\partial s}(s^{int} - s^{prev})} \tag{71}$$

Both derivatives $\partial \mathrm{F}/\, \partial \boldsymbol{\sigma}$ and $\partial \mathrm{F}/\, \partial \mathrm{s}$ are evaluated at the mid-point stress and suction (Equation 71), i.e., the average stress between $\boldsymbol{\sigma}^{int}$ and $\boldsymbol{\sigma}^{prev}$, and average suction between s^{int} and s^{prev}. The correct stress and suction is then given by:

$$\boldsymbol{\sigma}^{c} = \boldsymbol{\sigma}^{prev} + \alpha\left(\boldsymbol{\sigma}^{int} - \boldsymbol{\sigma}^{prev}\right) \tag{72}$$

$$s^{c} = s^{prev} + \alpha\left(s^{int} - s^{prev}\right) \tag{73}$$

If $|F[\boldsymbol{\sigma}^{c}, s^{c}]| \leq tol1$, convergence is achieved and α is computed:

$$\alpha = \frac{\sqrt{\sum(\boldsymbol{\sigma}^{c} - \boldsymbol{\sigma}^{prev})^2}}{\sqrt{\sum(\boldsymbol{\sigma}^{int} - \boldsymbol{\sigma}^{prev})^2}} \tag{74}$$

If the denominator is smaller than 10^{-5}, α is set to zero, indicating purely plastic strain. If $\alpha > 1$, it is set to one, meaning that the response remains fully elastic as the stress increase was insufficient to reach plasticity. For elastic-plastic transition, $0 < \alpha < 1$.

If $F[\boldsymbol{\sigma}^{c}, s^{c}] > tol1$, the stress $\boldsymbol{\sigma}^{int}$ is set to $\boldsymbol{\sigma}^{c}$ and, if $F[\boldsymbol{\sigma}^{c}, s^{c}] < -tol1$, the stress $\boldsymbol{\sigma}^{prev}$ is set to $\boldsymbol{\sigma}^{c}$. In both cases, the iterative process to compute the scalar α restart.

Upon convergence (i.e., $|F[\boldsymbol{\sigma}^{c}, s^{c}]| \leq tol1$), the values of α and $\boldsymbol{\sigma}^{c}$ are computed, and the strains are updated as follows:

$$d\boldsymbol{\varepsilon}^{r} = d\boldsymbol{\varepsilon}^{r} - \alpha d\boldsymbol{\varepsilon}^{i} \tag{75}$$

$$d\boldsymbol{\varepsilon}^{ic} = \alpha d\boldsymbol{\varepsilon}^{i} \tag{76}$$

The historical variable void ratio is updated based on $d\boldsymbol{\varepsilon}^{ic}$, and the previous stress is set to $\boldsymbol{\sigma}^{c}$, representing the stress state at the yield surface due to a purely elastic strain. Any subsequent strain increment will result in plastic integration, as outlined in the first scenario (Figure 55a).

In summary, this algorithm isolates the elastic portion of the stress increment and determines the stress state that reaches the yield surface without plastic deformation. The scalar α identifies this critical point, ensuring that the transition from elastic to plastic behavior is captured accurately.

7.1.6 Flowchart of the TEP Stress Integration Algorithm

Figure 56 illustrates the flowchart of the TEP stress integration algorithm, as an overview of the integration scheme after the detailed description of each routine.

The stress update starts with the assumption of a fully elastic response for the entire increment. The decision points of the algorithm, and thus the definition of the subsequent procedure (elastic or plastic integration, crossing yield surface, or yield correction algorithm), are determined by the evaluation of the yield function value. All computational routines that compose the TEP model, except for the trial elastic stress, adopt an internal iterative scheme to reach convergence.

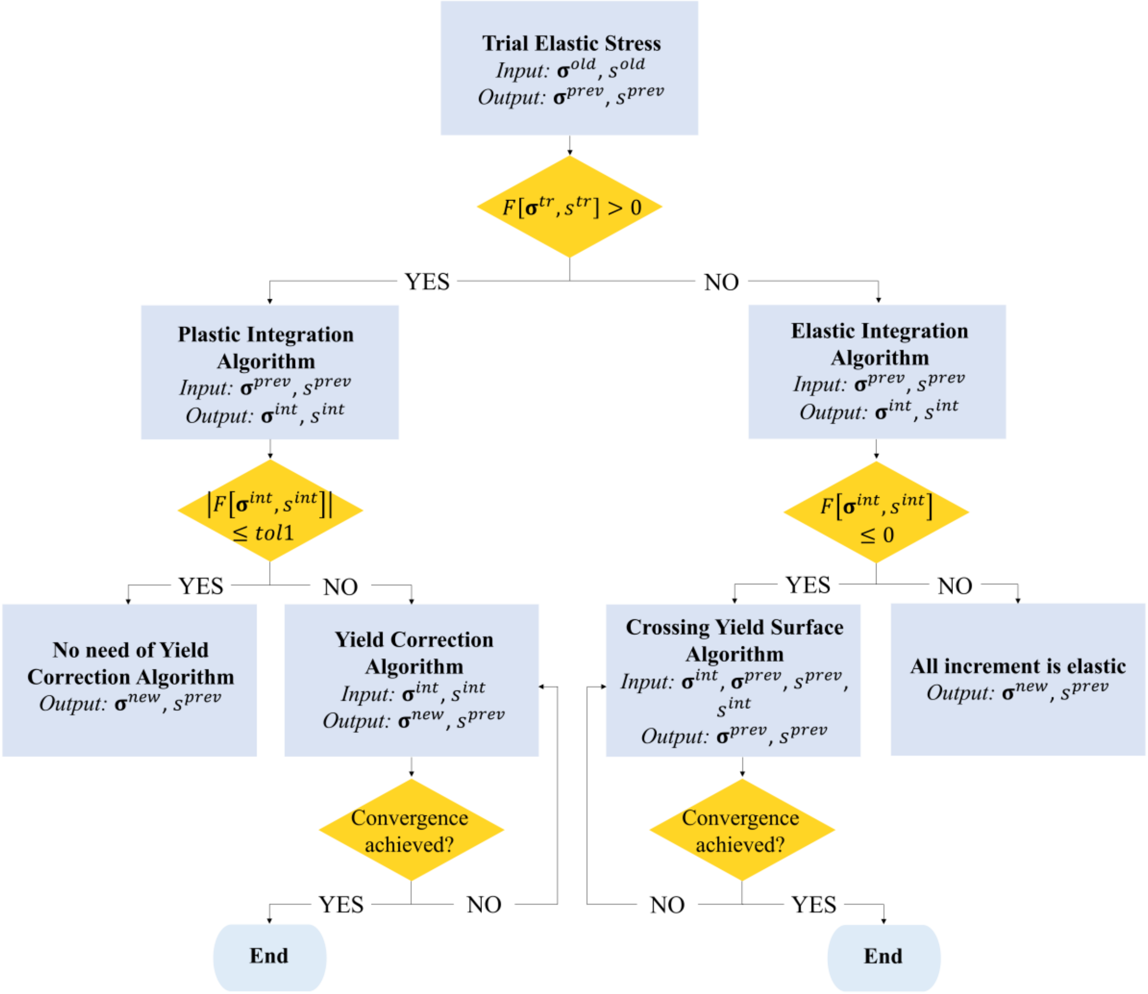

Figure 56. Flowchart summarizing the sequence of computational routines employed in the TEP model for the incremental integration scheme

7.2 Incorporation of the Suction-Increase Curve into the TEP Model

During the drying process, the gradual increase in suction affects both the size and position of the yield surface, even if the total stress is held constant and the external stress state remains unchanged. The increase in suction induces plastic strain once suction reaches a maximum previously attained value, namely s_0. This value represents the highest past suction ever experienced by the soil.

Suction hardening occurs even in the absence of increase in the plastic stress. The soil strain develops as a material response to maintain mechanical equilibrium under varying suction. This behavior can be effectively captured by coupled hydro-mechanical models, such as the Barcelona Basic Model (BBM), in which suction influenced both the elastic stiffness and the plastic hardening. In this framework, Alonso, Gens and Josa (1990) first introduced the definition and behavior of the so-called SI curve (suction-increase curve) as a yield curve in their original paper. Figure 57 illustrates the parameters associated with the yield suction and the location of the yield curves in the (p, s) plane, where, κ_s is the elastic stiffness parameter for changes in suction, λ_s is the stiffness parameter for changes in suction for virgin states of the soil, and s_0 is the hardening parameter of the suction increase yield curve.

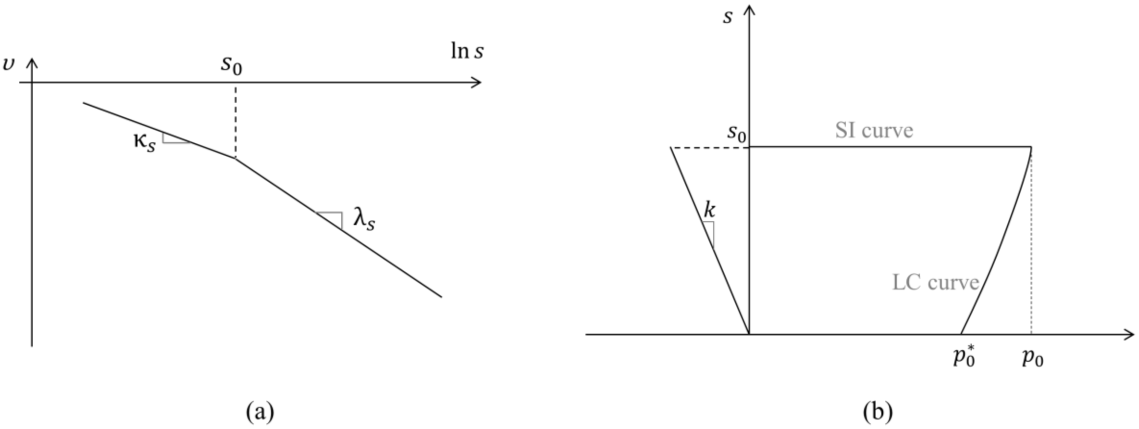

Figure 57. (a) Definition of yield suction, s_0; (b) Yield curves in (p, s) space (Modified from ALONSO; GENS; JOSA, 1990)

However, the SI curve is not included in the current BBM formulation implemented in the program CODE_BRIGHT. Plastic suction effects within the yield surface are currently accounted for only in the Barcelona Expansive Model (BExM) (ALONSO; VAUNAT; GENS, 1999) and in the double-structured expansive models (SÁNCHEZ et al., 2005). The main challenge in implement the SI curve relies in the discontinuity that arises at the intersection of the two discrete yield surface: LC and SI curves.

To address this issue, Pedroso and Farias (2011) proposed an extension of the BBM in which a single smooth yield surface in the stress-suction space describe both the LC and SI curves. This modification simplifies the implementation and enables the simulation of elastoplastic behavior under both mechanical and hydraulic loading cycles.

In this work, the modification of the BBM proposed by Pedroso and Farias (2011) was implemented in the program CODE_BRIGHT, within the Thermo-Elastoplastic Model for soils (TEP). This is a mechanical constitute model that employs an explicit integration scheme with error control (SLOAN, 1987; SLOAN; ABBO; SHENG, 2001). The formulation of the TEP currently implemented in CODE_BRIGHT was detailed in the previous section, and the modifications introduced to incorporate the SI curve are presented here.

The BBM adopts a yield surface similar to that of the modified Cam Clay Model, but with its size dependent on suction through the LC curve. The SI curve is represented as a plane parallel to the suction axis. Together, the LC and the SI yield loci enclose the elastic region. To overcome the discontinuity between LC and SI intersection, the so-called corner, Pedroso and Farias (2011) introduced a single smooth yield surface:

$$F = \frac{3J^2}{g_y^2} - L_y^2(p' + p_s)(p_0 - p') + C \tag{77}$$

In which,

$$C(s, s_0) = p_c^2 \left[exp\left(\frac{B(s - s_0)}{p_c}\right) - exp\left(-\frac{Bs_0}{p_c}\right)\right] \tag{78}$$

The additional term in the original yield function acts as a cap in the stress-suction space (Figure 58), depending only on suction and the hardening parameter of suction, s_0, which is treated in the implementation as a historical variable. The modified yield function introduces one additional parameter, B, a non-dimensional constant that controls the smoothness of the LC–SI transition. As B increases, the transition between the two surfaces becomes less smooth.

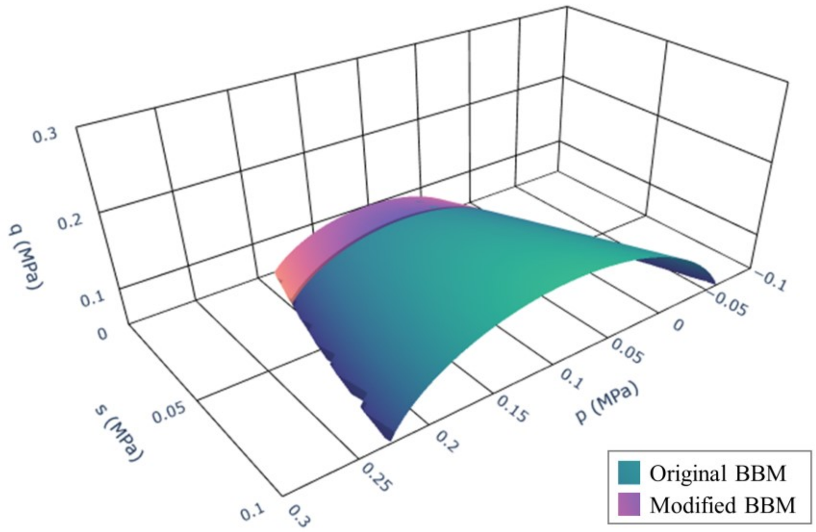

Figure 58. Yield surfaces: Original BBM and Modified BBM proposed by Farias and Pedroso (2011)

The following formulation presented here corresponds to the modifications introduced in the original equations to account for the changes in the yield surface definition and to incorporate the effect of plastic strain induced by drying. All other aspects of the formulation, not addressed in this section, remain identical to those of the original BBM implemented in the TEP.

The hardening law associated with increase in suction, when the SI yield locus is reached following plastic strain, has an effect similar to that of plastic strain induced by stress changes. In this way, the LC and SI curves are simply coupled by controlling their position through the total plastic strain (ALONSO; GENS; JOSA, 1991). The hardening law for increase in suction is expressed as follow:

$$\frac{ds_0}{(s_0 + p_{atm})} = \frac{(1+e)}{\lambda_s - \kappa_s} d\varepsilon_v^p \tag{79}$$

During loading or collapse paths, in which the LC curve shifts and changes shape, the SI curve is decoupled. That is, no movement of the SI curve occurs when plastic strains develop along these paths. To reproduce this behavior numerically, the derivative of the yield function with respect to the historical variable s_0 was evaluated. If the derivative is negative, the hardening parameter of the suction increase yield curve is updated, since this condition indicates plastic evolution in the direction of the SI curve; otherwise, the increment of the hardening parameter s_0 remains null.

The elastoplastic loading condition and the evolution of the yield surface are given by Equation 80, which requires the definition of gradients. For the modified yield surface, the gradient with respect to stress remains the same as in the original BBM, while only the gradient in relation to suction changing, as expressed by Equation 81.

$$\frac{\partial F}{\partial \boldsymbol{\sigma}} : \mathbf{C}_{ep} : d\boldsymbol{\varepsilon} + \frac{\partial F}{\partial s} ds > 0 \tag{80}$$

$$\frac{\partial F}{\partial s} = \frac{\partial F}{\partial p_s}\frac{\partial p_s}{\partial s} + \frac{\partial F}{\partial p_0}\frac{\partial p_0}{\partial s} + Bp_c exp\left[\frac{B(s - s_0)}{p_c}\right] \tag{81}$$

The plastic (or hardening) modulus, used to compute both the elastoplastic matrix ($\mathbf{C}_{ep}$) and the plastic flow matrix associate with the soil suction variation ($\boldsymbol{\Gamma}_s$), was modified to incorporate the changes introduced in the yield surface equation and to satisfy the consistency condition, as expressed in Equation 82:

$$H = -\left[\frac{(1+e)p_0^*}{\lambda(0)-\kappa}\frac{\partial F}{\partial p_0}\frac{\partial p_0}{\partial p_0^*}\frac{\partial G}{\partial \boldsymbol{\sigma}} + \frac{(1+e)(s_0+p_{atm})}{\lambda_s-\kappa_s}\frac{\partial F}{\partial s_0}\frac{\partial G}{\partial \boldsymbol{\sigma}}\right] \tag{82}$$

where,

$$\frac{\partial F}{\partial s_0} = -Bp_c exp\left[\frac{B(s-s_0)}{p_c}\right] + Bp_c exp\left[-\frac{Bs_0}{p_c}\right] \tag{83}$$

Finally, the plastic multiplier obtained from the plastic consistency condition is now computed according to Equation 84. In the TEP routine, which employs an explicit substepping integration scheme, the plastic multiplier is evaluated using a Taylor series expansion around the drifted stress state with respect to the updated bounding surface (DONG, 2023).

$$\lambda = \frac{F[\boldsymbol{\sigma}, s]}{H_{crit} - \frac{\partial F}{\partial p_0^*}\frac{(1+e)}{\lambda(0)-\kappa}p_0^*\sum\left(\frac{\partial \mathrm{G}}{\partial \boldsymbol{\sigma}}\right)_{ij} - \frac{\partial F}{\partial s_0}\frac{(1+e)(s_0+p_{atm})}{\lambda_s-\kappa_s}\sum\left(\frac{\partial G}{\partial \boldsymbol{\sigma}}\right)_{ij}} \tag{84}$$

A validation exercise was carried out to illustrate the proposed approach. Alonso, Gens, and Josa (1990) presented representative examples of triaxial stress paths and BBM predictions using the set of mechanical parameters listed in Table 20. The example considered here involves a drying–wetting cycle in which a maximum suction of 0.3 MPa is applied. The soil is initially saturated under a constant confining stress of 0.15 MPa, followed by a drying path and subsequent wetting until full saturation is reached. The sample is then subjected to a p-loading path up to 0.6 MPa, with the deviatoric stress maintained at zero throughout the simulation. This example illustrates the role of the SI curve, since the applied suction exceeds the value of s_0 value. Table 20 also presents the additional parameter required for the modified BBM and the consideration of the SI curve.

Table 20. Mechanical parameters used in the numerical simulation (ALONSO; GENS; JOSA, 1990; PEDROSO; FARIAS, 2011)

BBM original parameters (ALONSO; GENS; JOSA, 1990)		
$\lambda(0)$		0.2
κ		0.02
r		0.75
β	MPa^{-1}	12.5
p_c	MPa	0.1
λ_s		0.08
κ_s		0.008
M		1
k		0.7
p_0^*	MPa	0.2
s_0	MPa	0.025
e_0		0.9
Additional parameter for modified BBM (PEDROSO; FARIAS, 2011)		
B		1000

The numerical simulation of the triaxial test was carried out using CODE_BRIGHT. The geometry considered was a rectangle with a height of 0.10 m and a base of 0.025 m, defined as axisymmetric around the y-axis. The finite element mesh consisted of 600 structured quadrilateral elements and 656 nodes.

Figure 59 compares the results presented by Alonso, Gens, and Josa (1990) with the numerical simulation performed using the implementation of the SI curve in CODE_BRIGHT. To facilitate convergence during the drying process, the parameter k (which describes the increase in cohesion with suction) was adjusted from 0.6 to 0.7. The numerical results show good agreement with the reference data for the different simulated paths: drying (AB path), wetting (BC path), and loading (CD path).

Figure 60 illustrates the evolution of the LC and SI curves along the drying–wetting and loading paths. The drying process induces net compaction of the sample, and the resulting irreversible deformation shifts both the SI and LC curves, representing the coupling between them during drying. However, the evolution of the LC curve along the loading path does not translate into any corresponding evolution of the SI curve. This behavior was expected and was accurately captured by the numerical simulation.

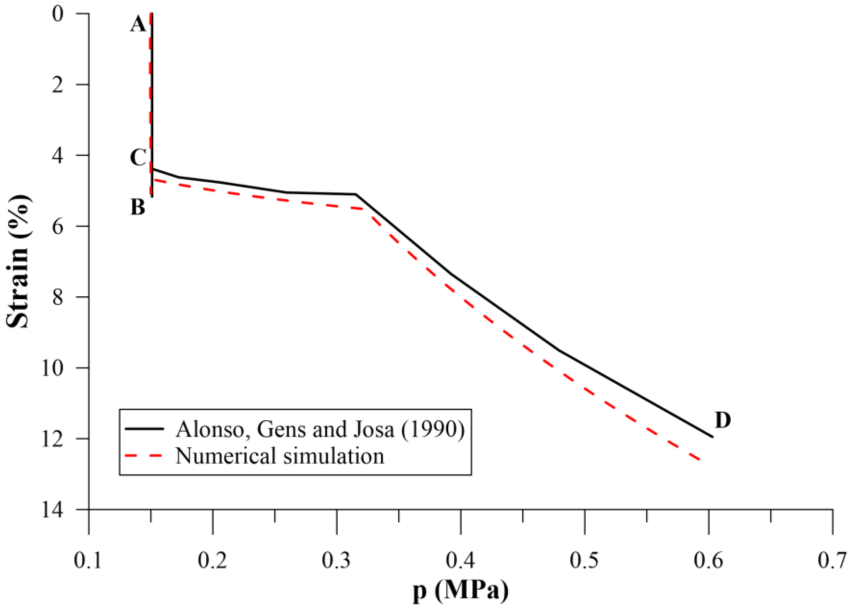

Figure 59. Numerical simulation of triaxial stress path involving drying–wetting cycle and comparison with Alonso, Gens and Josa (1990) results

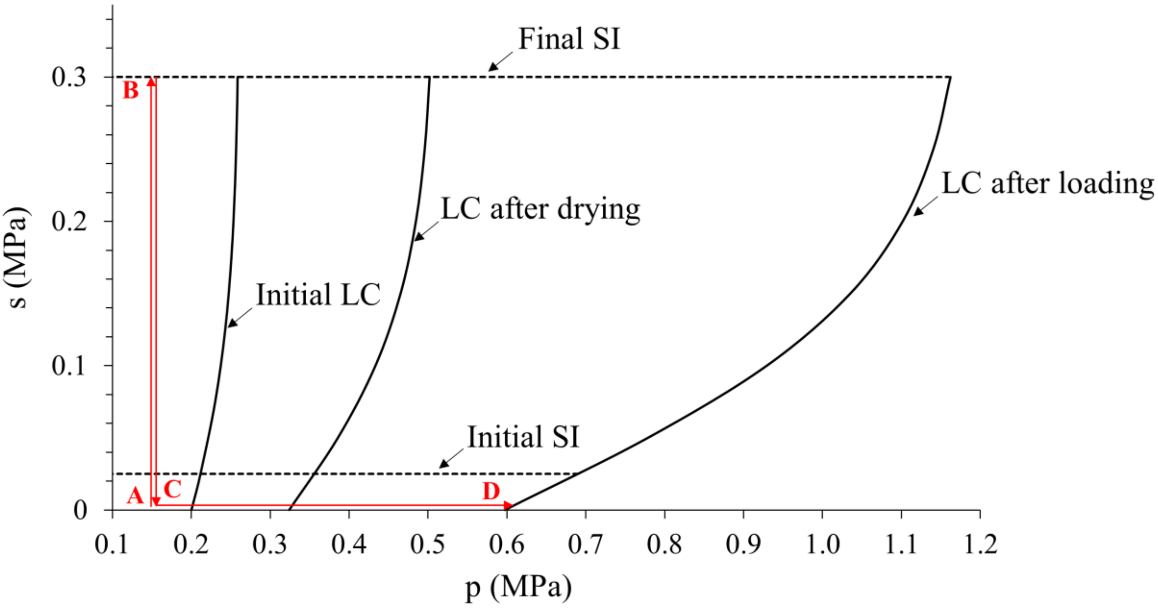

Figure 60. Evolution of the loading–collapse (LC) and suction–increase (SI) curves along drying–wetting and loading paths

8 RESULTS AND DISCUSSIONS: EXTENDED BBM WITH SI CURVE

In this chapter, the results of two sets of numerical simulations are presented. The first concerns the volumetric shrinkage test performed on the materials composing the dam, while the second addresses the operation of the earth dam itself. Both analyses were carried out using the Barcelona Basic Model (BBM) extended with the suction increase (SI) curve, whose formulation was discussed in Section 7. This extension of the BBM made it possible to examine the stress–strain response under drying conditions and to investigate whether the observed dam settlements can be interpreted as a drying-induced hardening.

8.1 Volumetric shrinkage test

The implementation of the SI curve into the TEP Model enabled, for the first time, the numerical simulation of the volumetric shrinkage test due to drying for both compacted and undisturbed Itaipu soils, as described in Section 4 (Item 4.4). This laboratory test consists of a free shrinkage experiment in which the soil is subjected to air-drying and the volumetric strain is determined using a laser profilometry technique. Suction is obtained indirectly from the monitored mass loss over time in combination with the soil water retention curve.

The numerical simulation of this test provides a means to assess and calibrate the mechanical parameters governing the drying process of the Itaipu earth dam soil. The geometry considered was a rectangle with a height of 0.019 m and a base of 0.037 m, defined as axisymmetric around the y-axis. The finite element mesh consisted of 703 structured quadrilateral elements and 760 nodes (*Figure 61*).

The mechanical parameters adopted in the numerical simulation of the volumetric shrinkage test were the same as those used in the simulation of the earth dam, as described in Section 5 (Item 5.2). Table 21 summarizes the mechanical parameters related to the drying process, including those required for the extension of the BBM with the SI curve, for both compacted and undisturbed (foundation) soils.

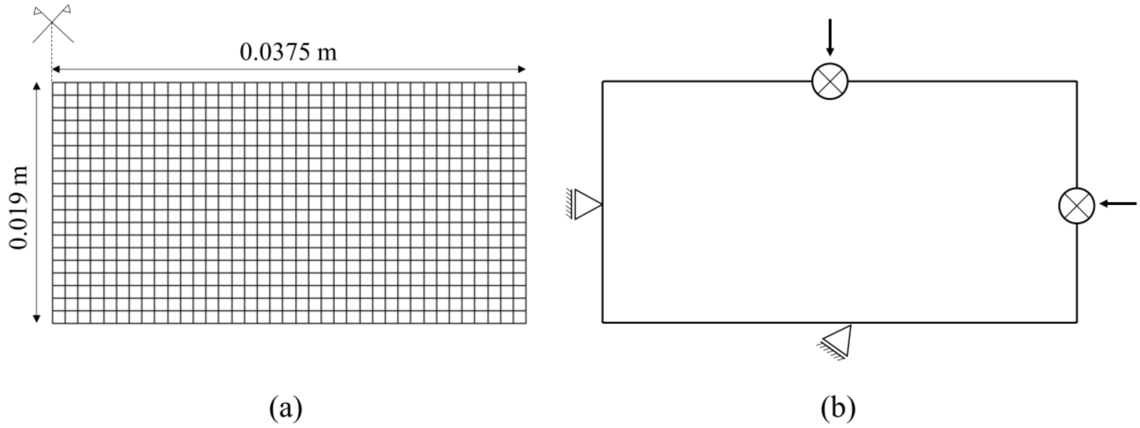

Figure 61. Numerical simulation setup for the volumetric shrinkage test during drying: (a) Geometry and mesh; (b) Boundary conditions

Table 21. Mechanical parameters related to the drying process: undisturbed (foundation) and compacted soil

Mechanical Constitutive Parameters		Red Clay - Foundation	Compacted Soil	Unit
κ_s	Elastic stiffness parameter for changes in suction	4.0×10^{-3}	8.0×10^{-3}	-
λ_s	Stiffness parameter for changes in suction for virgin states of the soil	8.0×10^{-2}	0.244	-
s_0	Hardening parameter of the suction increase yield curve	9.0	10.0	MPa
B	Non-dimensional constant that controls the smoothness of the LC–SI transition	1000	1000	-

Figure 62 and Figure 63 present the numerical simulation of the volumetric shrinkage test for undisturbed (foundation) and compacted soils, respectively.

These results further validate the BBM extended model with the SI curve implementation, since in both cases the model was able to reproduce the soil behavior during the drying process. The simulations also confirmed the suitability of the selected mechanical parameters, particularly those associated with drying-induced plasticity. Considering that the laboratory specimens are representative of the foundation soil and the compacted embankment, these parameters can therefore be employed to assess the behavior of the earth dam.

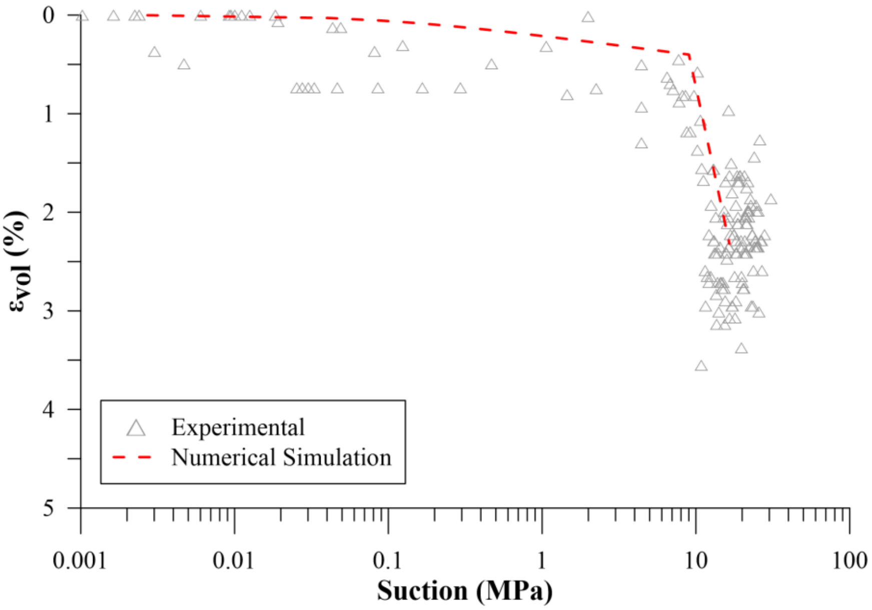

Figure 62. Numerical simulation the volumetric shrinkage test due to drying for undisturbed soil (red clay – foundation)

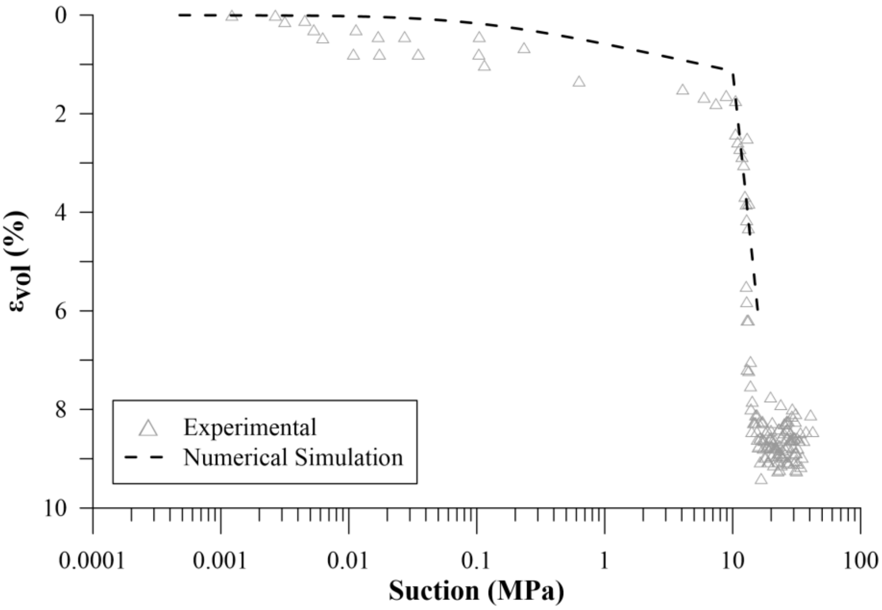

Figure 63. Numerical simulation the volumetric shrinkage test due to drying for compacted soil

8.2 Dam operation considering the SI Curve

The numerical simulation using the BBM extended with the SI curve followed the same procedures described previously. Thus, the geometry, adopted parameters, boundary conditions, finite element mesh, and the overall numerical framework were kept identical to those employed in the initial simulation with the original BBM. The only difference between the analyses was the adoption of the model with the implemented SI curve and the inclusion of the parameters related to the drying process, including those required for the BBM extension with the SI curve, as presented in Table 21.

Figure 64 presents the comparison between the numerical simulation, now considering the SI curve in the constitutive model, and the settlement records obtained from two settlement gauges located at station 135+50, covering the entire operational period of the dam. For reference, Figure 64 also shows the results of the simulation carried out with the original BBM. Figure 65 illustrates the numerical simulation results against the settlements recorded by the reference marker MR-L-23, installed on the crest near station 135+50, using both constitutive models: the original BBM and the BBM extended with the SI curve.

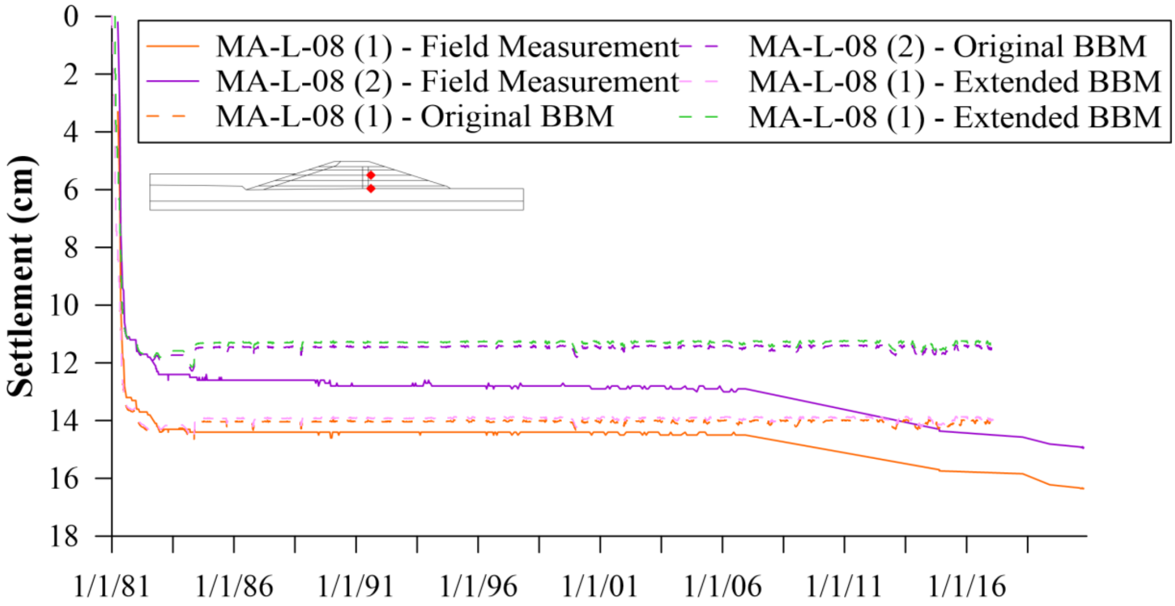

Figure 64. MA-L-08 - Settlement during operation: field measurement and numerical simulation for both original BBM and extended BBM with SI Curve

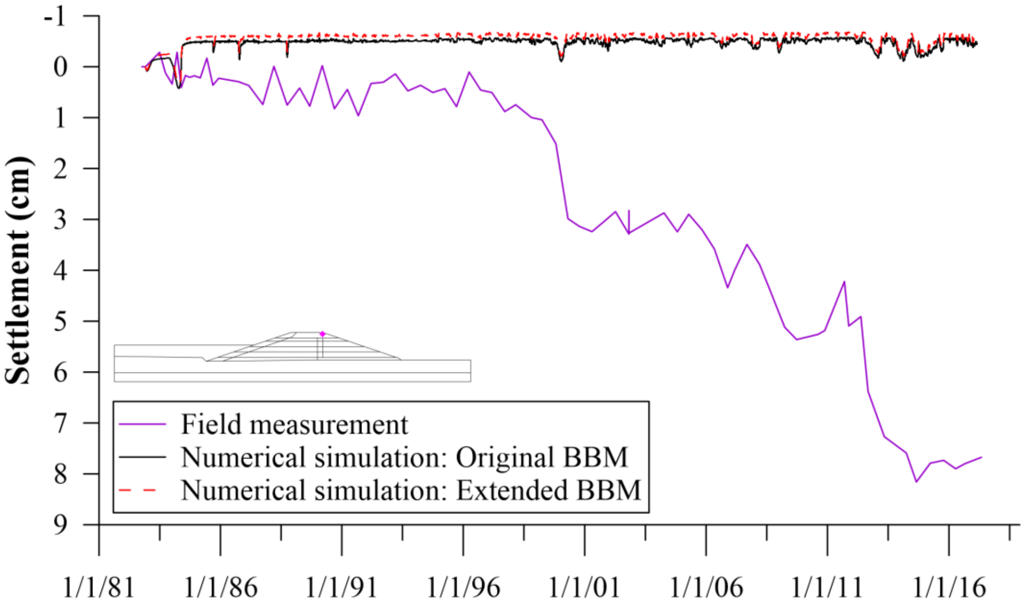

Figure 65. MR-L-23 -Crest settlement during operation: field measurement and numerical simulation for both original BBM and extended BBM with SI Curve

In both Figure 64 and Figure 65, the numerical results obtained with the original BBM and with the BBM extended with the SI curve are practically indistinguishable. This outcome is explained by the fact that the suction variations during the operation stage, caused by reservoir water-level fluctuations, were not sufficiently large to reach the maximum past suction previously experienced by the soil, either in the foundation layer or in the compacted embankment. The fundamental premise for activating the SI curve in the numerical simulation, i.e., suction reaching a maximum previously attained value (s_0), was therefore not met. Laboratory volumetric shrinkage tests due to drying indicated that the hardening parameter of the SI yield curve is high for both the foundation and the compacted dam materials, on the order of 10 MPa. Consequently, the SI curve was never activated throughout the numerical simulation, reducing the analysis to an identical response to that obtained with the original BBM.

Figure 66 shows the evolution of pore water pressure at random select points within the embankment, particularly in the lower zones near the rip-rap, where suction variations are more pronounced due to reservoir drawdowns. These results further support the conclusion that suction changes during the operation stage were insufficient to activate the SI curve.

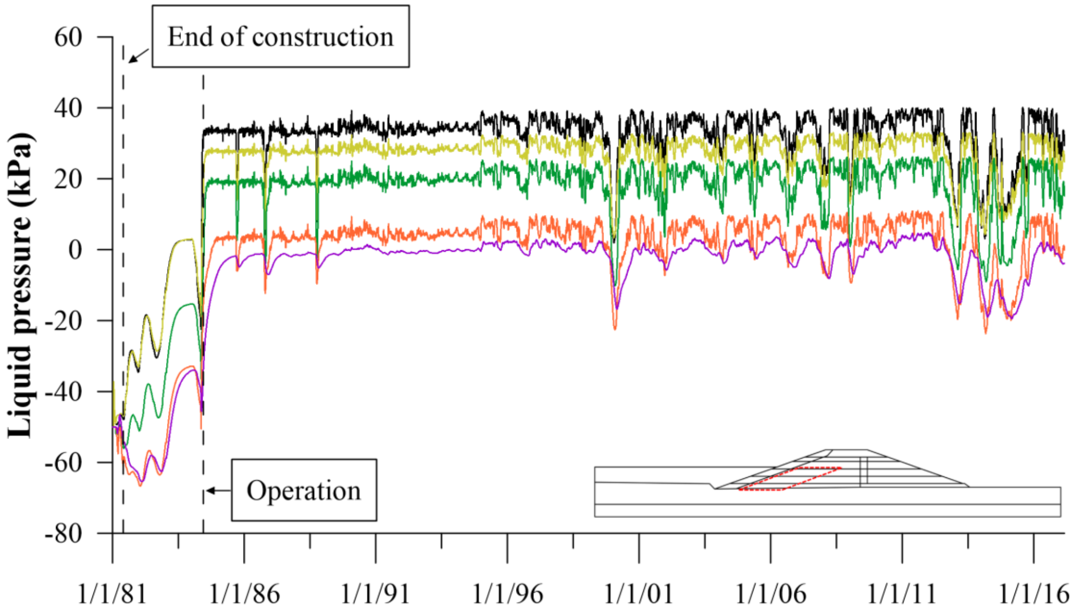

Figure 66. Evolution of pore water pressure at random select points within the embankment

Figure 67 presents the evolution of the historical variable p_0^* over different periods of the analysis. Since the LC and SI curves are coupled, suction-induced causes both curves to shift simultaneously. Time zero corresponds to the initial condition, 149 days to the end of construction (stage F), 1260 days to the end of reservoir impoundment (stage H), and 13207 days to the end of the simulated operational period. The results show an evolution of p_0^* only during construction and reservoir impoundment, while no yielding occurred during the operation stage, i.e., during operation the response remained entirely within the elastic domain, with no shift in either the LC or SI curve.

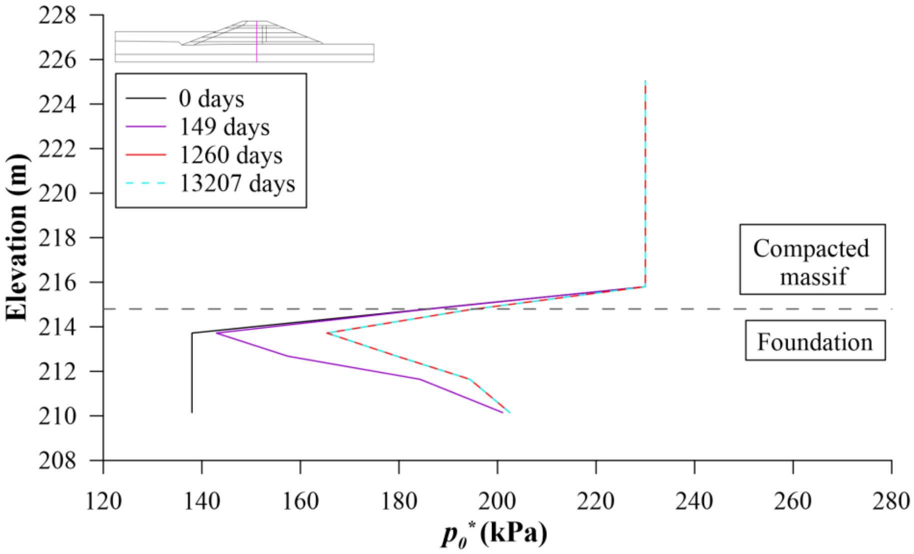

Figure 67. Evolution of the historical variable p0* during the construction, impoundment and operation of the earth dam considering the BBM extended with the SI curve

In summary, the implementation of the SI curve into the BBM mechanical model represents an important advance in the computational modeling and analysis of soil behavior under drying-induced plasticity. The results of the volumetric shrinkage tests performed with Itaipu soil validated the implemented model in CODE_BRIGHT and allowed the calibration of suction-hardening parameters. However, despite the good results obtained in the application of the BBM extended with the SI curve to literature benchmarks and laboratory tests, the model was not sufficient to explain the settlements observed in the dam, as recorded by the reference marker (MR-L-23) and settlement gauge (MA-L-08).

The main hypothesis of this research was that the settlements observed during operation were caused by prolonged periods with the reservoir water level below the normal operating range, inducing plastic settlements through soil drying processes. The numerical simulations, as designed in this study, indicated that reservoir level fluctuations alone did not produce suction variations large enough to activate the SI curve and trigger plastic strains in the red clay foundation or the compacted soil layers. Nevertheless, these results do not invalidate the hypothesis; instead, they suggest the need for further investigation of the parameters governing soil response to drying.

Therefore, while the SI curve implementation did not fully capture the observed settlements at Itaipu dam simulation, it constitutes an important contribution by extending the BBM framework to account for drying-induced hardening. This development establishes a base for future investigations, enabling a more accurate exploration of suction-related plasticity and a better understanding of how soil parameters and reservoir operation conditions influence dam settlements.

9 CONCLUSIONS

The numerical simulation covered the entire history of the left bank earth dam of Itaipu, specifically for station 135+50, from its construction and reservoir impoundment to approximately 30 years of operation. The simulation results of the construction and reservoir filling stages were consistent with field instrumentation data, including readings from piezometers and settlement gauges. At the end of the construction phase, the simulated stress field closely matched the design estimates for the dam.

Validation of the adopted mechanical and hydraulic parameters, as well as boundary and initial conditions, was achieved through numerical simulation of the construction and impoundment stages. This phase also provided a deeper evaluation of the coupled hydro-mechanical behavior of the soil. Simulated results indicated plastic strain of the foundation soil due to loading and collapse paths, with the latter caused by a rise in the water table after construction.

The collapse phenomenon is typically associated with significant soil deformations due to moisture, resulting in considerable geotechnical issues. In the case of the Itaipu earth dam, the wetting-induced plastic strain observed in the foundation layer was of minor magnitude, with strain of 0.5% out of a total of approximately 3.5%. Although this value is low, identifying this phenomenon allowed for a better understanding of the dam's hydro-mechanical behavior in its early years after construction.

The numerical simulation of the dam's operation aimed to understand the plastic settlements recorded by survey marker MR-L-23 installed on the crest. These settlements were approximately 2.5 centimeters between 1999 and 2000, followed by stabilization, and a subsequent settlement of around 3.0 centimeters between 2012 and 2015. These settlements occurred after prolonged periods of operation with reservoir water levels below usual operating levels. The numerical simulation was initially performed using the BBM formulation originally implemented in CODE_BRIGHT, which does not incorporate plastic strains induced by soil drying. Consequently, the model was not able to reproduce the field settlements.

To address this limitation, the SI curve was incorporated into the thermo-elasto-plastic model (TEP) through the extension proposed by Pedroso and Farias (2011), which provides a unified smooth yield surface in the stress–suction space. This development enabled the calibration of suction-hardening parameters based on volumetric shrinkage tests with Itaipu soil and demonstrated good performance when applied to benchmarks and laboratory experiments. However, the extended BBM with the SI curve was not sufficient to reproduce the settlements recorded in the dam during prolonged periods of low reservoir levels. Numerical simulations indicated that reservoir fluctuations alone did not induce suction changes large enough to activate drying-induced plasticity in the foundation and compacted layers. These findings suggest that additional mechanisms or refined parameter characterization may be required to explain the observed behavior. Even though the model did not fully capture the field response, the incorporation of the SI curve represents a significant advance in extending the BBM to account for drying-induced hardening, providing a solid basis for future investigations on suction-related plasticity and its implications for dam performance.

10 PERSPECTIVES FOR FUTURE RESEARCHS

Based on the conclusions and advances achieved in this work, the following perspectives for future research can be outlined:

- Numerically simulate the operation of the earth dam, considering the section of interest with constitutive models that account for the expansive behavior of the soil, such as the Barcelona Expansive Model (BExM) (ALONSO; VAUNAT; GENS, 1999) and the Double Structure Model (SÁNCHEZ et al., 2005). These models describe a continuous compression path and are capable of capturing plasticity induced by wetting–drying cycles, even for soils with limited expansive characteristic;
- Perform parametric sensitivity analyses to investigate the influence of the soil's drying-related mechanical parameters on plastic yielding induced by suction increase;
- Conduct laboratory tests to better characterize the soil drying parameters, particularly the hardening parameter s_o, which defines the initial position of the SI yield curve. Carry out laboratory experiments that include suction variation cycles, to understand the soil behavior under reservoir water level fluctuations. These tests are particularly relevant for improving the understanding of the soil drying mechanisms and for enhancing numerical analyses, either by using the methodology described in this work, which considers the SI curve, or by employing other models capable of reproducing soil hardening induced by wetting and drying cycles.

BIBLIOGRAPHIC REFERENCES

2061.50.1757.P. **Barragem de Terra e de Transição - M.E. Maciço de Argila Plástica: Relatório Final**. Foz do Iguaçu: [s.n.].

2063.50.0253.P. **Ensaios Geotécnicos sobre amostras indeformadas da fundação da barraggem de terra - Margem esquerda e dos aterros experimentais e sobre amostras deformadas das áreas de empréstimo "Dois Irmãos" e da "Escavação da fundação da barragem de enrocamento" - Usi**. Foz do Iguaçu: [s.n.].

2080.54.15717-P. **Fundação da Barragem de Terra - M.E.** Foz do Iguaçu: [s.n.].

4280.50.8003-E. **Aprovechamiento Hidroelectrico de Itaipu - Presa de Tierra Margen Izquierda y Transicion con la Presa de Enrocado: Informe Final del Proyecto**. Foz do Iguaçu: [s.n.].

4280.50.8007-E. **Aprovechamiento Hidroelétrico de Itaipu - Informe Geotecnico Final - Sintesis de los parametros geotecnicos y analisis de estabilidad del macizo**. Foz do Iguaçu: [s.n.].

AITCHISON, G. D. **Engineering concepts of moisture changes in soils - Statement of the review panel**. (Butterwoths, Ed.)Moisture equilibria and moisture changes in the soils beneath covered areas. **Anais**...Sydney: 1965.

ALONSO, E. E. Field applications of unsaturated soil mechanics. In: **Advances in Unsaturated Soil, Seepage, and Environmental Geotechnics**. [s.l: s.n.]. p. 1–33.

ALONSO, E. E. et al. Modelling the response of lechago earth and rockfill dam. **Geotechnique**, v. 61, n. 5, p. 387–407, 2011.

ALONSO, E. E.; BATLLE, F. Construction and Impoudment of an Earthdam. Application of the coupled flow-deformation analysis of unsaturated soils. In: **Modern Issues in Non-Saturated Soils**. [s.l.] Springer, 1995.

ALONSO, E. E.; GENS, A.; HIGHT, D. **Special Problem Soils. General Report**. (E. T. Hanrahan, T. L. L. Lorr, T. F. Widdis, Eds.)9th European Conference of Soil Mechanics and Foundation Engineering. **Anais**...Dublin: 1987.

ALONSO, E. E.; GENS, A.; JOSA, A. A constitutive model for partially saturated soils. **Géotechnique**, v. 41, n. 2, p. 273–275, jun. 1991.

ALONSO, E. E.; OLIVELLA, S. Unsaturated Soil Mechanics Applied to Geotechnical Problems. In: **Unsaturated soils 2006**. [s.l: s.n.]. p. 1–35.

ALONSO, E. E.; OLIVELLA, S.; HUGAS, J. Modelling the behavior of an earth and rockfill dam during construction and impoundment. In: **Unsaturated soils: Numerical and Theorical Approaches: Proceedings of the International Conference "From Experimental Evidence towards Numerical Modeling of Unsaturated Soils"**. Weimar, Germany: Springer Berlin Heidelberg, 2005. p. 269–287.

ALONSO, E. E.; OLIVELLA, S.; PINYOL, N. M. A review of Beliche Dam. **Geotechnique**, v. 55, n. 4, p. 267–285, 2005.

ALONSO, E. E.; PINYOL, N. M. **Unsaturated soil mechanics in earth and rockfill dam engineering**. (D. G. Toll et al., Eds.)Unsaturated soils: advances in geo-engineering. **Anais**...London: 2008.

ALONSO, E. E.; PINYOL, N. M. Numerical analysis of rapid drawdown: Applications in real cases. **Water Science and Engineering**, v. 9, n. 3, p. 175–182, 2016.

ALONSO, E. E.; VAUNAT, J.; GENS, A. Modelling the mechanical behaviour of expansive clays. **Engineering Geology**, v. 54, n. 1–2, p. 173–183, 1999.

ALONSO, M. et al. Three-Dimensional Modelling of a Large-Diameter Sealing Concept in a Deep Geological Radioactive Waste Disposal. **Rock Mechanics and Rock Engineering**, p. 1–26, 2024.

AMARAL, E. D.; LOYOLA, A. C.; CORDÃO NETO, M. P. Probabilistic Analysis of Dams Built with Collapsible Material. **International Journal of Geomechanics**, v. 20, n. 10, p. 1–12, 2020.

BISHOP, A. W. The principle of effective stress. **Tecknish Ukeblad**, v. 106, p. 859–863, 1959.

BROOKS, R. H.; COREY, A. T. Hydraulic Properties of Porous Media. **Hydrology Papers. Colorado Sate University**, v. 3, 1964.

CASINI, F.; VAUNAT, J.; ROMERO, E. Consequences on water retention properties of double-porosity features in a compacted silt. **Acta Geotechnica**, v. 7, p. 139–150, 2012.

CHANG, C. S.; DUNCAN, J. M. **Analysis of Consolidation of Earth and Rockfill Dams**. Berkeley, California: [s.n.].

CHEN, Q. et al. Modelling the construction of a high embankment dam. **KSCE Journal of**

Civil Engineering, v. 18, n. 1, p. 93–102, 2015.

CHEN, W. F.; ZHANG, H. **Structural Plasticity: Theory, Problems, and CAE software**. 2. ed. New York: Springer Verlag, 1991.

COSTA, L. M.; ALONSO, E. E. Predicting the Behavior of an Earth and Rockfill Dam under Construction. **Journal of Geotechnical and Geoenvironmental Engineering**, v. 135, n. 7, p. 851–862, 2009.

CRONEY, D. The movement and distribution of water in soils. **Geotechnique**, v. 3, n. 1, p. 1–16, 1952.

DE FARIAS, M. M.; CORDÃO NETO, M. P. Advanced numerical simulation of collapsible earth dams. **Canadian Geotechnical Journal**, v. 47, n. 12, p. 1351–1364, 2010.

DE FARIAS, M. M.; NETO, M. P. C. Advanced numerical simulation of collapsible earth dams. **Canadian Geotechnical Journal**, v. 47, n. 12, p. 1351–1364, 2010.

DONG, Y. Performance of explicit substepping integration scheme for complex constitutive models in finite element analysis. **Computers and Geotechnics**, v. 162, n. March, 2023.

FREDLUND, D. G.; MORGENSTERN, N. R. Stress state variables for unsaturated soils. **Journal of the Geotechnical Engineering Division**, v. 103, n. 5, p. 447–466, 1977.

FREDLUND, D. G.; RAHARDJO, H. **Soil mechanics for unsaturated soils**. 1. ed. [s.l.] John Wiley & Sons, 1993.

GALLIPOLI, D. et al. An elasto-plastic model for unsaturated soil incorporating the effects of suction and degree of saturation on mechanical behaviour. **Géotechnique**, v. 53, n. 1, p. 123–136, 2003.

GALLIPOLI, D.; D’ONZA, F.; WHEELER, S. J. A sequential method for selecting parameter values in the barcelona basic model. **Canadian Geotechnical Journal**, v. 47, n. 11, p. 1175–1186, 2010.

GALLIPOLI, D.; WHEELER, S. J.; KARSTUNEN, M. Modelling the variation of degree of saturation in a deformable unsaturated soil. **Géotechnique**, v. 53, n. 1, p. 105–112, 2003.

GENS, A.; SÁNCHEZ, M.; SHENG, D. On constitutive modelling of unsaturated soils. **Acta Geotechnica**, v. 1, n. 3, p. 137–147, 2006.

IECO-ECL. **Aproveitamento Hidrelétrico de Itaipu: Relatório do Histórico do Desempenho das Estruturas e suas fundações. Relatório n° 4006.50.00024**. [s.l: s.n.].

ITAIPU BINACIONAL. **Itaipu vai defender, em Paris, integração à Rede Mundial de**

Reservas de Biosfera (in Portuguese). Disponível em: <https://www.itaipu.gov.br/sala-de-imprensa/noticia/itaipu-vai-defender-em-paris-integracao-rede-mundial-de-reservas-de-biosfer>. Acesso em: 20 mar. 2025.

ITAIPU BINACIONAL. **Itaipu - Generation**. Disponível em: <https://www.itaipu.gov.br/energia/geracao>. Acesso em: 30 out. 2025.

KOLEV, B. N. **Stress-deformation analysis of Denis-Perron dam: verification and validation for better prediction of rockfill response**. [s.l.] University of British Columbia, 2017.

LI, H. et al. Recent developments of generalized plasticity models for saturated and unsaturated soils. **Water Science and Engineering**, v. 4, n. 3, p. 329–344, 2011.

LI, X.; ZIENKIEWICZ, O. C. Multiphase Flow in Deforming Porous Media and Finite Element Solutions. **Computers and Structures**, v. 45, n. 2, p. 211–227, 1992.

MAŠÍN, D. Predicting the dependency of a degree of saturation on void ratio and suction using effective stress principle for unsaturated soils. **International Journal for Numerical and Analytical Methods in Geomechanics**, v. 34, p. 73–90, 2010.

MATYAS, E. L.; RADHAKRISHNA, H. S. Volume Change Characteristics of partially saturated soils. **Géotechnique**, v. 18, n. 4, p. 432–448, 1968.

MELLO, J. B. **Experimental Study of geotechnical parameter of Itaipu left earth dam (In Portuguese)**. [s.l.] São Paulo State University, 2022.

NAYLOR, D. J. et al. **Finite Elements in Geotechnical Engineering**. Swansea, U.K.: Pineridge Press, 1981.

NAYLOR, D. J. et al. Predtion of construction performance of Beliche Dam. **Geotechnique**, v. 36, n. 3, p. 359–376, 1986.

NAYLOR, D. J.; MARANHA DAS NEVES, E.; VEIGA PINTO, A. A. A back-analysis of beliche dam. **Geotechnique**, v. 47, n. 2, p. 221–233, 1997.

OLIVELLA, S. et al. Numerical formulation for a simulator (CODE_BRIGHT) for the coupled analysis of saline media. **Engineering Computations**, v. 13, n. 7, p. 87–112, nov. 1996.

PEDROSO, D. M.; FARIAS, M. M. Extended Barcelona Basic Model for unsaturated soils under cyclic loadings. **Computers and Geotechnics**, v. 38, n. 5, p. 731–740, 2011.

PERTL, M.; HOFMANN, M.; HOFSTETTER, G. Coupled solid-fluid FE-analysis of an embankment dam. **Frontiers of Architecture and Civil Engineering in China**, v. 5, n. 1, p. 53–62, 2011.

PHOON, K.-K.; KULHAWY, F. H. Characterization of geotechnical variability.

Canadian Geotechnical Journal, v. 36, n. 1, p. 612–624, 1999.

PINYOL, N. M.; ALONSO, E. E. Design, Construction, Monitoring and Modelling of Albagés Earth Dam: A Case History. **International Journal of Civil Engineering**, v. 17, n. 4, p. 501–513, 2019.

PINYOL, N. M.; ALONSO, E. E.; OLIVELLA, S. Rapid drawdown in slopes and embankments. **Water Resources Research**, v. 44, n. 5, p. 1–22, 2008.

REPORT 4280.50.8006. **Presa de Tierra Margen Izquierda - Memoria Tecnica de la Construccion - Volume II**. [s.l: s.n.].

RODRIGUES, R. A.; SOARES, F. V.; SANCHEZ, M. Settlement of Footings on Compacted and Natural Collapsible Soils upon Loading and Soaking. **Journal of Geotechnical and Geoenvironmental Engineering**, v. 147, n. 4, 2021.

RODRIGUES, R. DE L. **Comportamento da Barragem de Terra da Margem Esquerda de Itaipu Durante Período de Operação**. [s.l.] Pontifícia Universade Católica do Rio de Janeiro, 2017.

ROSCOE, K. H.; BURLAND, J. B. On the generalized stress-strain behavior of "wet" clay. In: HEYMAR, J.; LECKIE, F. A. (Eds.). **Engineering plasticity**. [s.l.] Cambridge University Press, 1968. p. 535–609.

ROSCOE, K. H.; SCHOFIELD, A. N. **Mechanical behaviour of an idealised "wet" clay**. 2nd Eur. Conf. Soil Mechs. and Foundation Engineering. **Anais**...Wiesbaden: 1963.

SANCHEZ, M. **Transport phenomena in porous media (Lecture Notes)**. College StationTexas A&M University, , 2018.

SÁNCHEZ, M. et al. A double structure generalized plasticity model for expansive materials. **International Journal for Numerical and Analytical Methods in Geomechanics**, v. 29, n. 8, p. 751–787, 2005.

SHENG, D. et al. Finite element formulation and algorithms for unsaturated soils. Part I: Theory. **International Journal for Numerical and Analytical Methods in Geomechanics**, v. 27, n. 9, p. 745–765, 2003.

SHENG, D. et al. Unsaturated soils: From constitutive modelling to numerical algorithms. **Computers and Geotechnics**, v. 35, n. 6, p. 810–824, 2008.

SHENG, D.; FREDLUND, D. G. **Elasto-plastic modelling of unsaturated soils : An overview**. 12th International Conference on Computer Methods and Advances in Geomechanics 2008. **Anais**...2008.

SHOWKAT, R.; BABU, G. L. Deterministic and probabilistic analysis of the response of shallow footings on unsaturated soils due to rainfall. **Transportation Geotechnics**, v. 43,

p. 1–15, 2023.

SHOWKAT, R.; MOHAMMADI, H.; BABU, G. L. S. Effect of Rainfall Infiltration on the Stability of Compacted Embankments. **International Journal of Geomechanics**, v. 22, n. 7, 2022.

SICA, S.; PAGANO, L.; ROTILI, F. Rapid Drawdown on Earth Dam Stability After a Strong Earthquake. **Computer and Geotechnics**, v. 116, p. 103187, 2019.

SLOAN, S. W. Substepping schemes for the numerical integration of elastoplastic stress–strain relations. **International Journal for Numerical Methods in Engineering**, v. 24, n. 5, p. 893–911, 1987.

SLOAN, S. W.; ABBO, A. J.; SHENG, D. Refined explicit integration of elastoplastic models with automatic error control. **Engineering Computations**, v. 18, n. 1–2, p. 121–154, 2001.

TURKSON, P.; VANDENBERGE, D. R. Rapid Drawdown Analysis Using Pore Pressures from BBM. **Geotechnical and Geological Engineering**, n. 0123456789, 2023.

VAN GENUCHTEN, M. T. A Closed-Form Equation for Predicting the Hydraulic Conductivity of Unsaturated Soils. **Soil Science Society of America Journal**, v. 44, n. 5, p. 892–898, 1980.

WHEELER, S. J.; GALLIPOLI, D.; KARSTUNEN, M. Comments on use of the Barcelona Basic Model for unsaturated soils. **International Journal for Numerical and Analytical Methods in Geomechanics**, v. 26, n. 15, p. 1561–1571, 2002.

ZHANG, F.; IKARIYA, T. A new model for unsaturated soil using skeleton stress and degree of saturation as state variables. **Soils and Foundations**, v. 51, n. 1, p. 67–81, 2011.

ZHANG, X.; XIAO, M. Using modified state surface approach to select parameter values in the Barcelona Basic Model. **International Journal for Numerical and Analytical Methods in Geomechanics**, v. 37, p. 1847–1866, 2013.